

Universität der Bundeswehr München
Fakultät für Luft- und Raumfahrttechnik
Institut für Strömungsmechanik und Aerodynamik

On the performance increase of future space launchers: Investigations of buffeting, its reduction via passive flow control, and the Dual-Bell nozzle concept at trans- and supersonic flight conditions

Istvan Bolgar M.Sc.

Vollständiger Abdruck der von der
Fakultät für Luft- und Raumfahrttechnik
der Universität der Bundeswehr München
zur Erlangung des akademischen Grades eines

Doktor-Ingenieurs (Dr.-Ing.)

genehmigten Dissertation.

Gutachter:

1. Prof. Dr. rer. nat. habil. Christian J. Kähler
2. Prof. Dr.-Ing. Rolf Radespiel

Diese Dissertation wurde am 19.06.2019 bei der Universität der Bundeswehr München eingereicht und durch die Fakultät für Luft- und Raumfahrttechnik am 05.11.2019 angenommen. Die mündliche Prüfung fand am 13.11.2019 statt.

ACKNOWLEDGMENTS

I would like to take this opportunity to thank the people who made my dissertation possible. First, I would like to thank Prof. Christian Kähler, who gave me the opportunity to work at his institute with state-of-the-art facilities and measurement equipment, and a constructive working environment. I am especially thankful to him for guiding the research focus of my DFG project into novel nozzle concepts within the last funding period. This had already been one of my favorite topics throughout my studies.

Secondly, I want to thank Prof. Rolf Radespiel, who took the time to evaluate my work as part of the examination committee. Besides this, he increased the quality of my scientific work in his role within my DFG project. I will always remember his critical and peculiar questions during our meetings, in order to improve the output of the overall project.

Next I would like to thank all of my colleagues for all of the great discussions and for any help with my experiments. I am especially thankful for Dr. Sven Scharnowski's supervision during the entire time of my work. Through his widespread knowledge, he taught me all the necessary skills to carry out PIV measurements to the highest standards, and motivated me to excel at my engineering skills. His particular interest in my project led to a productive collaboration and to successful advances within my research. It was a pleasure to have him as a mentor.

I will also thank my parents at this point, as they have always supported me with my many ideas and extra-curricular activities. Without their guidance and experience, I would not have been able to coordinate all of these projects at once. Last but not least, I would like to thank my wonderful girlfriend Judith, who has also tolerated my eccentric ventures and continues to do so. She always believes in my capabilities and encourages me to realize my full potential. She was the biggest moral support during difficult times, and she was the best reason to go home to at the end of the day.

ACKNOWLEDGMENTS

TABLE OF CONTENTS

	Page
LIST OF FIGURES	ix
SYMBOLS	xv
ABSTRACT / KURZFASSUNG	1
1 Introduction	3
2 Ariane 5: Mission, early problems, and research questions	5
2.1 A typical mission profile of Ariane 5	5
2.2 Early problems with Ariane 5	10
2.2.1 Ariane 501 flight VA88	10
2.2.2 Ariane 517 flight VA157	11
2.2.3 Ariane 5 buffeting	12
2.3 Research questions	13
3 On the prediction of buffeting	15
3.1 Numerical limitations	15
3.2 Experimental challenges	18
3.2.1 Dimensional challenges	18
3.2.2 Measurement techniques	19
3.3 The solution: Particle image velocimetry, high-frequency pressure sensors & high-speed schlieren	21
4 Simplification of a complex problem: A backward-facing step in the Trisonic Wind Tunnel Munich	25
4.1 A backward-facing step as a simplified launcher geometry	25
4.2 The measurement facility & its boundary conditions	28
4.2.1 The Trisonic Wind Tunnel Munich	28
4.2.2 PIV setup used at the TWM	29
4.2.3 Schlieren setup at the TWM	30
4.2.4 Free-stream turbulence level in the test section	30
4.2.5 Mach number distribution in the test section	31
4.2.6 Shock-free model in transonic flow and supersonic shock reflection	33
4.2.7 Incoming boundary layer	36
4.2.8 Tracer particle response across shocks	37
5 The separated shear layer at relevant flight conditions	39
5.1 Literature review of separated shear layers	39
5.2 Experimental setup	47
5.2.1 Test cases & BFS model	47
5.2.2 Particle image velocimetry	48
5.2.3 Dynamic pressure measurements	49

TABLE OF CONTENTS

5.2.4	Simultaneous PIV-pressure measurements	49
5.3	BFS results & discussion	51
5.3.1	Mean flow field & reattachment	51
5.3.2	Dynamic flow field statistics	55
5.3.3	Dynamic pressure measurements	59
5.3.4	Pressure-velocity correlations	67
5.4	Summary & conclusions on the separated shear layer aft of a BFS	70
6	Load reduction with passive flow control	73
6.1	Literature review of flow control on a BFS	73
6.2	Experimental setup	77
6.2.1	Test cases & BFS model	77
6.2.2	Flow control devices	78
6.2.3	Particle image velocimetry	78
6.2.4	Dynamic pressure measurements	79
6.3	Flow control results & discussion	79
6.3.1	Mean flow field & reattachment	79
6.3.2	Dynamic flow field statistics	85
6.3.3	Mean pressures and RMS fluctuations on the reattachment surface	88
6.3.4	Pressure spectra	94
6.4	Summary & conclusions on passive flow control aft of a BFS	101
7	Design and validation of a nozzle model	103
7.1	Literature review of supersonic nozzle flow	103
7.2	Design of the nozzle model	108
7.2.1	Thrust chamber design	108
7.2.2	Nozzle design	113
7.2.3	Structural analysis	115
7.3	Experimental setup	117
7.3.1	The thrust optimized nozzle model	117
7.3.2	Test cases	119
7.3.3	Particle image velocimetry	119
7.3.4	Schlieren measurements	119
7.4	Integration and validation of the nozzle model in the TWM	119
7.4.1	Nozzle flow and seeding	119
7.4.2	Interaction between a nozzle flow and transonic external flow	121
7.4.3	Interaction between a nozzle flow and a supersonic external flow	125
7.5	Summary & conclusions on the TOC nozzle model	129
8	The feasibility of a Dual-Bell nozzle at relevant flight conditions	131
8.1	Literature review on Dual-Bell nozzles	131
8.2	Experimental setup	137
8.2.1	The Dual-Bell nozzle model	137
8.2.2	Test cases	139

8.2.3	Particle image velocimetry	139
8.2.4	Schlieren measurements	139
8.3	Results of the Dual-Bell nozzle	139
8.3.1	Nozzle mode prediction with CFD	139
8.3.2	Experiments in sea level mode	144
8.3.3	Experiments in altitude mode	149
8.3.4	Experiments on transition	151
8.4	Summary & conclusions on the feasibility of Dual-Bell nozzles	154
9	Summary & future outlook of space launchers	157
	LIST OF REFERENCES	161

TABLE OF CONTENTS

LIST OF FIGURES

Figure	Page
2.1 Left: Graphical illustration of Ariane 5. Right: Ariane 5 shortly after takeoff. A shear layer separates at the geometric discontinuity and reattaches on the Vulcain 2 nozzle. Images from ESA	6
2.2 Ariane 5 typical sequence of events. Image is originally published in Ariane 5's user manual (Arianespace 2016a).	7
2.3 Top: Ariane 5 time vs. altitude. Bottom: Ariane 5 time vs. relative velocity. Both plots have been generated in accordance with Ariane 5's user manual (Arianespace 2016a).	9
3.1 Basic PIV system setup	23
4.1 Dimensional drawing of the planar space launcher model. Dimensions are provided in units of [mm].	27
4.2 Trisonic Wind Tunnel Munich: (1) compressors, (2) tanks, (3) gate valve, (4) control valve, (5) variable Laval nozzle, (6) test section, (7) variable diffuser/nozzle, (8) exhaust tower.	29
4.3 Total pressure vs. free-stream turbulence level as a function of the Mach number in the TWM. This figure is published in Scharnowski et al. (2019b).	31
4.4 Mach number distribution within the test section referenced to a static pressure probe at $x/h \approx -30$	32
4.5 Instantaneous schlieren recordings showing the density gradients in the horizontal direction at $Ma_\infty = 0.80, 0.90, \& 2.00$ from top to bottom. Green to red corresponds to increasing density in the streamwise direction while red to green corresponds to decreasing density.	35
5.1 Separated flow phenomena occurring on a BFS	44
5.2 Three-dimensional behavior of the flapping mode (left) and the pumping mode (right). These results from a large-eddy simulation (LES) are published in Statnikov, Bolgar, Scharnowski, Meinke, Kähler, & Schröder (2016a).	45
5.3 Theoretical formation process of the finger-like structures aft of a BFS found by Scharnowski, Bolgar, & Kähler (2017). Note that the figure only serves as an illustration and is not drawn to scale.	46
5.4 Illustration of the planar space launcher model with its pressure ports and the field of view under investigation	48

LIST OF FIGURES

5.5	Comparison of the mean total pressure coefficients measured with static pressure probes vs. dynamic pressure transducers at $Ma_\infty = 0.80$. The error bars indicate the standard deviations of the pressure values.	50
5.6	Streamwise component of the mean flow fields at various Mach numbers . . .	53
5.7	Mean pressure coefficients at various Mach numbers. The pressure p_∞^* and the velocity U_∞^* indicate the far-field quantities at $x/h \approx -2.5$ and $x/h \approx -58.5$ for the sub- and supersonic cases, respectively.	54
5.8	Free-stream Mach number vs. reattachment length for planar and axisymmetric BFS: $Ma_\infty = 0.7$ from Scharnowski & Kähler (2015), $Ma_\infty = 0.8$ from Depres et al. (2004), $Ma_\infty = 2$ from Roshko & Thomke (1966).	54
5.9	Back-flow ratio for various Mach numbers at $y/h = 0.1$	56
5.10	Reynolds shear stress distribution at various Mach numbers. Contour lines indicate $\overline{u'v'}/U_\infty^2 = -0.003, -0.01, -0.02, -0.03$ towards the center.	57
5.11	Reynolds stress profiles at x_r for various Mach numbers	58
5.12	Mean (top) and RMS (bottom) total pressure coefficients at various Mach numbers. The pressure p_∞^* indicates the far-field pressure at $x/h \approx -2.5$ and $x/h \approx 58.5$ for the sub- and supersonic cases, respectively.	60
5.13	Normalized pressure fluctuations at $Ma_\infty = 0.80$ (left) and $Ma_\infty = 2.00$ (right) in space and time	61
5.14	Illustration of the modes of the surface pressure fluctuations within a spectrogram (on the left) and its according 2D spectrum extracted at $x/h = 6$ (on the right) at $Ma_\infty = 0.60$	62
5.15	Streamwise evolution of the power spectral density of the surface pressure fluctuations at various free-stream Mach numbers	65
5.16	Left: Streamwise evolution of the PSD of the surface pressure fluctuations at $Ma_\infty = 2.00$ for the baseline case. Right: PSD extracted at $x/h = 4$ from the spectrogram in the left illustration.	66
5.17	Correlation of pressure fluctuations at $x/h = 7$ to the scalars of the velocity field fluctuations at $Ma_\infty = 0.80$. Left column shows R_{pu} , right column shows R_{pv} . Images from top to bottom are offset by two time steps of the pressure transducers or $\Delta t = 117 \mu s$. The contour lines indicate a correlation of $R = \pm 0.15$	68
5.18	Correlation of pressure fluctuations at $x/h = 4$ to the scalars of the velocity field fluctuations at $Ma_\infty = 2.00$. Left column shows R_{pu} , right column shows R_{pv} . Images from top to bottom are offset by two time steps of the pressure transducers or $\Delta t = 117 \mu s$. The contour lines indicate a correlation of $R = \pm 0.15$	69
6.1	Illustration of the planar space launcher model with its pressure ports and the field of view under investigation	77
6.2	Modified BFS: Flow control devices under investigation	79
6.3	Streamwise component of the mean flow fields at $Ma_\infty = 0.80$ of the baseline vs. the FCL and FSL geometries at the lobes' valleys and peaks	82

6.4	Streamwise component of the mean flow fields at $Ma_\infty = 0.80$ for decreasing lobe sizes of the full circular and full square lobes measured at the lobes' peaks	83
6.5	Streamwise component of the mean flow fields at $Ma_\infty = 2.00$ showing a local shock ahead of the step with flow control	84
6.6	Reynolds shear stress distribution at $Ma_\infty = 0.80$ for the baseline vs. the FCL and FSL geometries at the lobes' valleys and peaks. Contour lines indicate $\overline{u'v'}/U_\infty^2 = -0.003, -0.01, -0.02, -0.03, -0.04$ towards the center	86
6.7	Comparison of the Reynolds shear stress distribution at $Ma_\infty = 0.80$ for decreasing lobe sizes of the full circular and full square lobes measured at the lobes' peaks. Contour lines indicate $\overline{u'v'}/U_\infty^2 = -0.003, -0.01, -0.02, -0.03, -0.04$ towards the center	87
6.8	Comparison of the mean and RMS total pressures coefficients along the reattachment surface at $Ma_\infty = 0.80$ for all large lobe geometries measured behind the lobe valleys and peaks. The pressure p_∞^* indicates the far-field pressure at $x/h \approx -2.5$	89
6.9	Comparison of the mean and RMS total pressures coefficients along the reattachment surface at $Ma_\infty = 0.80$ for the circular and square lobe geometries with decreasing size measured behind the lobe peaks. The pressure p_∞^* indicates the far-field pressure at $x/h \approx -2.5$	91
6.10	Comparison of the mean and RMS total pressures coefficients along the reattachment surface at $Ma_\infty = 2.00$ for all large lobe geometries measured behind the lobe valleys and peaks. The pressure p_∞^* indicates the far-field pressure at $x/h \approx -58.5$	93
6.11	Left: Streamwise evolution of the PSD of the surface pressure fluctuations at $Ma_\infty = 0.80$ for the baseline case. Right: PSD extracted at $x/h = 7$ from the spectrogram in the left illustration	94
6.12	Comparison of the streamwise evolution of the PSD of the surface pressure fluctuations at $Ma_\infty = 0.80$ for all the large lobe geometries measured behind the lobe valleys and peaks	96
6.13	Comparison of the streamwise evolution of the PSD of the surface pressure fluctuations at $Ma_\infty = 0.80$ for the circular and square lobe geometries with decreasing size measured behind the lobe peaks	98
6.14	Comparison of the streamwise evolution of the PSD of the surface pressure fluctuations at $Ma_\infty = 2.00$ for all the lobe geometries measured behind the lobe valleys and peaks	100
7.1	Illustration of a convergent-divergent nozzle with a thrust optimized contour	104
7.2	Various plume shapes dependent on $sNPR$	106

7.3	2D CFD analysis of a flow channel for implementing a honeycomb flow straightener. The static pressure distribution is displayed on the upper symmetrical half of the flow channel. The streamwise component of the mean velocity is illustrated on the lower half of the flow channel.	110
7.4	3D CFD analysis of flow channels with decreasing cross-sections in the 90° turn. Top: Flow channel with guide vanes. Bottom: Flow channel without guide vanes. Note that only the lower symmetry half of the flow channel is shown. The streamwise components of the mean velocity are shown in the left-hand channels. The pressure distributions are shown in the right-hand channels.	112
7.5	2D CFD analysis of the final TOC nozzle at desired operating conditions. The upper symmetry half indicates the mean static pressure distribution. The lower symmetry half indicates the mean streamwise velocity distribution.	114
7.6	FEM analysis of the nozzle model at 9 bar pressure differential. Top: illustration of model internals. Middle: von Mises stress distribution. Bottom: model displacement.	116
7.7	Illustration of the planar space launcher model with a 2D TOC nozzle and the measurement locations for PIV and schlieren	118
7.8	Left: Raw PIV image with seeding in the external and nozzle flow at $Ma_\infty = 0.80$. Right: Streamwise component of the vector field calculated from the raw PIV image.	120
7.9	Illustration of the streamwise component of the mean flow field at $Ma_\infty = 0.80$ without a jet plume at the top, and with a jet plume at the bottom	121
7.10	Schlieren shadowgraph at $Ma_\infty = 0.80$ with the jet plume in operation. The overexpansion of the nozzle is clearly visible through the presence of the characteristic overexpansion shocks stemming off the nozzle's lip.	122
7.11	Distribution of the Reynolds shear stresses at $Ma_\infty = 0.80$ without a jet plume at the top, and with a jet plume at the bottom. Contour lines indicate $\overline{u'v'}/U_\infty^2 = \pm 0.003, \pm 0.01, \pm 0.02$ towards the center.	123
7.12	Two-point correlation of v' at $Ma_\infty = 0.80$ with a jet plume. The + sign indicates the location that is correlated to the rest of the FOV. Contour lines indicate $R = \pm 0.2$	124
7.13	Illustration of the streamwise component of the mean flow field at $Ma_\infty = 2.00$ without a jet plume at the top, and with a jet plume at the bottom	125
7.14	Schlieren shadowgraph at $Ma_\infty = 2.00$ with the jet plume in operation. The underexpansion of the nozzle is clearly visible through the presence of the expansion waves surrounding the triangular jet plume core.	126
7.15	Distribution of the Reynolds shear stresses at $Ma_\infty = 2.00$ without a jet plume at the top, and with a jet plume at the bottom. Contour lines indicate $\overline{u'v'}/U_\infty^2 = \pm 0.003$	127

7.16	Two-point correlation of v' at $Ma_\infty = 0.80$ with a jet plume. The + sign indicates the location that is correlated to the rest of the FOV. Contour lines indicate $R = \pm 0.2$.	128
8.1	Thrust vs. p_e/p_∞	132
8.2	Thrust vs. altitude for different nozzle expansion ratios	133
8.3	Illustration of a Dual-Bell nozzle	134
8.4	Sketch of the two Dual-Bell operating modes: Sea level mode is illustrated above the axis of symmetry. Altitude mode is illustrated below the axis of symmetry.	135
8.5	Possible interaction of a subsonic (above the axis of symmetry) or a supersonic (below the axis of symmetry) external flow with a Dual-Bell nozzle flow	137
8.6	Illustration of the planar space launcher model with a 2D Dual-Bell nozzle and the measurement locations for PIV and schlieren	138
8.7	2D CFD analysis of the final Dual-Bell nozzle without an external flow. Top: $NPR = 15$. Bottom: $NPR = 20$. The upper symmetry halves of each case indicate the mean static pressure distribution. The lower symmetry halves of each case indicate the mean streamwise velocity distribution.	141
8.8	2D CFD analysis of the final Dual-Bell nozzle with an external flow at $Ma_\infty = 0.80$. Top: $NPR = 15$. Bottom: $NPR = 20$. The upper symmetry halves of each case indicate the mean static pressure distribution. The lower symmetry halves of each case indicate the mean streamwise velocity distribution.	142
8.9	2D CFD analysis of the final Dual-Bell nozzle with an external flow at $Ma_\infty \approx 2$ with $NPR = 5$. The upper symmetry half of indicates the mean static pressure distribution. The lower symmetry half indicates the mean streamwise velocity distribution.	143
8.10	Illustration of the streamwise component of the mean flow field at $Ma_\infty = 0.80$ with $NPR = 4.7$	144
8.11	Illustration of the streamwise component of the mean flow field at $Ma_\infty = 0.80$ with $NPR = 7$ or $NPR_{\text{eff}} = 7.7$	145
8.12	Illustration of a two-point correlation of v' at $Ma_\infty = 0.80$ with $NPR = 7$. The + sign indicates the location that is correlated to the rest of the FOV. Contour lines indicate $R = \pm 0.2$.	146
8.13	Illustration of the streamwise component of instantaneous vector fields at $Ma_\infty = 0.80$ with $NPR = 7$	147
8.14	Graphical illustration of the calculation method of the screech frequency	148
8.15	Illustration of the streamwise component of the mean flow field at $Ma_\infty = 2.00$ with $NPR = 18.8$ or $NPR_{\text{eff}} = 45.1$	150
8.16	Comparison of NPR vs. NPR_{eff} when the total pressure in the TWM is decreased over time	150

LIST OF FIGURES

8.17 Illustration of a two-point correlation of v' at $Ma_\infty = 2.00$ with $NPR = 18.8$.
The + sign indicates the location that is correlated to the rest of the FOV. . . . 151

8.18 Time vs. nozzle mode criterion. Asterisks provide the instance of the schlieren
images provided in figure 8.19. 152

8.19 Schlieren shadowgraph of the nozzle in sea level mode (left) and in altitude
mode (right) 153

8.20 Sketch of the possible driving mechanism for the flip-flop phenomenon at
supersonic external conditions 154

SYMBOLS

Quantities

A	area
C	coefficient
c	speed of sound
D	diameter or thickness
d	distance
e	energy density
F_N	thrust force
f	frequency net force per unit mass
L	Length
H_{12}	shape factor
h	step height atmospheric height
\dot{m}	mass flow rate
p	pressure
q	dynamic pressure heat flux
Ma	Mach number
N	number of
NPR	nozzle pressure ratio
$sNPR$	static nozzle pressure ratio
R	specific gas constant
R_{ij}	Pearson's correlation coefficient correlating e.g. i and j
Re	Reynolds number
S	control surface
SNR	signal-to-noise ratio
Sr	Strouhal number
St	Stokes number
T	temperature
Tu	turbulence level
t	time
U	magnitude of the velocity vector
u	streamwise component of the velocity vector
V	control volume
v	vertical component of the velocity vector
x	streamwise direction
y	vertical direction
y^+	dimensional wall-normal distance

Greek symbols

β	oblique shock angle
Δ	difference
δ_1	displacement thickness
δ_2	momentum thickness
δ_{99}	boundary layer thickness
δ_ω	vorticity thickness
η_K	Kolgomorov length scale
κ	ratio of specific heats
ρ	density
μ	dynamic viscosity
ν	kinematic viscosity
θ	angle of a contour or the change in flow direction
τ	viscous stress
τ_p	relaxation time of a particle across a shock
ξ_p	relaxation distance of a particle across a shock
ϵ	average dissipation rate of turbulent kinetic energy per unit mass
ϵ	nozzle expansion ratio
ω	vorticity

Superscripts

\bar{i}	temporal average of a quantity, e.g. of i
i'	fluctuating component of a quantity, e.g. $i' = i - \bar{i}$
i^*	critical condition of a quantity, e.g. of i

Subscripts

base	base surface on nozzle
e	nozzle exit location
eff	effective
i	index for spatial components
j	index for spatial components
max	maximum
min	minimum
n	nozzle
p	particle
PM	Prandtl-Meyer
r	reattachment
rel	relative
s	screeching
sep	separation
shock	shock

surf	surface
tr	transition
wall	position along wall
0	total quantity e.g. pressure or temperature
∞	quantity at free-stream

Units

[bar]	bar - measure of pressure
[counts]	counts - measure of light intensity on a digital camera sensor
[HBW]	hardness Brinell Wolfram - measure of material hardness
[Hz]	Hertz - measure of frequency
[J]	Joule - measure of work or energy
[K]	Kelvin - measure of temperature
[m]	meter - measure of length
[Pa]	Pascal - measure of pressure
[px]	pixel - measure of length on a digital camera sensor
[s]	second - measure of time
[W]	Watt - measure of power

Acronyms

AFC	active flow control
BFS	backward-facing step
CFD	computational fluid dynamics
CMOS	complementary metal-oxide semiconductor
CNES	French space agency
CW	continuous wave
DEHS	di-ethyl-hexyl-sebacat
DFG	German research foundation
DLR	German aerospace center
DNS	direct numerical simulation
DNW	German-Dutch wind tunnel
ESA	European space agency
FCL	full circular lobes large
FCM	full circular lobes medium
FCS	full circular lobes small
FEM	finite element method
FSL	full square lobes large
FSM	full square lobes medium
FSS	full square lobes small
FOV	field of view
GTO	geostationary transfer orbit

SYMBOLS

HCL	half circular lobes large
KH	Kelvin-Helmholtz
LEO	lower earth orbit
LES	large-eddy simulation
OBC	on-board computer
ONERA	the French aerospace lab
PFC	passive flow control
PIV	particle image velocimetry
POD	proper orthogonal decomposition
PSD	power spectral density
PTU	programmable timing unit
RANS	Reynolds-averaged Navier Stokes
RMS	root mean square
ROI	region of interest
SR	step on a body of revolution
SRI	inertial reference system
SST	shear stress transport
sCMOS	scientific CMOS
TIC	truncated ideal contour
TKE	turbulent kinetic energy
TOC	thrust optimized contour
TWM	Trisonic Wind Tunnel Munich
1D	one-dimensional
2D	two-dimensional
3D	three-dimensional

ABSTRACT

Bolgar, Istvan. Dr. Ing, Universität der Bundeswehr München, 05.11.2019. On the performance increase of future space launchers: Investigations of buffeting, its reduction via passive flow control, and the Dual-Bell nozzle concept at trans- and supersonic flight conditions. Professor: Prof. Dr. rer. nat. habil. Christian J. Kähler.

A turbulent separated shear layer is investigated on a generic space launcher model in sub-, trans-, and supersonic free-stream conditions in order to characterize the fundamental physical phenomena that cause buffeting on a space launcher's afterbody during its ascent. The experimental work was carried out in the Trisonic Wind Tunnel Munich with particle image velocimetry and dynamic pressure measurements. The results show that the so-called step mode is mainly responsible for the high dynamic loads experienced on the reattachment surface aft of a backward-facing step. The loads are most predominant in transonic free-stream conditions. In supersonic free-stream conditions it is shown that only the subsonic part of the boundary layer has a statistical effect on the pressure fluctuations experienced on the reattachment surface.

Subsequently, passive flow control is applied in order to reduce the dynamic loads in trans- and supersonic free-stream conditions. A load reduction of around 35% is achieved with the most efficient geometry, next to a reduction of over 80% in the mean reattachment length. This can be attributed to the imprinting of streamwise vorticity into the separated shear layer, which increases the turbulent mixing downstream of the step. The power spectral density distribution of the pressure fluctuations on the reattachment surface shows that the step mode is measurably diffused with the optimal flow control device.

The successful control of the afterbody aerodynamics allows for the integration of longer nozzle extensions with a higher thrust capacity on a space launcher. Therefore, the interaction of an external flow with a Dual-Bell nozzle flow is investigated at last. At transonic conditions, the interaction of the external flow with the jet plume in sea level mode triggers screeching. In supersonic conditions, a Prandtl-Meyer expansion around the nozzle's lip decreases the external pressure in the vicinity of the nozzle exit by 58%. This causes the nozzle to operate in its altitude mode much earlier than predicted by current design methods, which consider the external pressure to define one of the most important nozzle design parameters, namely the nozzle pressure ratio. Therefore, a corrected formulation of the nozzle pressure ratio is introduced. Furthermore, an interaction between a supersonic external flow with the jet plume triggers the flip-flop phenomenon when the nozzle initially transitions. This yields a Dual-Bell nozzle designed to transition in supersonic flight unfeasible for the application on a space launcher. Future experiments need to verify that a nozzle designed to transition in transonic flight avoids interactions that lead to flip-flop.

KURZFASSUNG

Um die grundlegenden physikalischen Phänomene die das sogenannte "Buffeting" an einer Trägerrakete während ihrer Aufstiegsphase verursachen zu charakterisieren, wird eine turbulent abgelöste Scherschicht an einem generischen Trägerraketenmodell im trisonischen Windkanal München unter Sub-, Trans- und Überschallbedingungen mit der Particle Image Velocimetry und dynamischen Druckmessungen untersucht. Die Ergebnisse zeigen, dass der so genannte "Step Mode" hauptsächlich für die hohen dynamischen Lasten auf der Wiederanlegefläche hinter einer zurückspringenden Stufe verantwortlich ist. Die höchsten Lasten treten bei transsonischen Freistrahbedingungen auf. Bei Überschallbedingungen wird gezeigt, dass nur der Unterschallteil der Grenzschicht einen statistischen Einfluss auf die Druckschwankungen auf der Wiederanlegefläche hat.

Im Anschluss wird passive Strömungskontrolle eingesetzt um die dynamischen Lasten bei Trans- und Überschallbedingungen zu reduzieren. Mit der effizientesten Geometrie werden die dynamischen Lasten um circa 35 % reduziert, während die mittlere Wiederanlegelänge um über 80% verkürzt wird. Dies wird durch das Aufprägen von Längswirbeln in die abgelöste Scherschicht erreicht, welche die turbulente Vermischung stromabwärts der Stufe erhöht. Zusätzlich zeigt die spektrale Leistungsdichteverteilung der Druckschwankungen auf der Wiederanlegefläche, dass der Step Mode mit der optimalen Kontrollmaßnahme aufgelöst wird.

Die erfolgreiche Beeinflussung der Heckströmung führt dazu dass längere Düsenverlängerungen mit einem höheren Schubpotenzial an einer Trägerrakete integriert werden können. Daher wird abschließend die Interaktion einer Außenströmung mit einer Dual-Bell Düsenströmung untersucht. Im Transschall regt die Interaktion zwischen der Außenströmung und der Düsenströmung im Bodenmodus das "Screeching" der Düse an. Bei einer Überschallaußenströmung reduziert eine Prandtl-Meyer-Expansion, um die Düsenlippe herum, den Außendruck in der Nähe des Düsenaustritts um 58%. Dadurch befindet sich die Düse viel früher im Höhenmodus als von den derzeitigen Auslegungsmethoden vorhergesagt wird, welche den Außendruck heranziehen um das Düsendruckverhältnis zu bestimmen, dass eines der wichtigsten Düsenauslegungsparameter darstellt. Daher wird eine korrigierte Formulierung des Düsendruckverhältnisses definiert. Darüber hinaus löst eine Wechselwirkung zwischen einer Überschallaußenströmung mit der Düsenströmung bei der erstmaligen Transition das Flip-Flop Verhalten aus. Daher ist eine Dual-Bell Düse, welche für eine Transition im Überschallflug ausgelegt ist, nicht ohne Weiteres an realen Trägerraketen anwendbar. Zukünftige Experimente müssen an einer Dual-Bell Düse, welche für eine Transition im transsonischen Flug ausgelegt ist, untersuchen, ob die Interaktionen vermieden werden, die zum Flip-Flop Verhalten führen.

1 Introduction

The Ariane 5 space launcher system is Europe's independent access to space. The launcher is a 2-stage rocket comprised of liquid propellant main and upper stages, and two solid propellant boosters. From the beginning of its service life, Ariane 5 has suffered two catastrophic failures that ultimately led to a trade-off in the design to solve the issues at hand. Ariane 5's maiden flight failed due to a software problem. The second catastrophic failure occurred after the launcher system received an updated main engine with a longer nozzle extension. This failure was the result of an aerodynamic interaction of a separated shear layer with the structure of the main engine's nozzle, which caused critical damage to the nozzle structure. Engineers had to settle for a trade-off solution, which reinforced the nozzle structure, adding weight to the system, and reduced the length of the nozzle, decreasing its thrust performance. This trade-off increases the price per unit mass of the payload to be launched into space, decreasing the competitiveness of Europe's launch system on the private market. Therefore, it is of highest priority to find a solution to the root cause of the problem instead of settling for an expensive trade-off.

This work presents a detailed overview of mechanisms that led to Ariane 5's failures, allowing the clear definition of the research aims. This is followed by a demonstration of today's limitations regarding the prediction of fluid dynamic phenomena on space launchers. Subsequently, a description of how the complex shape of an Ariane 5 can be scaled down and simplified, in order to conduct fundamental research, is given. Afterwards, the pertaining aerodynamic phenomena are analyzed within a relevant flight envelope of a space launcher. Those results are a significant addition to the currently available literature on launcher aerodynamics due to the fact that the effect of different free-stream Mach numbers are investigated on the same model and in the same test facility with similar boundary conditions. This is complemented by presenting a passive flow control solution to the aerodynamic problems that arise on Ariane 5. The most successful flow control device achieved a more than 80% reduction in the mean reattachment length of the separated region in the most critical flight condition, a value that has not remotely been achieved in previous literature. Prior to the analysis of a future nozzle concept, the design of a generic rocket nozzle model, its validation, and the interaction of an external flow with a nozzle flow are shown. Since the successful control of the aerodynamics allows for a longer nozzle extension, the feasibility of a novel nozzle concept – the Dual-Bell – is studied in realistic flight conditions later on. A published performance study of Ariane 5 with such a nozzle has shown that a simple change from the currently used nozzle extension to a Dual-Bell would yield a payload capacity increase of 5% on a typical mission. The experiments in this work are the first known investigations where the interaction of the Dual-Bell's nozzle flow

with an external flow is considered. At last, an outlook for future space flight is provided based on the findings of this work. Hence, the upcoming chapters are structured as follows:

- 2 Ariane 5: Mission, early problems, and research questions
- 3 On the prediction of buffeting
- 4 Simplification of a complex problem: A backward-facing step in the Trisonic Wind Tunnel Munich
- 5 The separated shear layer aft at relevant flight conditions
- 6 Load reduction with passive flow control
- 7 Design and validation of a nozzle model
- 8 The feasibility of a Dual-Bell nozzle at relevant flight conditions
- 9 Summary & future outlook

2 Ariane 5: Mission, early problems, and research questions

This chapter gives an overview of the European space launcher Ariane 5 and its typical mission profile. This is complemented by a detailed discussion on the two catastrophic failures the Ariane 5 program has suffered since its maiden flight. Insights from literature help to identify the causes for the failures. Even though the fail mechanisms have been eliminated after each failure, the root cause of these mechanisms still exists on today's launchers. Therefore, one of the research goals of this work is to identify and eliminate the root cause of the failures, which could also allow for future nozzle concepts to be integrated on current space launcher designs. This chapter is structured as follows:

2.1 A typical mission profile of Ariane 5

2.2 Early problems with Ariane 5

2.3 Research questions

2.1 A typical mission profile of Ariane 5

Ariane 5¹ was designed as Europe's access to space, more specifically the geostationary transfer orbit (GTO) with the option to serve lower earth orbit (LEO) with an increased payload. The current version, Ariane 5 ECA, has a payload capacity of more than 10 metric tons for GTO. It is a 2-stage launcher with two solid propellant boosters. The main stage and the upper stage are each propelled by cryogenic liquid oxygen/hydrogen rocket motors. An illustration of the launcher system and its main stage engine is provided in figure 2.1.

¹The information provided in chapter 2.1 has been gathered from Ariane 5's user manual (Arianespace 2016a)

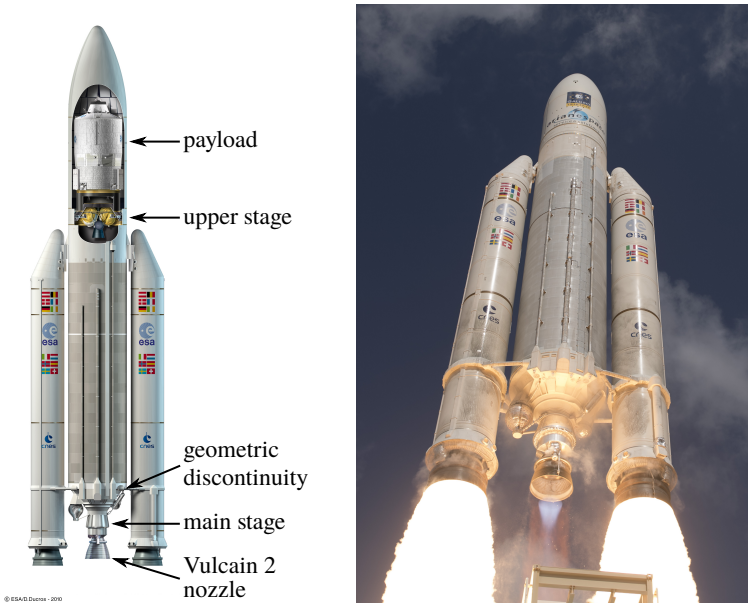


Figure 2.1: Left: Graphical illustration of Ariane 5. Right: Ariane 5 shortly after takeoff. A shear layer separates at the geometric discontinuity and reattaches on the Vulcan 2 nozzle. Images from [ESA²](#).

A typical GTO mission is comprised of four main events (refer to figure 2.2):

1. Ignition of the main stage and the boosters (H0)
2. Booster flame-out and separation (H1)
3. Main stage shutdown and separation (H2)
4. Upper stage shutdown followed by payload delivery (H3)

After ignition of the main stage and the boosters at H0, the launcher carries out a simultaneous acceleration and ascending phase. At the end of this phase the vehicle reaches a velocity of nearly 2000 m/s at an altitude of around 100 km. This phase is considered the most critical phase of flight, where the launch vehicle is traveling in the high-density part of

²Images are reproduced in accordance with [ESA's](#) standard license copyrights.

the atmosphere and has to break the sound barrier. Following the separation of the boosters at H1, the acceleration phase increases the velocity to almost 7000 m/s at an altitude of approximately 200 km. During the final phase, after separation of the main stage at H2, the upper stage mainly increases the altitude of the vehicle to above 600 km while the velocity modestly increases close to 9500 m/s. At this point the upper stage is shutdown and the vehicle continues to travel on its momentum to an altitude of up to 4000 km. A graphical illustration of the typical mission profile is provided in figure 2.3.

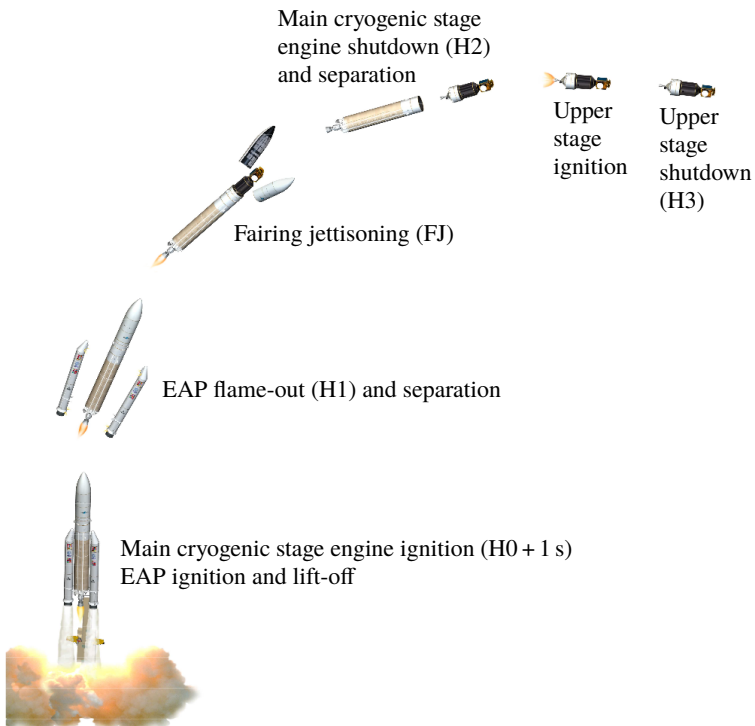


Figure 2.2: Ariane 5 typical sequence of events. Image is originally published in Ariane 5's user manual (Arianespace 2016a)³.

³Images are reproduced with permission from Arianespace.

As previously noted, the critical phase of flight is between H0 and H1. Since its service in 1996, Ariane 5 has suffered two catastrophic failures, both in the early stages of H0+ (refer to chapter 2.2.1 and 2.2.2). This phase is characterized by high mechanical load fluctuations experienced by the main engine's nozzle during the transonic phase of flight (refer to chapter 2.2.3). This typically occurs from around 20 seconds after ignition (H0+20), at which point the launcher is approaching the transonic phase of flight at about 200m/s ($Ma_\infty \approx 0.7$), still being near to the earth's surface. At H0+50 ($Ma_\infty \approx 1.2$), the critical phase has been overcome. From H0+20 to H0+50, the vehicle experiences the highest dynamic pressures and thus, the greatest potential for aerodynamic loads on the structure. Additionally, eigenfrequencies of the nozzle overlap with aerodynamically induced frequencies in close proximity to the nozzle. As a consequence of challenges in this environment, a major focus of this dissertation lies on the critical phase of flight, in and around the transonic regime.

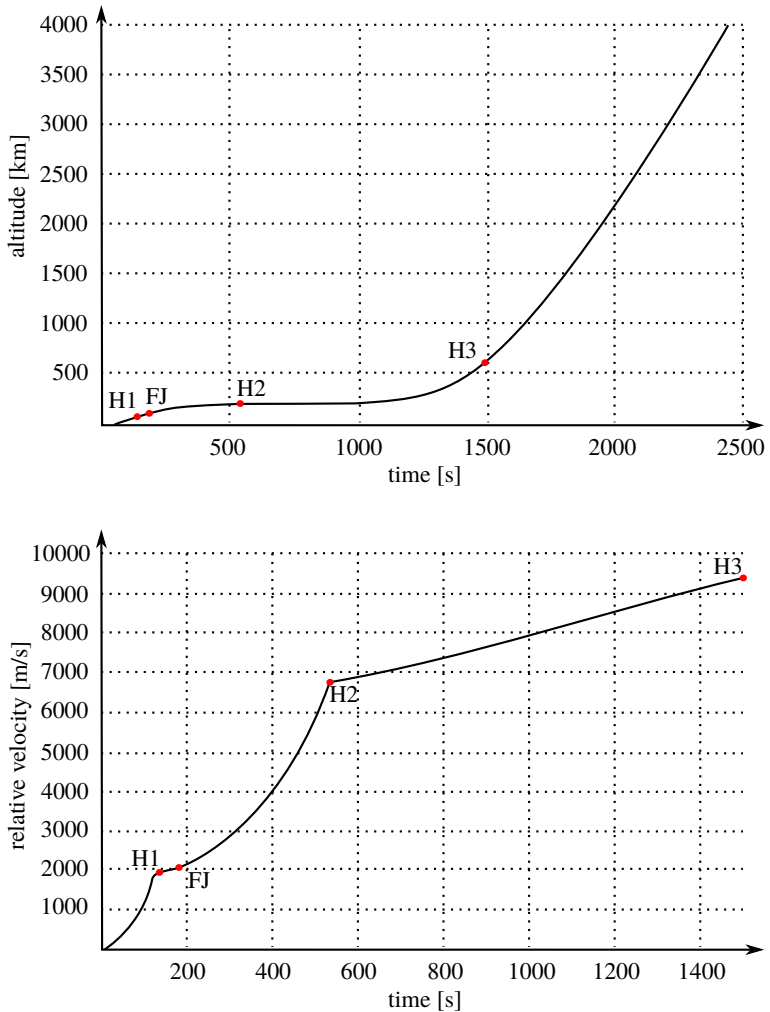


Figure 2.3: Top: Ariane 5 time vs. altitude. Bottom: Ariane 5 time vs. relative velocity. Both plots have been generated in accordance with Ariane 5's user manual (Arianespace 2016a)³

2.2 Early problems with Ariane 5

Since the beginning of its service life in 1996, Ariane 5 has suffered two catastrophic failures. Each of these failures occurred on maiden flights of a new design or a design update, respectively. After each failure, proper steps were taken to improve the design and to eliminate the flaws. Since the last failure in 2002, Ariane 5 has become the most reliable commercial space launcher with 82⁴ consecutive successful launches ([Arianespace 2016b](#)). This section summarizes the failures and their causes, as well as their effects on the design of the space launcher, and the countermeasures that were taken. The main topics in this section are as follows:

2.2.1 Ariane 501 flight VA88

2.2.2 Ariane 517 flight VA157

2.2.3 Ariane 5 buffeting

2.2.1 Ariane 501 flight VA88

On June 4th 1996, Ariane 5 suffered its first catastrophic failure during the initial phase of its ascent on its maiden flight, also known as flight VA88⁵. The launcher with serial number 501 flew a nominal procedure till about 37s after ignition, termed H0+37, when the vehicle suddenly veered off into one direction. Due to the high angle of attack, which a space launcher is not designed for, the self-destruction mechanism of the vehicle was automatically triggered. The self-destruction occurs when the aerodynamic side loads exceed certain limits, causing a mechanical rupture between the links of the solid boosters and the main stage. The vehicle finally suffered complete failure at around H0+39.

The veering off of its flight path was a result of an erroneous thrust vectoring input, initiated by a chain of events. The first signs of anomaly occurred at H0+36.7, when both inertial reference systems (SRI) failed. Subsequently, abnormal motions of the booster engines as well as the cryogenic main engine were recorded, followed by the vectoring of the main engine into an extreme position, causing the severe flight path deviation.

The erroneous thrust vectoring input occurred due to the failed main and backup SRI, which provide the on-board computer (OBC) with critical vehicle attitude information. Amongst others, the OBC is then responsible for controlling the thrust vectoring of the main engine via servo valves and hydraulic actuators. The OBC interpreted the data from the failed main SRI as proper flight data, which called for a full deflection of the main engine.

⁴Launch statistics data cited from [Wikipedia contributors \(2018\)](#)

⁵After the failure, the European Space Agency (ESA) and the French Space Agency (CNES) set up an independent inquiry board to investigate the failure and its causes. The information provided in chapter 2.2.1 has been gathered from the official investigation report by [Lions et al. \(1996\)](#).

Both SRI failed due to a software error, which was not able to convert an excessively high 64-bit floating point into a number that could be represented by a 16-bit integer. This excessively high 64-bit floating point was the horizontal velocity of the Ariane 5. The software for the SRI was designed for Ariane 4 and was carried over to Ariane 5 without changes. However, Ariane 4 did not have such high horizontal velocities as Ariane 5, for which reason the 64-to-16-bit conversion was sufficient. Thus, a software error led to the catastrophic failure of Ariane 501.

2.2.2 Ariane 517 flight VA157

The investigation on Ariane 5's flight 501 also led to other information about potential design flaws on the launch vehicle. One such flaw had been listed as an anomaly in the report by [Lions et al. \(1996\)](#), stating that from H0+22, a gradual development of variations in hydraulic pressure of the actuators of the main engine nozzle took place. These variations in hydraulic pressure had a dominant frequency of approximately 10Hz, or a dimensionless frequency of $Sr_D \approx 0.2$. In other words, the main engine's nozzle was constantly being deflected with a dominant frequency by external forces, that led to the coherent hydraulic pressure variations of the thrust vectoring actuation reservoir.

Despite of the findings from Ariane 501, suggesting the presence of aerodynamically induced coherent loads (refer to chapter [2.2.3](#)), Ariane 5 underwent an evolution which added a longer nozzle extension to the new main engine. According to an ESA technical report ([Coulon 2000](#)), this new main engine, Vulcain 2, provided promising thrust gains of approximately 18%, allowing the advanced Ariane 5 ECA to reach GTO with a payload increase of about 50%.

Ariane 5 with the serial number 517 was the first ECA version of the launcher. It launched on December 11th 2002, on flight VA157 for the first time. Similar to Ariane 501, this launchers maiden flight was also destined to fail. An inquiry board stated two probable causes for the failure of Ariane 517:

- The degraded thermal condition of the nozzle due to fissures in the cooling tubes
- Non-exhaustive definition of loads to which the Vulcain 2 engine is subjected to during flight.

As a result, the nozzle was mechanically reinforced and a thermal barrier coating was applied to the cooling tubes surrounding the nozzle ([Winterfeldt et al. 2005](#)). Additionally, the nozzle extension was slightly shortened by 0.15m, while still remaining significantly longer than Vulcain 1's nozzle ([Geurts 2006](#)).

A publication by CNES and Arianspace employees previously had outlined how buffeting excites nozzle deformation, by which the thermal protection of the nozzle may suffer damage ([Chemoul et al. 2001](#)). This is very much in agreement with the inquiry board's probable causes for the failure and the preventive actions that were taken. Furthermore, [Marie et al. \(2011\)](#) showed how the Vulcain 2 nozzle has two dominant low-frequency structural modes

by which the nozzle deforms. At 10Hz a so-called pendulum mode deforms the nozzle about its pivot point similar to the deflections of a pendulum. At 25Hz nozzle ovalization takes place, by which the nozzle deforms about its circumference from its round shape into an oval. Additionally, [Marie et al. \(2011\)](#) confirmed two peaks in the spectrum of the aerodynamic loads on the nozzle at $Sr_D = 0.2$ & 0.5 with respect to the main stage's diameter, which is equivalent of approximately 10Hz and 25Hz at $Ma_\infty = 0.8$, respectively.

Therefore, the events by which flight VA157 failed can be reproduced with confidence. Aerodynamically induced coherent loads in the transonic regime caused the nozzle to deform, thereby damaging the thermal protection of the nozzle extension, which ultimately led to the thermal failure of the nozzle. This phenomenon did not occur on 13 consecutive missions of the preceding Ariane 5 launches, as those versions of the launcher were propelled by Vulcain 1. The shorter nozzle extension of Vulcain 1 was for one, less susceptible to the pendulum mode due to its shorter length and thus moment arm about the pivot point. Additionally, shorter nozzle length with a smaller nozzle outlet diameter provides for a more rigid structure, which is more resistant to ovalization.

2.2.3 Ariane 5 buffeting

After the exploitation of Ariane 501's data, sufficient evidence led to believe that so-called buffeting was taking place in the aft section of the launcher when entering the transonic phase of flight. In aerodynamics, buffeting is a phenomenon that is characterized by coherent pressure fluctuations that excite the structural modes of an object and thus lead to strong physical oscillations of that object. In the specific case of the Ariane 5, buffeting is taking place on the nozzle structure of the main engine, downstream of the main fairing. The main fairing ends in an abrupt geometric discontinuity ahead of the cryogenic engine. When the launcher is in motion, the flow separates at the end of the main stage, creating a turbulent shear layer which reattaches onto the main engine's nozzle with high spatial and temporal fluctuations. These shear layer fluctuations have several natural frequencies, which eventually cause buffeting. According to flight 501's investigation report's data ([Lions et al. 1996](#)), the aerodynamically induced loads started occurring from 22s into the flight with increasing intensity. According to Ariane 5's user manual ([Arianespace 2016a](#)), at H0+22 the launcher is just about entering the transonic phase of flight at approximately a Mach number of $Ma_\infty = 0.7$ (refer to chapter 2.1 and figure 2.3).

As a consequence of the catastrophic maiden flight of Ariane 501, a series of research studies on the afterbody aerodynamics was launched in Europe. By 1997, the French Aerospace Lab (ONERA) carried out three measurement campaigns on a realistic Ariane 5 model with a 1:60 dimension ([Depuydt et al. 1997](#)). The goal was to characterize the buffeting loads in the transonic regime and to investigate various countermeasures to reduce these loads. The same wind tunnel model, fitted with the Vulcain 2 nozzle variant, was subsequently used for measurements carried out at the German-Dutch Wind Tunnels' (DNW) facilities. These investigations focused on characterizing the aerodynamic loads on

the main engine's nozzle in the high subsonic and the supersonic regimes (Ramiandrasoa 2000). Using the same model setup with the Vulcain 2, another test campaign was finished in 2001, evaluating the dynamic loads on the afterbody and the performance of flow control measures to reduce these (Tafairy 2004). Over the years, this model has been used for many other measurements and publications including the more recent work of Schrijer et al. (2011), Hannemann et al. (2011) and Marie et al. (2011, 2013). Thus, buffeting has been an ever-present issue, especially after the failure of Ariane 517.

Even though the effects of buffeting on the nozzle structure have been managed, making Ariane 5 such a reliable launcher, the preventive actions that were taken to increase the structural strength of the nozzle added weight to the system. This decreases the performance of the vehicle, and with it the profitability as a commercial business tool. Therefore, fixing the root cause of buffeting would be an ideal solution, as it would not detriment the launcher's performance. However, the driving mechanisms behind buffeting have to be understood and predicted, in order to account for them in the design phase. Buffeting has been extensively investigated in various wind tunnel campaigns since Ariane 501, but the predictions on Vulcain 2 were not sufficient for Ariane 517. According to Geurts (2006), the dynamic load results showed restitution values between 18% to 30% when compared to flight data from Ariane 501 and 502, depending on whether a jet plume was integrated into the model. This shows that buffeting is not only a contemporary problem, but also a complex one, and that significantly more research still has to be performed to resolve the basic flow physics governing its aerodynamic origin.

2.3 Research questions

The previous section explained how buffeting still is an omnipresent issue for Ariane 5 today. The currently re-engineered Vulcain 2 nozzle does not perform to its full potential, as the nozzle has been shortened slightly, in order to avoid structural deformation through buffeting. Furthermore, the nozzle structure was mechanically reinforced, which added weight to the space launcher and thereby decreased the payload capacity. Since the flow physics that lead to buffeting still have not been fully understood today, the following research questions arise:

1. What are the major flow phenomena affecting the nozzle structure of a space launcher?
2. If there are several main driving factors for buffeting, which is the most dominant one?
3. Can this phenomenon be eliminated with passive flow control?
4. Assuming it is possible to reduce buffeting effects, is a longer nozzle extension, such as a Dual-Bell, a feasible alternative for future space launchers?

These questions will be answered systematically throughout this dissertation. The first two research questions will be evaluated in chapter 5. Chapter 6 covers the effect of passive flow control devices. Finally, chapter 8 investigates the feasibility of a Dual-Bell at relevant flight velocities of a space launcher. Thus, the aim of this work is to add to the current body of knowledge with respect to separated shear layers, controlling these with passive flow control devices, and to perform elementary studies on Dual-Bell nozzles subjected to realistic flight conditions. The results of this work will not only be useful for rocketry, but also for the design of future aerospace vessels that travel at or above commercial flight velocities.

3 On the prediction of buffeting

This chapter starts out with a brief overview on why the buffeting phenomenon, as it occurred on Ariane 5, cannot be predicted accurately by today's flow simulations. Subsequently, some of the challenges of wind tunnel measurements are discussed, in order to demonstrate why experiments also cannot provide a complete picture of the flow physics on such complex problems. At last, it is discussed how a combination of particle image velocimetry, dynamic pressure measurements, and schlieren shadowgraphy provide for a good compromise when investigating buffeting using today's state-of-the-art experimental measurement technology. This chapter is structured as follows:

- 3.1 Overview of the numerical limitations of today's flow simulations
- 3.2 Overview of experimental challenges with respect to model requirements and measurement techniques
- 3.3 Today's state-of-the-art experimental aerodynamics measurement technology

3.1 Numerical limitations

As the literature from chapter 2.2.3 suggests, most work with respect to predicting buffeting loads on the Ariane 5 were carried out experimentally. For one, this is due to the fact that any numerical simulation would need accompanying experiments to verify the basic modeling quality of the code. More importantly however, this is due to the excessive amounts of computational power necessary to resolve non-stationary effects in an acceptable amount of time. The only computational fluid dynamics (CFD) method that accounts for all spatial and temporal effects is the so-called direct numerical simulation (DNS). In its classical definition (refer to Orszag & Patterson (1972) and Fox & Lilly (1972)), DNS solves six equations in each cell of a discretized computational domain. These so-called Navier-Stokes equations, a set of second order non-linear partial differential equations, are comprised of the continuity equation (refer to equation 3.1), the momentum equation for three dimensions (refer to equation 3.2), and the energy equation (refer to equation 3.3). For compressible flow, the integral form of these equations can be written with the Einstein notation as follows, starting with the continuity equation:

$$\frac{\partial}{\partial t} \int_V \rho dV + \int_S \rho u_j dS = 0 \tag{3.1}$$

with $j = 1, 2, 3$

where ρ is the density of the fluid and u is a scalar component of the velocity vector denoted with index j for the three spatial components of the second term. The temporal term, denoted by $\frac{\partial}{\partial t}$, is integrated over the cell volume dV , whereas the second term, or the convective term, is integrated over the cell's respective surface dS . The momentum equation for a compressible fluid can be written as:

$$\frac{\partial}{\partial t} \int_V \rho u_i dV + \int_S u_j \rho u_i dS + \int_S p dS_i - \int_V \rho f_i dV - \int_S \tau_{ij} dS_j = 0 \quad (3.2)$$

with $i \& j = 1, 2, 3$

where p is the pressure of the fluid, f is the net force on the body per unit mass exerted on the fluid inside the volume, and τ is the deviatoric stress tensor, which describes the diffusion due to viscosity. In this case, i also denotes the three spatial components, however indicating a change of the terms across three separate equations for each spatial component. In the form written above, the momentum equation is also referred to as the Navier-Stokes equation. Finally, the energy equation, or the first law of thermodynamics, can be written as:

$$\frac{\partial}{\partial t} \int_V \rho \left(e + \frac{1}{2} u_i^2 \right) dV + \int_S \rho u_j \left(e + \frac{1}{2} u_i^2 \right) dS - \int_V \rho f_i u_i dV - \int_S \tau_{ij} u_i dS_j + \int_S q_i dS_i = 0 \quad (3.3)$$

with $i \& j = 1, 2, 3$

where e is the energy density and q is the heat flux. To close the equations, an equation of state is specified with the assumption of an ideal gas:

$$p = \rho RT \quad (3.4)$$

where R is the specific gas constant and T is the gases temperature.

Reynolds number's effect on simulation time

The numerical limitations that arise when solving these equations for specific initial boundary conditions on a full-scale space launcher at relevant velocities are based on the Reynolds number and the Kolmogorov scale. The Reynolds number is a dimensionless quantity relating the inertial to the viscous forces of a fluid in motion. Amongst others, this quantity gives important information about the state of the boundary layer and separation bubbles. The idea of investigating the effect of the inertial to the viscous forces and quantifying them was first reported in 1883 in literature by [Reynolds \(1883\)](#). He suggested a proportionality constant with a critical value from which steady fluid motions become unstable. This was later defined as the Reynolds number, such as:

$$Re = \frac{\rho UL}{\mu} = \frac{U_\infty L}{\nu} \quad (3.5)$$

where ρ is the density of the fluid, U is the magnitude of a characteristic velocity, L is the characteristic length, μ is the dynamic viscosity of the fluid, and ν is the kinematic viscosity of the fluid. Depending on the type of flow environment, e.g. an external flow over an airfoil or a pipe flow, different characteristic lengths have to be chosen. Viscous forces dominate a low-Reynolds-number flow. This type of flow is characterized by steady uniform fluid motion and is also known as laminar flow. On the contrary, inertial forces dominate a high-Reynolds-number flow. These tend to produce chaotic eddies or vortices, and other instabilities, or turbulence. Therefore, high-Reynolds-number flows are considered turbulent flows.

The effect of the Reynolds number on simulation time is based on the spatial as well as the temporal discretization of the computational domain. Even though CFD codes operate in a dimensionless environment, the effects of the inertial or viscous forces cannot be non-dimensionalized. [Kolmogorov \(1941\)](#) suggested that from a certain length scale the turbulent kinetic energy carried by eddies is dissipated to heat while viscous forces start to dominate the phenomena. This is described by the Kolmogorov length scale as:

$$\eta_K = \left(\frac{\nu^3}{\epsilon} \right)^{1/4} \quad (3.6)$$

where ϵ is the average dissipation rate of turbulent kinetic energy per unit mass. Hence, the Kolmogorov length scale provides the smallest possible size of structures that have an effect on the flow due to their motion. Therefore the smallest cell size of a DNS mesh should be chosen slightly smaller than the Kolmogorov length scale, in order to resolve the effects of the smallest structures on the overall flow. As the kinematic viscosity is inversely proportional to the Reynolds number, the resolution requirement for a three-dimensional mesh with N_{nodes}^3 number of nodes increases with increasing Reynolds number by:

$$N_{\text{nodes}}^3 \geq Re_\tau^{9/4} \quad (3.7)$$

where the turbulence Reynolds number is characterized by the friction velocity U_τ .

Similarly, as flow velocities increase, thereby increasing the Reynolds number, the unit distance traveled by the fluid in a specific unit time increases. In order to explicitly evaluate the effects of the flow on a specific location in the spatially discretized domain, the domain needs to be discretized temporally as well. Therefore, the time step decreases with increasing Reynolds number, so that the temporal change of the physical quantities at a specific location can be resolved. At the same time, the integral length scale L , containing the motions with most of the kinetic energy, must be resolved. These are the large structures, thus a high number of time steps must be chosen. This is proportional to:

$$N_{\Delta t} = \frac{L}{\eta K} \sim Re_{\tau}^{3/4} \quad (3.8)$$

When combing the computational requirements for the spatial and temporal discretizations, the number of operations increases by the cubic of the Reynolds number:

$$N_{\text{total}} = N_{\text{nodes}} \times N_{\Delta t} = Re_{\tau}^3 \quad (3.9)$$

For reference, the highest Reynolds number DNS simulation published to date by [Eitel-Amor et al. \(2014\)](#) has a Reynolds number of $Re_{\delta_2} = 8300$ with respect to the momentum thickness of the boundary layer δ_2 , or $Re_{\tau} \approx 2500$ with respect to the friction velocity and the boundary layer thickness. The simulated flow was about a simple flat plate on which the computation was performed on 4096 cores in parallel for 10^6 CPU hours. In transonic conditions, an Ariane 5's friction velocity Reynolds number is roughly two orders of magnitude higher, or $Re_{\tau} \approx 250,000$. When neglecting the complexity of the mesh required to spatially discretize an Ariane 5, the total number of operations would increase by six orders of magnitude, or a factor of 1,000,000, according to equation 3.9. Hence, these kinds of fully resolved simulations on full-scale models are simply not feasible today.

3.2 Experimental challenges

3.2.1 Dimensional challenges

Similar to today's numerical methods, experimental aerodynamic measurement methods also have their limitations. The most apparent one is the dimensional limitation. Before full-scale flight tests can be performed on an aerospace vessel, experiments are usually conducted in a wind tunnel environment. Since wind tunnels have finite dimensions, the models' sizes are inherently limited. According to [Couch & Brooks \(1973\)](#) the model's cross section should be on the order of 1% or less of the wind tunnel's cross section, in order to avoid the influence of so-called transonic blockage effects from the wind tunnel walls. Since the energy requirement for the operation of a wind tunnel increases till sonic conditions, transonic wind tunnels usually have smaller cross sections than subsonic wind tunnels. Therefore, models of commercial aerospace vehicles are usually about two orders of magnitude smaller than the actual vessel. For instance, the Ariane 5 model used in the experimental investigations described in chapter 2 had a scale of 1 : 60, which is considered to be a very large model.

Since the size of the model has a direct influence on the Reynolds number (refer to equation 3.5), the density of the fluid surrounding the model has to be increased in order to keep the Reynolds number similar at the same velocity. Depending on the type of facility, the pressure in the test section can be regulated, which has a direct effect on the density of the fluid. Another approach to increase the Reynolds number is to decrease the viscosity of the fluid. [Kilgore et al. \(1974\)](#) introduced a concept in which very advanced facilities,

so-called cryogenic wind tunnels, have the capability to cool a gas to just above its boiling point around 100 K (cryogenic temperatures). This results in a decrease of the viscosity and thereby increases the Reynolds number. Due to the complexity of such a facility, very few of them exist.

The dimensions of the model also influence the measurement equipment and techniques that can be fitted and used, respectively. For instance, typical dynamic pressure transducers have a diameter of about 2 mm and a length of above 15 mm depending on the sensor type. Therefore, placing these kinds of sensors in a model with a thickness or diameter between 25 mm – 50 mm can be challenging, especially when the desired number of sensors grows. Optical measurement methods have to resolve a region of interest. The smaller the model, the higher the magnification through an objective lens becomes. This in turn increases the optical aberrations on the camera's sensor and ultimately leads to a so-called resolution limit (refer to chapter 3.2.2).

In summary, a measurement facility's test section dimensions limit the size of a model. This increases the complexity requirements of that facility, in order to provide sufficiently high Reynolds numbers. The model size's lower limit is then governed by the facilities capabilities as well as measurement equipment and methods.

3.2.2 Measurement techniques

With the decrease of the model's size, the characteristic size of the eddies carrying the turbulent kinetic energy (TKE) decreases, while traveling at the same velocities as their full-scale counterparts. Also, the spatial periodicity of so-called coherent structures (parts of a turbulent flow whose vorticity expression contains orderly components that appear periodically in space and time) decreases leading to an increase in their temporal frequency at a constant dimensionless frequency. This dimensionless frequency was defined by [Strouhal \(1878\)](#) and is referred as the Strouhal number today:

$$Sr = \frac{fL}{U} \quad (3.10)$$

where f is the dominant frequency of the events, L is the characteristic length, and U is the magnitude of a characteristic velocity. Therefore, the sampling rate requirement of the measurement equipment increases inversely proportional to the decrease in the model's characteristic length. On a model with a diameter of 25 mm, the higher dominant frequency occurring at 25 Hz on the Ariane 5 rear section (refer to chapter 2.2.2) would translate to a frequency of around 5000 Hz. According to [Shannon \(1949\)](#), who credited the work of [Nyquist \(1928\)](#), a sampling frequency of at least twice the sources frequency would be required to resolve it properly. For an Ariane model with a 25 mm diameter this would yield a sampling rate of at least 10 kHz. This holds true for sensors, cameras, lasers, or any other measurement equipment used to resolve these phenomena.

Non-intrusive measurement techniques do not require sensors to be fitted to the model, but usually involve the use of cameras. These cameras do not only need to have high

recording rates for temporally resolved acquisitions, but the size of the pixels on their digital sensor determines the image quality. On one hand, large pixels are advantageous for taking high quality images, as a larger pixel surface area can gather more light and therefore provide higher signal-to-noise ratios (*SNR*). On the other hand, the limiting resolution increases with decreasing pixel size as shown in an applied particle image velocimetry (PIV) example by [Kähler et al. \(2012\)](#). Typically, the limiting resolution is a measure of how many line pairs can be resolved in a unit distance, also referred to as line pairs per millimeter (lps/mm). Two lines imaged onto a sensor are distinguishable as two separate entities if they are separated by at least one pixel. In other words, a higher amount of lps/mm can be resolved if the size of a pixel in between two lines decreases. This essentially yields a lower uncertainty, a property that is paramount in a scientific environment.

At high flow velocities, a short exposure time of the camera sensor is desired, in order for the effects to appear stationary versus blurred on the final image. With increasing recording frequencies, the exposure time of a sensor naturally needs to decrease. The issue with short exposure times is that less photons can be accumulated onto a camera sensor, resulting in a low *SNR*. To compensate this problem, a high-energy light source is required to illuminate the region of interest sufficiently.

Lasers are commonly used as a light source in experimental measurement techniques. They provide a monochromatic source of light with a high energy density, allowing them to be focused over very long distances without chromatic aberrations ([Raffel et al. 2018](#)). In general, two main types of lasers are used for aerodynamic experiments: Continuous wave (CW) lasers or pulsed laser. CW lasers have the advantage that they do not need a complex timing unit to trigger pulses at specifically desired instances. The temporal integral of their power over the exposure time of a camera frame is relatively low, however. With increasing power levels of CW lasers, other problems such as fire hazards may arise. Pulsed lasers split up their power into high-energy pulses. With increasing pulsing frequencies, their energy per pulse decreases, limiting the amount of light available for a camera frame.

Overall, it can be concluded that experimental measurement techniques also provide challenges for the prediction of buffeting loads on the Ariane 5. Sensors, such as dynamic pressure transducers provide high-frequency temporal resolutions, but only at point-wise spatial locations. Depending on the read-out speeds of the hardware, these types of sensors provide over 100kHz of temporal resolution. Non-intrusive optical measurement methods, on the other hand, provide high spatial resolutions but are limited to lower temporal resolutions, mostly limited by the light source. Therefore, today's PIV measurements are not temporally resolved at commercial flight velocities with small scale models. Consequently, a solution to the problem is to use a combination of several measurement techniques for a more complete rendering of the phenomena at hand.

3.3 The solution: Particle image velocimetry, high-frequency pressure sensors & high-speed schlieren

The solution for the challenges and limitations summarized above is to conduct quantitative measurements with a combination of high-frequency point-wise pressure measurements and spatially highly resolved velocity field recordings in a controlled wind tunnel environment. The application of dynamic pressure transducers and PIV, respectively, achieves those aims. This allows for a locally temporally resolved overview of the flow phenomena, and a spatially highly resolved statistical overview of its features. Furthermore, the Reynolds numbers that can be reproduced in the experiments are not as limited as they are for numerical methods. Thus, a Reynolds number at which the turbulent flow phenomena in the experiments are comparable to a real space launcher can be achieved. Note that this Reynolds number may still be significantly lower than the one at realistic flight conditions. However, a threshold Reynolds number, from which a change in the turbulent phenomena is negligible, can be reached.

A dynamic pressure sensor gathers electrical resistance information, which is then converted into pressure information via a calibration function of that sensor. The calibration function is usually created in a controlled environment, where a range of known pressures is applied to the back of the membrane of the transducer through a reference pressure tube, while its electrical resistance at each pressure is recorded.

In addition to PIV and pressure measurements, the schlieren technique can complement the desired information of the flow by qualitatively visualizing density gradients. Schlieren shadowgraphy works by illuminating a desired fluid region with parallel light, which gets imaged onto a camera sensor placed into the light path normally. A large density difference in the fluid causes the light to refract along its path, creating regions with varying light intensity on the camera sensor. The changes in light intensity on the image can be categorized into a positive or negative pressure gradient. Therefore, the schlieren technique is especially useful when compressible flow effects, such as shocks or Prandtl-Meyer expansions, are present in the flow. Since this technique is not limited by the frequency of its light source, schlieren recordings can provide a high temporal resolution, which is mostly limited by the frame rate of the camera. Therefore, it can be used to quantify shock oscillations for instance. A drawback of this technique is that the image on the sensor is integrated along the light path and thus provides a spatial average along the axis of the light.

Basic principles of PIV

In 1977, three independent groups ([Barker & Forney 1977](#), [Dudderar & Simpkins 1977](#), [Grousson & Mallick 1977](#)) measured parabolic velocity profiles in laminar tube flow with the application of laser speckle photography, a technique that was initially developed for solid mechanic applications. The first intended use of what is considered PIV today, dates back to 1984, when [Adrian \(1984\)](#) recognized that the illumination of particles by a light

sheet creates images of individual particles instead of speckles. This led to decades of development of PIV as outlined in the review paper by [Adrian \(2005\)](#), ultimately resulting in its widespread popularity today. PIV is a non-intrusive optical measurement technique used to experimentally quantify the velocity in desired region of interest (ROI). The ROI is illuminated by a focused light source and the flow is seeded with tracer particles. The focused light visualizes the particles, while a digital camera can capture multiple images of them as they move with the flow. Between two individual images separated by a known time delay Δt , the particles shift a certain distance. Classically, the particles' displacement is quantified by correlation methods. In standard planar PIV, where two-dimensional particle images are focused onto the camera sensor, the sensor is spatially discretized into multiple interrogation windows consisting of a few pixel in size (e.g. 16×16 pixel). In the most basic form, the particle locations from one frame of such an interrogation window are then cross-correlated with the particle locations and displacements of a second frame captured Δt later. This results in a correlation matrix (array of possible displacements), where the correlation peak signifies the most probable particle displacement for that interrogation window. The projection of the vector of the local flow velocity into the plane of the light sheet (two-component velocity vector) is calculated by taking the magnification into account and dividing the particle image displacement for that interrogation window by Δt . More advanced iterative correlation methods using 'window shifting', 'grid refinement', 'image deformation', etc. exist. An overview of a basic PIV setup is provided in [figure 3.1](#). For a more detailed overview of PIV's system requirements and its various evaluation methods, the reader is referred to the book on "Particle Image Velocimetry" ([Raffel et al. 2018](#)).

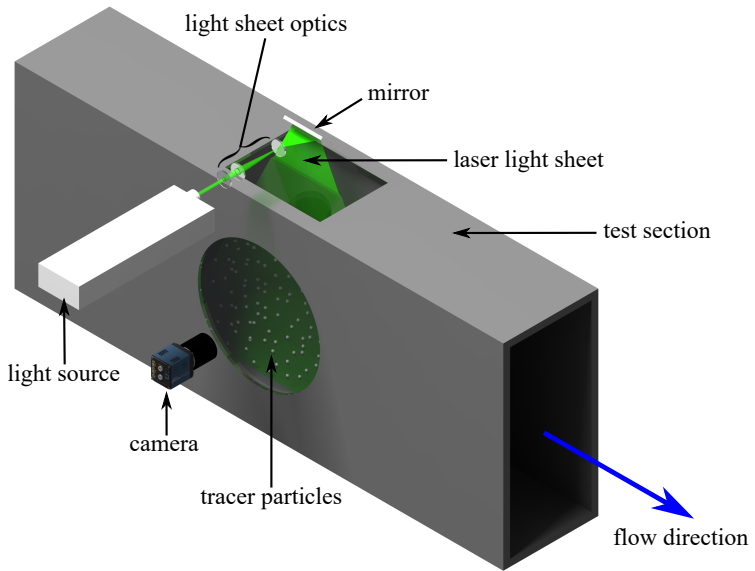


Figure 3.1: Basic PIV system setup

4 Simplification of a complex problem: A backward-facing step in the Trisonic Wind Tunnel Munich

This chapter discusses how the aft section of an Ariane 5 can be simplified to a generic geometry; the backward-facing step. Initially, it is described how the flow physics of the Ariane 5 afterbody can be reproduced on a simple geometry such as a backward-facing step. The latter section of the chapter then provides a thorough discussion of the boundary conditions as well as the flow quality of the experiments analyzed throughout this work. This chapter is structured as follows:

- 4.1 Simplifying the complex afterbody of the Ariane 5 to a backward-facing step
- 4.2 The boundary conditions and the flow quality of the underlying experiments

Part of this chapter is published in [Bolgar et al. \(2018\)](#)¹.

4.1 A backward-facing step as a simplified launcher geometry

The previous section outlined the numerical and experimental difficulties pertaining to full-scale models. Therefore, the Reynolds number needs to be decreased to fulfill the requirements for a feasible computation time, or for experiments, the model needs to be scaled down for it to physically fit in an adequate wind tunnel. Furthermore, it is possible to simplify and generalize the shape of the Ariane 5 rear section. As mentioned in chapter 2, the rear section of the Ariane 5 is characterized by a geometric discontinuity at the end of the main stage's fairing. Buffeting is triggered by the separated shear layer that develops from the geometric discontinuity and attaches onto the main engine's nozzle. Therefore, only a geometric discontinuity followed by a reattachment surface is required to generate and investigate the basic mechanisms of a separated shear layer. Consequently, a backward-facing step (BFS) provides a sufficient geometry that models the rear section of a space launcher, similar to Ariane 5, in a generic manner. Furthermore, a BFS is a very fundamental shape on which a lot of research is published in literature.

A planar BFS model instead of an axisymmetric one was chosen for the experiments of this work. For one, the wind tunnel that was used has a rectangular test section, making it

¹Reprinted by permission from Springer Nature Customer Service Center GmbH: Springer Netherlands, [Flow Turbul Combust](#), *The Effect of the Mach Number on a Turbulent Backward-Facing Step Flow*, Istvan Bolgar, Sven Scharnowski and Christian J. Kähler, © Springer Science+Business Media B.V., part of Springer Nature 2018.

rather ideal for planar models. More importantly, a planar model spanning across the entire test section does not require any sort of additional mounting equipment such as a sting or a sword mount, as would be the case for an axisymmetric model. [Bitter et al. \(2011\)](#) showed that sting mounted models have a tendency to start a pendulum motion around their fixation location. The sword mounts of models, on the other hand, drastically influence the flow conditions ahead of the step into the radial direction as recently shown by [Statnikov et al. \(2016c\)](#). Also, sensors such as dynamic pressure transducers can be fitted into the model more easily. In addition, a planar model is advantageous for setting up planar laser light sheets used for non-intrusive measurements. Finally, a generic quasi-2D shape allows to further simplify the phenomena related to flow separation by removing the radial direction about the model. This is helpful for isolating certain phenomena from three-dimensional effects. Even though the radial degree of freedom is removed from the model, the flow aft of a planar backward-facing step is highly three-dimensional, nonetheless. For instance, the existence of the same modes by which the shear layer statistically modulates over time has been outlined by [Statnikov et al. \(2016b\)](#) for a planar and an axisymmetric BFS. Furthermore, major relevant parameters such as the shear layer instability and its growth rate are also comparable between a planar and an axisymmetric model, as shown by [Deck & Thorigny \(2007\)](#). Therefore, it can be assumed that there is a strong similarity between the driving mechanisms of a planar and an axisymmetric BFS flow, making a planar BFS an adequate research tool for the afterbody aerodynamics of space launchers.

The wind tunnel model

The quasi-2D BFS model used in the underlying experiments of this work is symmetric about its horizontal plane and spans across the entire test section of the wind tunnel. It has a 150 mm long gently curved nose which smoothly transitions into a 100 mm long flat plate prior to the step. The nose's shape was carefully designed by [Statnikov et al. \(2016b\)](#) in order to ensure locally subsonic conditions (at $Ma_\infty = 0.80$) about the model's forebody. The step height is $h = 7.5$ mm and attaches to a 150 mm long splitter plate. The step's width-to-height ratio, or aspect ratio, is 40 : 1, which according to [de Brederode \(1975\)](#) provides an unaffected recirculation region due to sidewall effects. The overall model's thickness is $D = 25$ mm, or 3.7% of the test section's height.

The upper side of the splitter plate was fitted with 24 dynamic pressure transducers (Kulite XCQ-062 with a gauge pressure range of ± 3.5 bar) centered in the spanwise direction of the model. The array of sensors is aligned in parallel to the streamwise direction with a constant spacing of $0.5h$. The first sensor is located $0.5h$ aft of the step, thus the last one is located $12h$ downstream of the step. For reference purposes the model was also fitted with 24 static pressure ports (Pressure Systems DTC ESP-32HD) in the same streamwise locations as the dynamic pressure ports, however offset by 36 mm into the spanwise direction. [Figure 4.1](#) shows essential details of the BFS model.

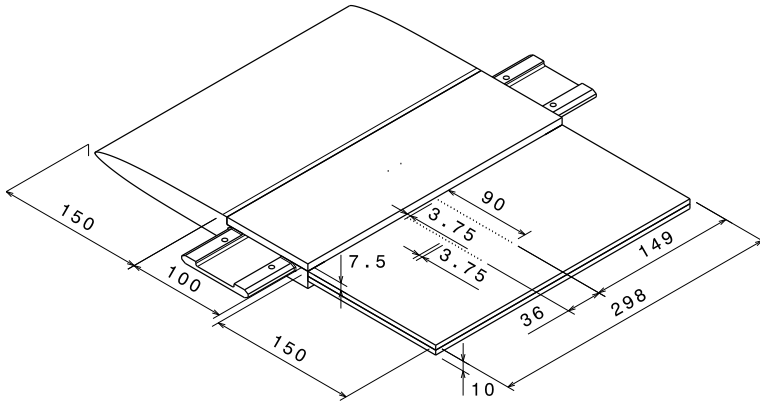


Figure 4.1: Dimensional drawing of the planar space launcher model. Dimensions are provided in units of [mm].

4.2 The measurement facility & its boundary conditions

4.2.1 The Trisonic Wind Tunnel Munich

All experiments were conducted at the Trisonic Wind Tunnel Munich (TWM) at the Bundeswehr University, which is a two-throat blow-down type wind tunnel with an operating total pressure range of 1.2 – 5 bar and a Mach number range of 0.15 – 3.00. Figure 4.2 shows some of the key features of this measurement facility. For the remainder of this paragraph, the numbers in parenthesis refer to that figure. Up to 20 bar (above ambient) of pressurized dry air is stored in two tanks (2), holding a total volume of 356 m³. Typically, the air is a few Kelvin above ambient temperature after the tanks have been pressurized by up to three compressors (1). The test section (6) is 300 mm wide and 675 mm high with suction capabilities at both, the horizontal and the vertical walls. The vertical walls are fitted with suction holes, while the horizontal walls have suction slits. Both use the lower pressure available downstream in the diffuser (7) as their source of passive suction. The test section is surrounded by a plenum chamber that can be opened for easy access to the model. Once the plenum is closed, the gate valve can be opened and the pressurized air is released up to the control valve (4). When in operation, the control valve keeps a steady total pressure in the test via a closed-loop control logic. By setting a desired total pressure, the Reynolds number can be varied between 4 – 80 × 10⁶ m⁻¹. The Mach number in the test section is controlled by a variable diffuser/nozzle (7) downstream of the test section up until sonic conditions. Above this, a variable Laval nozzle (5) can also be adjusted in order to reach supersonic conditions. Both, the diffuser as well as the Laval nozzle can be adjusted with infinite increments. The Laval nozzle always takes the shape of an ideal contour nozzle, providing uniform flow above sonic conditions. Downstream of the diffuser the air is released into the atmosphere through the exhaust tower (8).

For the experiments under investigation, the sidewall suction was taken advantage of below sonic conditions. This not only helps in reducing the low momentum boundary layers on the sidewalls of the test section, but also reduces blockage effects at transonic conditions. The horizontal walls' suction was not applied, as the light sheet for PIV was inserted at an angle from a top window inside the plenum. Slits in the horizontal walls equalize the pressure in the test section with the plenum when the horizontal walls' suction is not in use. However, when it is used, the pressure is reduced resulting in a pressure difference between the test section and the plenum. This would cause the light sheet to diffract due to the difference in the densities, thus changing the location of the illuminated domain with respect to the calibrated plane. However, in order to offset the increasing displacement thickness of the boundary layers on the horizontal walls and to get a rather small pressure gradient in the test section, the horizontal walls were put at a deflection angle, increasing the cross section in the direction of the flow by 25 mm over the test section length of 1.8 m.

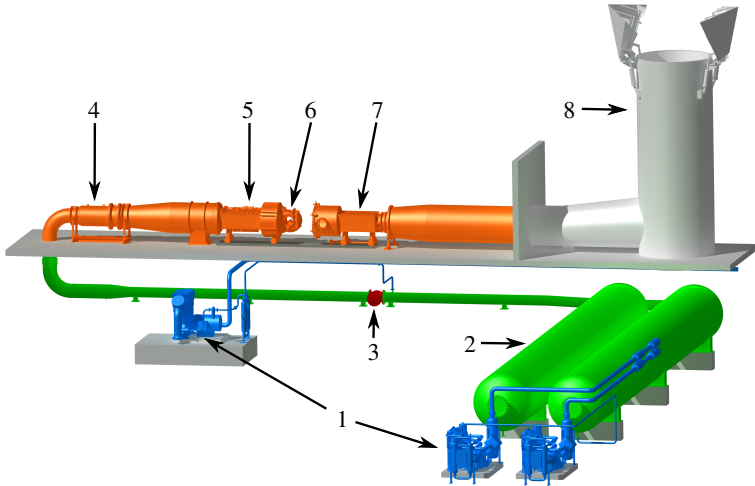


Figure 4.2: Trisonic Wind Tunnel Munich: (1) compressors, (2) tanks, (3) gate valve, (4) control valve, (5) variable Laval nozzle, (6) test section, (7) variable diffuser/nozzle, (8) exhaust tower.

4.2.2 PIV setup used at the TWM

For the statistical and quantitative analysis of the flow, instantaneous flow fields were computed with PIV. The PIV system for the underlying experiments used a Quantel EverGreen double pulse laser with 200mJ per pulse. The light was focused into a 1 mm thick light sheet via optical lenses. The light sheet illuminated di-ethyl-hexyl-sebacat (DEHS) tracer particles with a mean diameter of $1\ \mu\text{m}$ (described in [Kähler et al. \(2002\)](#)), which were added just downstream of the control valve of the wind tunnel. The particles were imaged onto a 2560×2160 pixel sensor of a LaVision Imager sCMOS camera with a 50mm planar objective lens from Zeiss. The PIV system's trigger events were controlled by a LaVision PTU X. Depending on the experimental conditions, several hundred to thousands of double images were recorded at a statistically independent frequency of 15Hz. The time separation between an image pair was between $0.8 - 4.5\ \mu\text{s}$ depending on the free-stream Mach number, limiting the particle image shift to about 10 – 15 pixel. According to [Scharnowski & Kähler \(2013, 2016\)](#), this ensures that the error due to curved streamlines, spatial gradients, and loss-of-correlation due to out-of-plane motion, is sufficiently low.

The data processing consisted of a pre-processing step, the PIV evaluation itself, and a post-processing step. The pre-processing step was comprised of an image shift correction in order to compensate for camera vibrations, and subtracting the background reflections

by means of proper orthogonal decomposition (POD) as described by [Mendez et al. \(2017\)](#). Instantaneous PIV images used for statistical analyses such as the two-point correlations, had a final interrogation window size of 8×8 to 12×12 pixel with 50% overlap, depending on the experiment. The interrogation windows included a Gaussian window weighting and image deformation from LaVision DaVis 8.3. The mean flow fields were then obtained by averaging the instantaneous vector fields. In order to determine the state of the incoming boundary layer ahead of separation, a single-pixel ensemble-correlation method with symmetric double correlations (for more details refer to [Avallone et al. \(2015\)](#)) was applied to obtain a spatially highly resolved mean flow field upstream of the BFS.

4.2.3 Schlieren setup at the TWM

A four-color schlieren system was used to qualitatively visualize density gradients, isentropic compression and expansion waves, and compressible shear layers. The light source of the schlieren system installed at the TWM is a 1.6 kW xenon lamp, from which spectrum' the colors red, green, blue and yellow can be extracted via band-pass filters. The four colors were overlapped with a 4-sided prism mirror. A quad-condenser projected each of the four colors onto their own slit, where the slits for red and green were aligned horizontally, while the slits for blue and yellow were aligned vertically. The slits were placed in the focus of a concave mirror with a focal length of 4000 mm in a classical Z-setup, so that the light aft of the mirror traveled through the side windows of the test section in parallel. On the other side of the test section, the changes in the parallelism of the light were detected. In order for this to work, the light was focused onto so-called knife edges with a second concave mirror before being projected onto a high-speed camera sensor. For a detailed description of the schlieren system installed at the TWM facility, the reader is referred to [Hampel \(1984\)](#).

4.2.4 Free-stream turbulence level in the test section

One of the key features of a wind tunnel is its turbulence level Tu . Historically, this quantity is measured with the hot-wire technique. This technique indirectly measures turbulence through the convective heat transfer rate across the wire. However, compressibility effects make the convective heat transfer rate difficult to quantify. Hence, [Scharnowski et al. \(2019b\)](#) used PIV to quantify the turbulence level in the TWM. The results show that with increasing free-stream Mach numbers the turbulence level decreases from around $Tu = 1.9\%$ at $Ma_\infty = 0.3$ to $Tu = 0.45\%$ at $Ma_\infty = 3.0$. [Figure 4.3](#) provides a complete overview for various free-stream Mach numbers and total pressures. Even though the turbulence level at $Ma_\infty = 0.3$ is relatively high in comparison to facilities intentionally designed for subsonic operation, the turbulence levels are within the accepted range of other subsonic measurements (refer to [Eaton & Johnston \(1981\)](#)). In the transonic regime the turbulence level is around $Tu = 1.3 \pm 0.1$, monotonically decreasing further into the supersonic regime, which increases the quality of the measurement conditions.

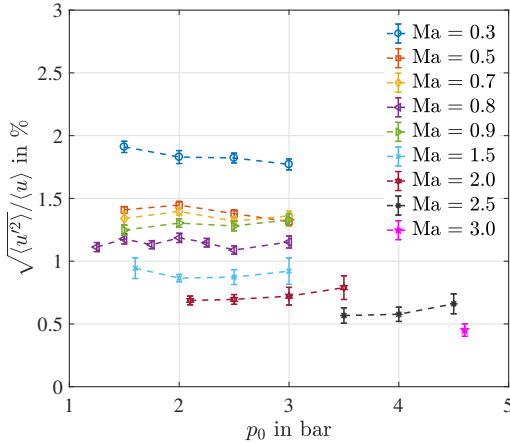


Figure 4.3: Total pressure vs. free-stream turbulence level as a function of the Mach number in the TWM. This figure is published in [Scharnowski et al. \(2019b\)](#).

4.2.5 Mach number distribution in the test section

An important parameter in any wind tunnel measurement is the pressure gradient present in the test section. This is especially true for compressible measurements, as blockage can occur in the test section due to the presence of a model. Blockage occurs when the oncoming transonic flow becomes locally supersonic in the test section due to the acceleration around the model. When this locally sonic flow acts against a positive pressure gradient, a normal shock naturally forms and "blocks" any additional mass flow through the facility. As the free-stream's pressure and its Mach number can be related isentropically (refer to equation 4.1), the Mach number distribution in the test section gives a direct indication of whether blockage has been reached anywhere in the test section.

$$\frac{p_0}{p_\infty} = \left[1 + \frac{\kappa - 1}{2} Ma_\infty^2 \right]^{\frac{\kappa}{\kappa - 1}} \quad (4.1)$$

where p is pressure, Ma is the Mach number, and κ is the ratio of specific heats. Blockage has to be avoided, since the indicated Mach number referenced to a certain pressure sensor can be vastly different to the local Mach number surrounding the model. Also, blockage is accompanied by a total pressure drop in the test section due to the fact that any process across a shock is not isentropic. Figure 4.4 shows the local Mach number along the test section, measured on the bottom wall. These distributions were recorded with the model

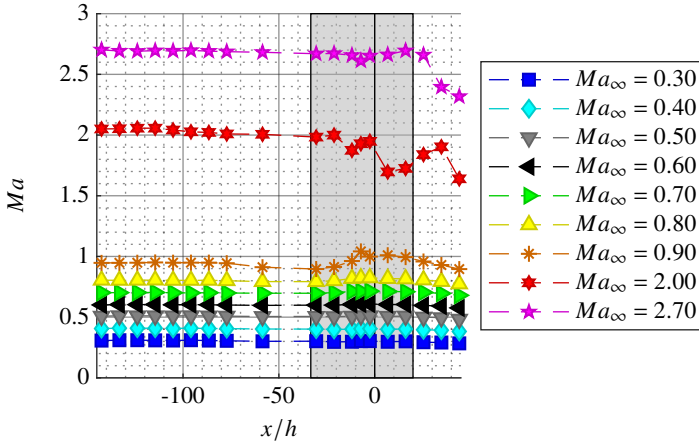


Figure 4.4: Mach number distribution within the test section referenced to a static pressure probe at $x/h \approx -30$

described in chapter 4.1 placed into the test section. For the other physical quantities and their standard deviations refer to table 5.1.

Right away, the free-stream Mach numbers 2.00 & 2.70 distinguish themselves from the other free-stream Mach numbers, while $Ma_\infty = 0.90$ is also a lot different than the other runs. For the $Ma_\infty = 2.00$ case, the sudden drop in the Mach number at $x_{\text{wall}}/h \approx -20$ is due to the formation of a separated shock in front of the model's nose, which reaches the horizontal walls ahead of $x_{\text{wall}}/h \approx -12$. At this point the shock has already lost intensity and is rather a Mach wave, which is reflected back towards the center of the test section. Due to an acceleration over the model's nose followed by a compression fan where the nose's curvature reduces, the Mach number first increases from $x_{\text{wall}}/h \approx -12$ till $x_{\text{wall}}/h \approx -2.5$ and then decreases strongly till $x_{\text{wall}}/h \approx 7$. At this point the effect of the expansion fan around the step can be noticed till $x_{\text{wall}}/h \approx 35$, as the Mach number along the wall rises. Finally, the oblique shock stemming from the recompression on the model's reattachment surface causes the lastly portrayed Mach number drop along the horizontal walls. A similar trend can be seen for the $Ma_\infty = 2.70$ case, however with much lower Mach number changes as the angle of the oblique/reflected shock and expansion waves are much steeper, thus reducing their intensities. It can also be seen that the final Mach number drop occurs earlier at $x_{\text{wall}}/h \approx 16$. Note that the Mach number changes along the wall can be seen further downstream as they occur on the model, due to the angles of the compression/expansion waves, thus the location of impact on the Mach number changes. It can be summarized that for the supersonic cases the Mach number distribution in the test section is as expected and of good quality. The changes in the Mach number induced by

the model do not affect the measurement domain itself. Furthermore, the reflected shock from the wind tunnel wall does not interfere with the measurement domain either.

At $Ma_\infty = 0.9$, the presence of the model induces a Mach number drop in the test section upstream of itself from $x_{\text{wall}}/h \approx -87$ to $x_{\text{wall}}/h \approx -30$. From there onwards, the expansion over the nose's curvature can be seen till $x_{\text{wall}}/h \approx -7$. At that point, the Mach number suddenly drops again till $x_{\text{wall}}/h \approx -2.5$. This is due to the formation of a nearly normal shock as a result of the compression waves meeting, which are created by the decreasing curvature, as illustrated in the schlieren image in figure 4.5 in the middle. Therefore, the definition of the free-stream Mach number $Ma_\infty = 0.9$ should be viewed with caution, as blockage occurs around the model. Thus, the Mach number aft of the shock, just ahead of the step, is higher than the free-stream Mach number referenced at $x/h \approx -58.5$. By means of PIV it was determined to be $Ma \approx 1.00 \pm 0.01$ at $x/h = -1$. After the shock, the flow then expands through an expansion fan around the BFS till $x_{\text{wall}}/h \approx 7$, from where the oblique recompression shock/fan creates a drop in the wind tunnel wall Mach number till the end of the test section. Again, this can be seen clearly in the schlieren image in figure 4.5 in the middle. In order to be able to compare the pressure dynamics downstream of the step between the various free-stream Mach numbers, the values were normalized with the total pressure, which is set upstream of the model. As the normal shock on the model surface creates a loss in the total pressure, the pressure ratios provided in chapter 5.3.3 in figure 5.12 at $Ma_\infty = 0.9$ are slightly smaller than they would normally be, since they were divided by the total pressure ahead of the normal shock.

At $Ma_\infty = 0.80$ a slight expansion from the flow accelerating over the model's nose can be noticed without a stationary shock or blockage. This statement is supported by the schlieren image in figure 4.5 at the top. Even though there is an increase in the Mach number by approximately 2% ahead of the step, the pressure gradient in the test section is satisfactory. All other subsonic free-stream Mach numbers lower than $Ma_\infty = 0.80$ have nearly no gradient in the Mach number distribution.

4.2.6 Shock-free model in transonic flow and supersonic shock reflection

In the previous section it was discussed how blockage has to be avoided for reliable measurement conditions. For high quality incoming flow conditions ahead of the region of interest, it is also important to keep the flow close to the model's surface locally below the sonic barrier, when the free-stream conditions define the flow to be below sonic. As mentioned in chapter 4.1, the model under investigation was carefully designed with a gently curved nose, which ensures subsonic conditions locally at $Ma_\infty = 0.80$.

When conducting supersonic experiments, a shock, either oblique or separated, gets generated at the model's nose. This shock will get reflected at the wind tunnel walls back towards the model. For these kinds of measurements it is an important criterion that the reflected shock gets reflected downstream of the ROI.

Two transonic free-stream Mach numbers ($Ma_\infty = 0.80$ & $Ma_\infty = 0.90$) as well as the

supersonic free-stream Mach number ($Ma_\infty = 2.00$) were measured with the schlieren system qualitatively, visualizing the density gradients in the horizontal direction with only two colors (red for a positive density gradient and green for a negative density gradient). Table 5.1 provides a more detailed overview of the wind tunnel boundary conditions.

Figure 4.5 at the top shows the shock free design of the nose at $Ma_\infty = 0.80$, while no blockage is present at any portion across the model. In the middle of this figure, at $Ma_\infty = 0.90$, a nearly normal shock is present ahead of the step, indicating that the test section has reached blockage. Furthermore an expansion is also visible in the black zone about the step. This indicates that the flow accelerates aft of the normal shock to just above sonic conditions, which is in agreement with the PIV data as well as the Mach number distribution in the test section, shown in chapter 4.2.5. The two lambda shocks, one forming ahead of the step and the other one forming due to reattachment, are both stable in time. This is also the case for the bow shock and the recompression shock at $Ma_\infty = 2.00$ at the bottom of figure 4.5. Here it can also be seen that the reflected shock at $Ma_\infty = 2.00$ does not interfere with the measurement domain for PIV or the pressure ports, as it gets reflected past the bounds of the schlieren image. Note that the wind tunnel wall would be located at $y/h \approx 45$ in the images.

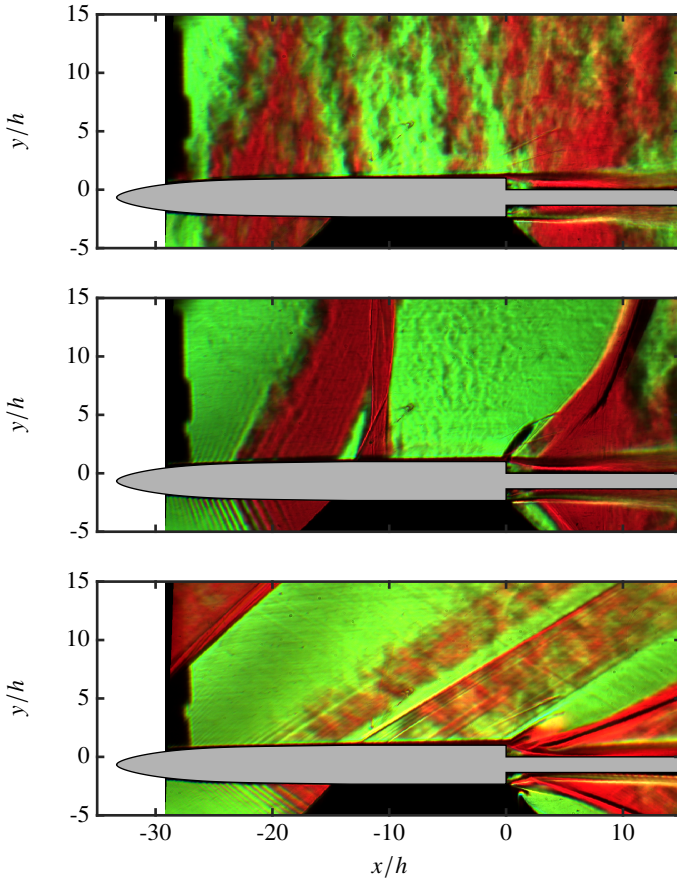


Figure 4.5: Instantaneous schlieren recordings showing the density gradients in the horizontal direction at $Ma_\infty = 0.80, 0.90, \& 2.00$ from top to bottom. Green to red corresponds to increasing density in the streamwise direction while red to green corresponds to decreasing density.

4.2.7 Incoming boundary layer

Characterizing state of the boundary layer is yet another important criterion when conducting experimental measurements. The incoming boundary layer was evaluated at $x/h = -1$ using single-pixel ensemble-correlation as mentioned in chapter 5.2.2. This allowed for a spatial resolution of $35 \mu\text{m}$ per vector in the wall-normal direction, while the first reliable vector was at $\approx 100 \mu\text{m}$ due to wall reflections and loss of seeding. The rest of the boundary layer was extrapolated linearly towards the wall, allowing to estimate the upper limits of the displacement and momentum thicknesses. The boundary layer parameters of the thickness δ_{99} , the displacement thickness δ_1 , momentum thickness δ_2 , the shape factor H_{12} , and the momentum thickness Reynolds number for the various Mach numbers are listed in table 4.1. For all investigated Mach numbers, the incoming boundary layers were turbulent according to [Schlichting & Gersten \(2006\)](#), as the shape factor H_{12} is around 1.4. Since the densities in the boundary layer cannot be solely extracted with PIV, the displacement thickness was determined by using the incompressible definition for all cases:

$$\frac{\delta_1}{h} = \frac{1}{h} \int_1^{\infty} \left[1 - \frac{\bar{u}(y)}{\bar{u}_{\delta_{99}}} \right] dy \quad (4.2)$$

where h denotes the step height, \bar{u} is the mean streamwise component of the velocity, and $u_{\delta_{99}}$ signifies the mean streamwise velocity at the outer edge of the boundary layer. Similarly, the incompressible definition for the momentum thickness was used:

$$\frac{\delta_2}{h} = \frac{1}{h} \int_1^{\infty} \frac{\bar{u}(y)}{\bar{u}_{\delta_{99}}} \left[1 - \frac{\bar{u}(y)}{\bar{u}_{\delta_{99}}} \right] dy \quad (4.3)$$

The shape factor H_{12} was then determined by the ratio of the two:

$$H_{12} = \frac{\delta_1}{\delta_2} \quad (4.4)$$

Table 4.1: Incoming boundary layer parameters at $x/h = -1$

Ma_{∞}	$U_{\infty} [\frac{\text{m}}{\text{s}}]$	$\frac{\delta_{99}}{h}$	$\frac{\delta_1}{h}$	$\frac{\delta_2}{h}$	H_{12}	Re_{δ_2}	Re_h
0.30	≈ 102	0.40	< 0.061	< 0.045	≈ 1.36	≈ 2600	$\approx 58,000$
0.50	≈ 167	0.37	< 0.062	< 0.041	≈ 1.53	≈ 3700	$\approx 90,000$
0.80	≈ 258	0.35	< 0.057	< 0.041	≈ 1.39	≈ 7400	$\approx 180,000$
0.90	≈ 285	0.34	< 0.053	< 0.035	≈ 1.53	≈ 6200	$\approx 177,000$
2.00	≈ 511	0.47	< 0.056	< 0.038	≈ 1.49	≈ 7900	$\approx 208,000$

A boundary layer thickness to step height ratio of around $\delta_{99}/h = 0.4 \pm 0.1$ signifies a strongly perturbed flow, according to [Bradshaw & Wong \(1972\)](#) (refer to chapter 5.1).

Hence, the turbulent structures from the boundary layer are significantly altered within a recognizable shear layer.

4.2.8 Tracer particle response across shocks

When conducting PIV measurements with the presence of shocks, it is known that the tracer particles do not decelerate suddenly, such as the discontinuity due to a shock would suggest. They rather need a certain distance and time for adjusting to the local flow conditions as suggested by [Ross et al. \(1994\)](#). This lag can be quantified by the relaxation distance ξ_p and time τ_p . For all supersonic cases as well as the $Ma_\infty = 0.90$ case in this work, a recompression shock forms on the reattachment surface, as the locally supersonic flow gets deflected into a parallel direction with respect to the reattachment surface. For both, the $Ma_\infty = 0.90$ and 2.00 cases, $\xi_p \approx 0.6$ mm and $\tau_p \approx 1.9$ μ s. These values are nearly identical with previous findings on di-ethyl-hexyl-sebacat (DEHS) tracer particles from [Ragni et al. \(2011\)](#). This yields a Stokes number of $St = 0.063$, where the Stokes number is defined as $St = \tau_p / \tau_{\text{flow}}$ with $\tau_{\text{flow}} = \rho / U_\infty$. According to [Raffel et al. \(2018\)](#), this yields an root mean square (RMS) tracking error below 1 %. Furthermore, as the interrogation window sizes are smaller than the relaxation distance while the separation time between two frames is on the order of the relaxation time (refer to chapter 5.2.2), the analysis thereof can be considered reliable, apart from a small region around the shock (≈ 1 vector), according to [Ragni et al. \(2011\)](#). The interrogation windows on top of the shock also suffer from correlation errors due to the increase in particle image density across the shock, which yields a higher weighting of the slow velocity aft of the shock in the correlations. Therefore, the velocity vector across the shock is generally underestimated in its magnitude, which counteracts the effects of the particles' lag. As a result, the velocity fields closely portray the reality ahead and aft of the shocks, while the shocks themselves are shown with a width of ξ_p on the PIV images.

5 The separated shear layer at relevant flight conditions

This chapter provides an overview of the backward-facing step model investigated in the low subsonic, through the transonic, into the supersonic regime. As previously noted in chapter 4, a BFS is used to simplify the aft geometry of a space launcher to a generic shape that produces all relevant flow effects. The major phenomena exciting buffeting during the transonic phase of flight for the Ariane 5 are very similar to the phenomena occurring aft of a BFS. Furthermore, it is important to characterize the behavior and change of the underlying flow physics when going from one Mach regime into the other, as a space launcher has to travel through all of these regimes during its ascent. This allows for reliable conclusions on why buffeting is most critical in the transonic phase. Additionally, more precise predictions can be made on whether other critical phenomena occur later in the Mach number range, that are currently being overlooked due to the severity of buffeting. This chapter is structured as follows:

- 5.1 Literature review of BFS flow and the modes occurring aft of such
- 5.2 Test cases and analysis methods
- 5.3 Detailed overview and discussion of the results
- 5.4 Summary and conclusions of the gathered insights

Part of this chapter is published in [Bolgar et al. \(2018\)](#)¹.

5.1 Literature review of separated shear layers

A flow around a backward-facing step (BFS) has been of scientific interest for decades for various reasons. For one, it provides a well-defined location for the onset of flow separation and thereby a shear layer with reattachment around a simple geometry. Therefore, phenomena regarding the flow separation, including the generation and amplification of flow disturbances, the reattachment thereof, and shear layer dynamics can be studied in detail with such a simple shape. Another reason is that today the flow physics of the wake aft

¹Reprinted by permission from Springer Nature Customer Service Center GmbH: Springer Netherlands, [Flow Turbul Combust](#), *The Effect of the Mach Number on a Turbulent Backward-Facing Step Flow*, Istvan Bolgar, Sven Scharnowski and Christian J. Kähler, © Springer Science+Business Media B.V., part of Springer Nature 2018.

of a BFS, such as the modes responsible for the load fluctuations, have not been fully understood, as stated by [Statnikov et al. \(2016a\)](#).

In 1972, [Bradshaw & Wong \(1972\)](#) compiled a review paper on the reattachment and relaxation of turbulent shear layers. This work played a substantial role in making the BFS the most common geometry for research on separated flows. Before this, a lot of experimental work on separation bubbles was carried out on rectangular obstacles placed on a flat plat, fences, ramps and also BFS to name a few. According to [Bradshaw & Wong](#), a shortcoming of many previous experiments was the abundance of over-complicated geometries. Thus, a simpler and more generic geometry was necessary for scientists to be able to reproduce the physical phenomena and also to be able to compare results with one another. The authors proposed a relation of the step height h vs. the boundary layer thickness δ_{99} in order to classify the severity of the perturbation of the flow. Weak perturbation was defined where $h/\delta_{99} \ll 1$, strong perturbation where $h/\delta_{99} \approx 1$, and overwhelming perturbation where $h/\delta_{99} \gg 1$. Back then, it was already evident that strong perturbations, as present in the current work (refer to chapter 4.2.7), are the most difficult ones to understand. It was also suggested that the relaxation of the boundary layer to its classical formulation takes at least 30 shear layer thickness downstream of reattachment, which is generally defined as ([Brown & Roshko 1974](#)):

$$\delta_{\omega}(x) = \frac{\bar{u}_{\max}(x) - \bar{u}_{\min}(x)}{[d\bar{u}(x)/dy]_{\max}} \quad (5.1)$$

where $\delta_{\omega}(x)$ is the shear layer thickness, also sometimes referred to as the vorticity thickness, which is calculated by dividing the maximum mean velocity difference at a streamwise location by the maximum gradient of the mean velocity normal to the surface.

Into the eighties an increasing number of articles on separated flows, especially on BFS, were published. Therefore [Eaton & Johnston \(1981\)](#) summarized the findings from work on turbulent BFS flows from the two previous decades in an elaborate review paper. With the wide range of initial boundary conditions, the mean reattachment locations varied between $4.9h - 8.2h$ for the various experiments. The important fact that the reattachment location of the shear layer temporally fluctuates was already confirmed by this time by [Abbott & Kline \(1962\)](#). [Eaton & Johnston](#) considered five different criteria which would explain the large spread between the mean reattachment lengths for different experiments: (1.) the initial state of the boundary layer, (2.) the initial boundary layer thickness, (3.) the free-stream turbulence, (4.) the pressure gradient in the test section, (5.) the aspect ratio (width-to-height) of the step. For the underlying experiments these quantities have all been summarized in chapter 4. [Eaton & Johnston](#) recommended that, at the time, future work should focus on understanding the low-frequency motions of the shear layer, which they predicted to be very important to engineering applications.

The effect of the boundary layer state on the reattachment length was investigated by [Eaton et al. \(1979\)](#). The state of the boundary, being either laminar or turbulent, had a significant effect on the reattachment length. According to that work, the reattachment

length becomes independent of the Reynolds number once the boundary layer ahead of the step is fully turbulent.

[Badri Narayanan et al. \(1974\)](#) studied the effect of different step heights on the pressure distribution aft of BFS. Since all models were of the same length, the boundary layer thickness remained constant. The resulting pressure distributions were in good agreement with each other, regardless of the step height. Since the reattachment location can be derived from the pressure distribution on the reattachment surface, it can be concluded that the boundary layer thickness has a relatively weak effect on reattachment length.

The effect of the free-stream turbulence on the reattachment length can be derived from several plots in [Eaton & Johnston \(1981\)](#). Results from various experiments were compared in these plots, which showed a trend that the reattachment length decreases with increasing levels of free-stream turbulence. As [Eaton & Johnston \(1981\)](#) mentioned, this observation was in agreement with measurements in a plane-mixing layer by [Patel \(1978\)](#), who observed an increasing growth rate of the plane-mixing layer with increased free-stream turbulence.

The fact that reattachment is highly sensitive to the pressure gradient present in the test section was shown by [Kuehn \(1980\)](#). His results demonstrate that the pressure gradient can alter the reattachment location by as much as $\pm 1h$. One of his hypotheses was that the different pressure gradients in various published measurements were the major reason for the large deviations in reattachment lengths.

The effect of the step's aspect ratio was investigated by [de Brederode \(1975\)](#). The results showed that for aspect ratios smaller than 10:1, the step's width-to-height ratio has an influence on the reattachment length, for both, laminar and turbulent boundary layers ahead of the step. However, for aspect ratios greater than 10:1, this effect becomes negligible, thus the reattachment length remains constant for specific flow conditions, independent of the step's aspect ratio.

Subsequently, the research on shear layers moved onto investigating the low-frequency motions thereof. [Ho & Huerre \(1984\)](#) published an extensive review paper of perturbed shear layers. The work analyzed the dynamical processes in mixing- and free shear layers. Amongst others, three major dynamic processes of the shear layer were identified: (1.) A laminar shear layer is initially dominated by a linear instability mechanism. It is caused by the periodic generation of Kelvin-Helmholtz instabilities. These instabilities were recognized as two-dimensional vortical structures that exponentially grow into the downstream direction. (2.) A nonlinear instability regime exists downstream of the linear one, where the Kelvin-Helmholtz vortices evolve into a periodic array of compact spanwise vortices. (3.) These compact vortices pair into larger structures with their neighboring vortices. This is the primary process by which a mixing layer grows into the downstream direction.

On a laminar BFS flow, [Hasan \(1992\)](#) investigated the dynamics of the reattaching shear layer. He found two distinct instability modes. The first one occurred at a normalized frequency or Strouhal number of $Sr_{\delta_2} \approx 0.012$ with respect to the momentum thickness of the boundary layer. The other one occurred at $Sr_{\delta_2} \approx 0.004$, or $Sr_h \approx 0.185$ with respect

to the step height. The high-frequency instability of the two is found in close proximity of separation and was termed the 'shear layer mode'. The low-frequency instability exists further downstream and was termed the 'step mode'. The shear layer mode would be comparable to the mixing layer's linear instability mechanism (refer to (1.) in the paragraph above). According to [Hasan](#), the merging of vortices reduces the mode's frequency to the step mode's frequency, which is identical to the vortex pairing process in shear layers (refer to (3.) in the paragraph above). This trend was also observed by [Eaton & Johnston \(1980\)](#), who reported a rapid decay in the frequencies with increasing distance towards the reattachment location. However, [Hasan](#) also stated that the decrease in frequencies past the reattachment location is not due to the pairing of vortices, but is rather caused by the upstream sweeping of large eddies. According to this theory, the mean reattachment location represents a splitting location where part of the shear layer's eddies continue to move downstream, whereas the other portion moves upstream within the recirculation region. Due to the sensitivity of the streamwise measurement location, the step mode has been reported over a wide spectrum in literature, ranging from $Sr_{L_r} \approx 0.6 - 1.0$ with respect to the reattachment length L_r ([Cherry et al. 1984](#), [Driver et al. 1987](#), [Heenan & Morrison 1998](#)). Therefore it is important to observe this quantity as a function of the streamwise position.

Underneath the spanwise vortex street, the recirculation zone exhibits its own dynamics. [Driver et al. \(1987\)](#) found a 'flapping' motion of the shear layer, by which the entire separation bubble enlarges with an abnormally long instantaneous reattachment, and contracts with a short one. The scale of this motion was found to be bigger than the largest eddy, which was said to be approximately one step height in diameter. The amplitude of flapping was estimated to be on the order of 20% of the shear layer width. At the same time it was established that flapping does not contribute much energy to the overall fluctuations taking place in the flow field. The major part of the kinetic energy contribution was verified to reside in the characteristic vortex roll up process (shear layer mode) and the pairing of vortical structures (reduction of the frequency to the step mode) at $Sr_{\delta_\omega} \approx 0.2$ with respect to the vorticity thickness δ_ω . According to [Hasan \(1992\)](#), the flapping mode could be responsible for splitting the shear layer structures into up- and downstream moving eddies.

With the help of a microphone array, [Lee & Sung \(2001\)](#) investigated the pressure fluctuations aft of a BFS. He also detected the low-frequency flapping mode. This mode is predominant between $Sr_h \approx 0.01 - 0.015$ with respect to the step height, or $Sr_{L_r} \approx 0.1$, which is very similar to the findings of [Cherry et al. \(1984\)](#), who investigated separated flows aft of a forward-facing step. It was concluded that this mode is responsible for a periodic change in the reattachment location by the flapping motion of the shear layer.

Next to the flapping mode at $Sr_h \approx 0.01$, [Statnikov et al. \(2016a\)](#) showed the existence of a high-frequency 'pumping' mode within the recirculation zone, where the reattachment location is relatively steady while the recirculation region pumps at $Sr_h \approx 0.07$ around the mean reattachment location. The pumping mode has also been shown to exist on a scaled version of the Ariane 5 launcher and an axisymmetric model (refer to [Hannemann et al.](#)

(2011), Schrijer et al. (2011, 2014)). Statnikov et al. also showed that these two modes exhibit a large periodic motion into the spanwise direction with a dominant wavelength of around two step heights, thus renaming these modes into 'cross-flapping' and 'cross-pumping'. Note that pumping in that work refers to the classical definition of flapping and vice versa.

Figure 5.1 provides a graphical illustration of the dynamics taking place aft of a BFS, as described in the paragraphs above. The time-averaged phenomena occurring aft of a BFS are illustrated in figure 5.1 at the top. The flow over a BFS separates at the geometric discontinuity and reattaches on the lower surface further downstream. Upstream of the reattachment location, a recirculation region develops, where the flow is separated by definition. In the close vicinity of the base of the step, a small secondary recirculation zone exists. From the point where the flow separates, a shear layer develops between the main flow and the recirculation region. The shear layer itself, as well as the recirculation region, exhibits dominant temporal dynamics, which are characterized by coherent phenomena, also referred to as modes. These phenomena are experienced in form of pressure fluctuations on the reattachment surface. The step mode originates from the shear layer instabilities, such as is illustrated in figure 5.1 at the top. The flapping mode is characterized by a period change in the reattachment location of the shear layer, as depicted in figure 5.1 in the middle. The pumping mode (refer to figure 5.1 at the bottom), on the other hand, is characterized by a pumping motion of the shear layer, which results in the growth and shrinkage of the reverse flow region normal to the reattachment surface.

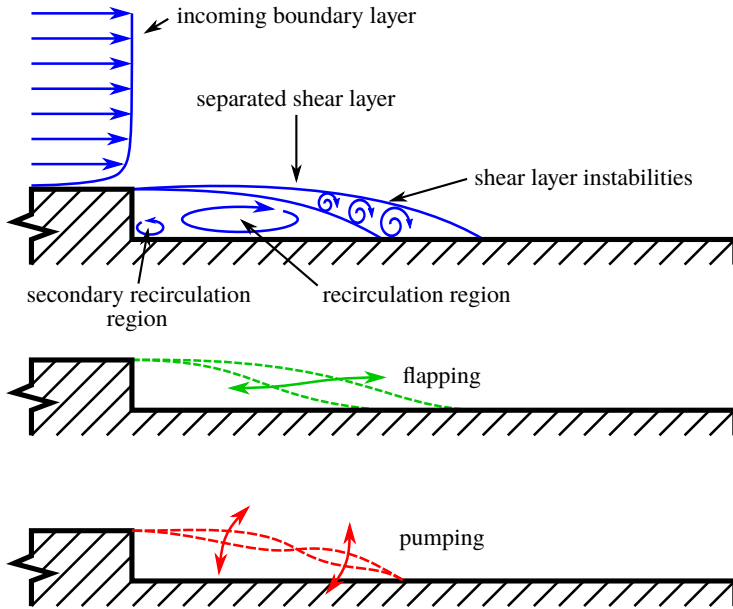


Figure 5.1: Separated flow phenomena occurring on a BFS

Figure 5.2 illustrates the three-dimensional behavior of the flapping and the pumping modes, which were termed as the cross-flapping and cross-pumping modes, respectively, by Statnikov et al. (2016a), as mentioned above.

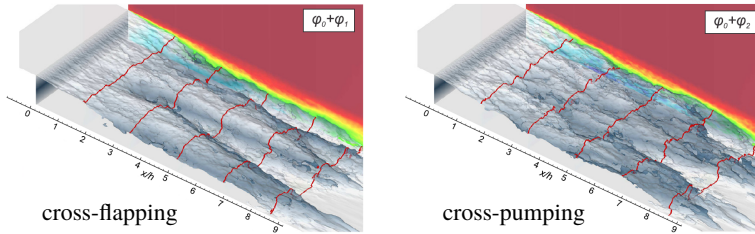


Figure 5.2: Three-dimensional behavior of the flapping mode (left) and the pumping mode (right). These results from a large-eddy simulation (LES) are published in Statnikov, Bolgar, Scharnowski, Meinke, Kähler, & Schröder (2016a)².

Previously, the existence of streamwise large-scale periodic coherent structures with a length of multiple step heights and a wavelength of roughly two step heights had been shown by Scharnowski, Bolgar, & Kähler (2015) and Scharnowski, Bolgar, & Kähler (2017). These structures form shortly aft of the step and strongly resemble the shape of the low-frequency cross-flapping mode as seen in Statnikov, Bolgar, Scharnowski, Meinke, Kähler, & Schröder (2016a). One should also not mistake these large-scale coherent structures for time-averaged streamwise vortices that have been shown to appear subsonic conditions by Barkley et al. (2002), Beaudoin et al. (2004), and supersonic conditions by Ginoux (1971). The streamwise vortical structures as described by Scharnowski et al. appear consistently over time, however randomly in space. When the velocity fields are time-averaged, there are no structures or streamwise vortices of any kind present, but the flow field is completely two-dimensional apart from side wall effects. An illustration of the theoretical formation process of these finger-like structures is provided in figure 5.3.

Despite all the available literature, very little work has been published on planar BFS in transonic flow. Even on axisymmetric BFS, also referred to as step on a body of revolution (SR), only a few publications are to be found. The following gives a brief overview on relevant material. The work of Kumar & Viswanath (2002) describes the pressure distribution aft of a SR with different boat-tail angles for the step. Depres et al. (2004) studied the effect of different rear body extension lengths on the unsteadiness

²Reproduced from Vladimir Statnikov, Istvan Bolgar, Sven Scharnowski, Matthias Meinke, Christian J. Kähler and Wolfgang Schröder. Analysis of characteristic wake flow modes on a generic transonic backward-facing step configuration. *European Journal of Mechanics – B/Fluids* 2016; 59: 124–134. © 2016 Elsevier Masson SAS. All rights reserved.

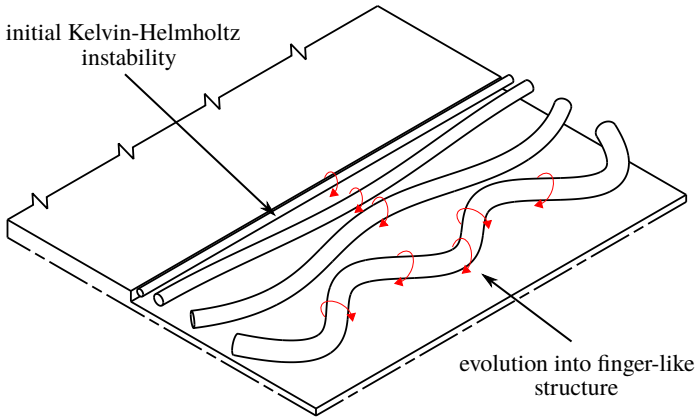


Figure 5.3: Theoretical formation process of the finger-like structures aft of a BFS found by [Scharnowski, Bolgar, & Kähler \(2017\)](#). Note that the figure only serves as an illustration and is not drawn to scale.

in transonic afterbody flows. [Deck & Thorigny \(2007\)](#) investigated the unsteadiness of transonic separating-reattaching flows on SR. [Schrijer et al. \(2014\)](#) conducted a modal analysis of unsteady fluctuations aft of a SR.

Recently, the work of [Statnikov et al. \(2015, 2016a\)](#), and [Scharnowski et al. \(2017\)](#) focused on transonic BFS flow. However, from the available literature it can be seen that it is still unclear what changes occur within the flow physics when going from the sub- to the trans- and supersonic conditions, an important criterion for a space launcher. Hence, a major research aim of this chapter is to analyze the wake topology and its characteristics throughout these Mach regimes. Furthermore, the question arises what mechanisms cause the most dominant pressure loads on the reattachment surface. Previous research on supersonic BFS has shown that this flow is characterized by a much shorter reattachment for both, the planar as well as the axisymmetric cases (refer to [Halupovich et al. \(1999\)](#), [Roshko & Thomke \(1966\)](#)), than in the sub- or transonic regimes. Therefore, it is evident that when moving from the below sonic into the supersonic regime, a large change in the flow physics is taking place, which is part of the research focus of this chapter.

5.2 Experimental setup

5.2.1 Test cases & BFS model

Free-stream Mach numbers ranging from 0.30 up to 2.70 were examined over a BFS model. Table 5.1 provides the experimental conditions that were analyzed with PIV, dynamic pressure sensors, and simultaneous PIV-pressure measurements. The \pm values in the table indicate the standard deviation of each quantity during the measurements.

Table 5.1: Free-stream flow conditions of TWM with the standard deviations of the quantities

Exp. method	Ma_∞	p_0 [bar]	p_∞ [bar]	T_0 [K]
PIV	0.30 ± 0.0015	1.20 ± 0.0013	1.131 ± 0.0012	294 ± 1.8
	0.50 ± 0.0013	1.20 ± 0.0019	1.012 ± 0.0015	292 ± 1.6
	0.80 ± 0.0008	1.73 ± 0.0017	1.129 ± 0.0012	291 ± 1.2
	0.90 ± 0.0006	1.60 ± 0.0016	0.943 ± 0.0009	290 ± 1.0
	2.00 ± 0.0010	2.20 ± 0.0023	0.282 ± 0.0004	292 ± 1.6
pressure measurements	0.30 ± 0.0013	1.20 ± 0.0016	1.130 ± 0.0015	289 ± 1.0
	0.40 ± 0.0012	1.20 ± 0.0012	1.076 ± 0.0011	287 ± 0.9
	0.50 ± 0.0010	1.20 ± 0.0009	1.007 ± 0.0007	287 ± 0.9
	0.60 ± 0.0007	1.20 ± 0.0007	0.940 ± 0.0006	286 ± 0.8
	0.70 ± 0.0006	1.20 ± 0.0010	0.863 ± 0.0009	286 ± 0.8
	0.80 ± 0.0007	1.72 ± 0.0014	1.128 ± 0.0005	284 ± 0.6
	0.90 ± 0.0006	1.60 ± 0.0010	0.946 ± 0.0007	285 ± 0.7
	2.00 ± 0.0013	2.20 ± 0.0017	0.284 ± 0.0005	285 ± 0.7
	2.70 ± 0.0018	5.00 ± 0.0014	0.223 ± 0.0006	287 ± 1.3
simultaneous PIV-pressure	0.80 ± 0.0007	1.73 ± 0.0013	1.129 ± 0.0010	285 ± 1.0
	2.00 ± 0.0012	2.20 ± 0.0014	0.283 ± 0.0005	286 ± 1.3
schlieren	0.80 ± 0.0007	1.73 ± 0.0015	1.129 ± 0.0007	285 ± 0.7
	0.90 ± 0.0007	1.60 ± 0.0012	0.942 ± 0.0007	287 ± 0.7
	2.00 ± 0.0009	2.20 ± 0.0015	0.283 ± 0.0006	286 ± 0.7

Figure 5.4 shows essential details of the BFS model, as well as the PIV FOV and schlieren measurement volume used for the investigations. For more details about the model, the reader is referred to chapter 4.1.

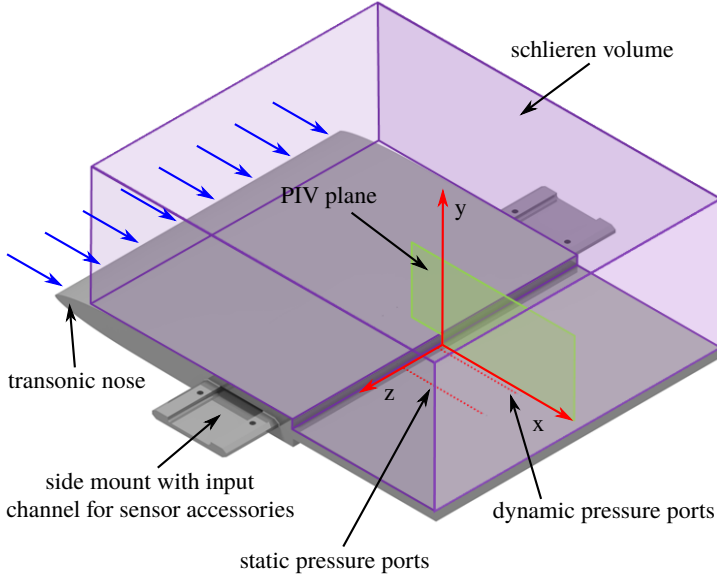


Figure 5.4: Illustration of the planar space launcher model with its pressure ports and the field of view under investigation

5.2.2 Particle image velocimetry

The PIV setup described in chapter 4.2.2 was used for the two-dimensional velocity field measurements. For each test case, 1000 double images were recorded. The time separation between an image pair was set in between $0.8 - 4.5 \mu\text{s}$, depending on the free-stream Mach number being evaluated. For data processing, the same pre-processing, evaluation methods, and post-processing steps were applied as described in chapter 4.2.2. During the PIV evaluation the final interrogation window size was reduced to 12×12 pixel with 50 percent overlap, yielding a vector grid spacing of $210 \mu\text{m}$.

5.2.3 Dynamic pressure measurements

In addition to the PIV measurements, dynamic pressure measurements were also conducted. These measurements were not only carried out at the same Mach numbers as PIV, but also at various other Mach numbers for a more complete overview (refer to table 5.1). The 24 dynamic sensors (Kulite XCQ-062 with a gauge pressure range of ± 3.5 bar) were sampled simultaneously at a frequency of 25.6 kHz, gathering 128,000 samples in 5 s for each Mach number, while static pressure ports were sampled with 200 Hz. A physical reference pressure from the free-stream at $x/h \approx -30$ was applied onto the static and dynamics pressure sensors, in order for them to measure the difference to the static pressure in the test section's free-stream. The dynamic pressure transducers were calibrated simultaneously by applying various relative pressures within the range of ± 0.8 bar onto the backside of the membranes via reference tubes with a General Electric PACE 5000 pressure controller. The voltage at each pressure point was measured, ultimately resulting in a calibration curve for each sensor. After calibration, the unfiltered mean values of the dynamic sensors were compared to the static values and showed a near perfect match (refer to figure 5.5). Thus, the results summarized in chapter 5.3.3 only show the pressure values gathered with the dynamic sensors. Figure 5.5 also shows the standard deviations of the pressure values measured with the static and the dynamic sensors. As expected, the static sensors underestimate the dynamics significantly, since the viscous effects in the long pressure lines dampen their signals. Note that the dynamic pressure sensors at $x/h = 3.5, 6.5$ & 10 were not used for the measurements, since some of the 24 available electrical ports were used to also measure pressure fluctuations in the free-stream and ahead of the step simultaneously.

5.2.4 Simultaneous PIV-pressure measurements

For the scope of this chapter, PIV and dynamic pressure were measured simultaneously for a trans- ($Ma_\infty = 0.80$) and a supersonic case ($Ma_\infty = 2.00$). This was done in order to compare a flow with transonic behavior aft of the step (without supersonic expansion around the BFS) to a flow with supersonic behavior aft of the step (with supersonic expansion around the BFS). At both of the free-stream Mach numbers, 500 PIV images were recorded at 15 Hz while recording the dynamic pressure data at 25.6 kHz, gathering just above 850,000 pressure samples at each port. By measuring PIV simultaneously to the pressure at various locations, it is possible to correlate the velocity fluctuations to the pressure fluctuations in similar manner as in the works of Hudy et al. (2007), Buchmann et al. (2016), Bolgar et al. (2017), Chovet et al. (2017). This technique makes it possible to visualize the fluid structures that cause the dominant pressure loads on the surface in a spatially highly resolved velocity plane. The triggering event of the PIV system and the pressure sensors was set up to work simultaneously, so that each vector field can be assigned to a certain pressure sample at each sensor. When the 500 corresponding pressure signals are correlated to their 500 velocity fields, the pressure fluctuations at one pressure port were correlated to a

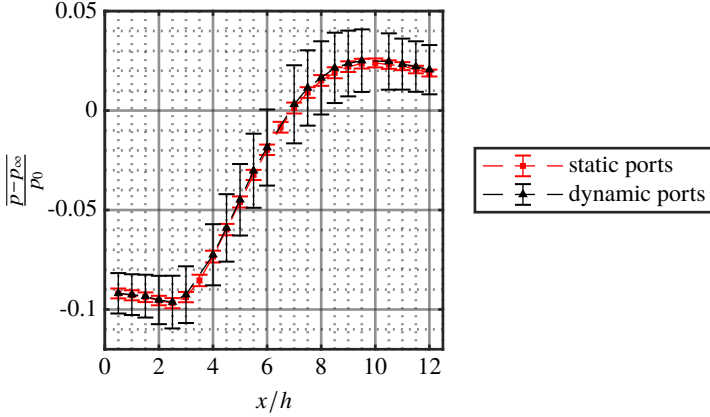


Figure 5.5: Comparison of the mean total pressure coefficients measured with static pressure probes vs. dynamic pressure transducers at $Ma_{\infty} = 0.80$. The error bars indicate the standard deviations of the pressure values.

component of the velocity fluctuations in the 2D velocity plane, as described by Pearson's correlation coefficient (refer to [Rodgers & Nicewander \(1988\)](#)) in equation 5.2.

$$R_{pu}(x, y) = \frac{\sum_{i=1}^N [p_i(x_0) - \bar{p}(x_0)][u_i(x, y) - \bar{u}(x, y)]}{\sqrt{\sum_{i=1}^N [p_i(x_0) - \bar{p}(x_0)]^2 \sum_{i=1}^N [u_i(x, y) - \bar{u}(x, y)]^2}} \quad (5.2)$$

where the term $[p_i(x_0) - \bar{p}(x_0)]$ is the fluctuating portion of the pressure (or p') evaluated at a streamwise location x_0 , while the term $[u_i(x, y) - \bar{u}(x, y)]$ is the fluctuating portion of a scalar of the velocity vector (or u' or v' in the scope of this dissertation) evaluated in the entire 2D plane of the FOV. A pressure sample is evaluated with its corresponding image i up to the sum of all the images N .

The temporal resolution of PIV can be improved artificially with the use of pressure transducers. For this, the pressure signals are shifted by Δt and correlated to the vector fields. This means that a set of pressure signals recorded before or after the double images were taken indicates the past or the future, respectively, in relation to those images. This allows for a statistical tracking of dominant phenomena over time with the temporal resolution of the dynamic pressure sensors, thus an artificially improved temporal resolution. Each correlation image shows the correlation between the 500 velocity fields to 500 pressure measurements with an offset of Δt . This is described by equation 5.3.

$$R_{pu}(x, y, t) = \frac{\sum_{i=1}^N [p(x_0, t_i - \Delta t) - \bar{p}(x_0)][u_i(x, y) - \bar{u}(x, y)]}{\sqrt{\sum_{i=1}^N [p(x_0, t_i - \Delta t) - \bar{p}(x_0)]^2 \sum_{i=1}^N [u_i(x, y) - \bar{u}(x, y)]^2}} \quad (5.3)$$

where $(t_i - \Delta t)$ indicates that not only the PIV images' corresponding pressure terms p' recorded at t_i can be correlated to the PIV images, but also pressure fluctuating terms offset by a certain time step Δt .

5.3 BFS results & discussion

5.3.1 Mean flow field & reattachment

The mean flow fields in figure 5.6 clearly show that with increasing Mach numbers the reattachment location moves downstream, at least up to $Ma_\infty = 0.80$. This is in contradiction to the mean pressure coefficients, which show that the maximum suction aft of the step remains at comparable values with increasing Mach number (refer to figure 5.7). This means that the mean reattachment location moves downstream with increasing Mach number due to the increase in inertial forces and momentum of the flow. As soon as the flow is locally above sonic conditions ahead of the step (from $Ma_\infty = 0.90$), a supersonic expansion occurs around the step, forcing the reattachment location to move upstream again. With a further increase in Mach number, the expansion angle around the step gets steeper, therefore further decreasing the reattachment length. The overall large deviation in the reattachment length for varying Mach numbers is characteristic of the planar BFS, while being present in a weaker manner on axisymmetric BFS. Due to the radial degree of freedom provided by an axisymmetric shape, mean reattachment occurs further upstream in general. Above sonic conditions, either configuration's mean reattachment length is controlled by the Prandtl-Meyer expansion around the step, which is purely a function of the Mach number. The trend either configuration shows at various Mach numbers is comparable, as well as the three-dimensional large-scale structures, and the shear layer instability or growth rate mentioned in chapter 4.1. Figure 5.8 compares the reattachments from the experiments of this chapter with other experimental reattachment locations on axisymmetric BFS published in literature. The mean reattachment locations were determined by taking the first reliable vector above the surface, whose x -component was positive. Since the mean reattachment locations were determined using standard PIV (refer to chapter 5.2.2) and not single-pixel ensemble correlation, the first reliable vector above the surface is at $y/h = 0.028$ or $200 \mu\text{m}$.

The topology of the subsonic flow fields are rather similar, as can be seen from figure 5.6. It can also be noticed that the maximum of the mean horizontal component of the back-flow velocities are around -20% of the free-stream velocity, regardless of the Mach number. The maximum values of the mean horizontal component of the velocities are around 110% of

the free-stream, until $Ma_\infty = 0.90$, where a supersonic expansion is already present around the step. The mean reattachment as well as the extreme values of both mean velocity components are summarized in table 5.2.

Table 5.2: Mean flow field statistics and extrema from PIV

Ma_∞	x_r/h	\bar{u}_{\max}/U_∞	\bar{u}_{\min}/U_∞	\bar{v}_{\max}/U_∞	\bar{v}_{\min}/U_∞
0.30	4.4	1.07	-0.21	0.05	-0.13
0.50	4.8	1.08	-0.21	0.04	-0.12
0.80	6.0	1.13	-0.22	0.05	-0.10
0.90	5.1	1.32	-0.24	0.31	-0.13
2.00	3.2	1.07	-0.18	0.16	-0.24

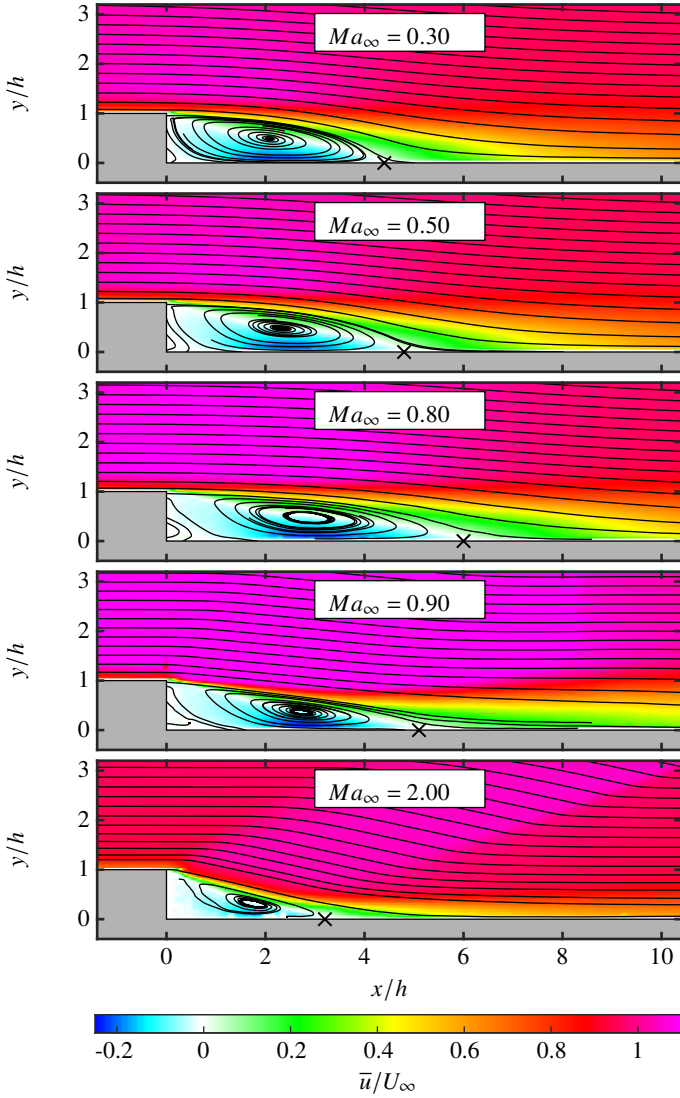


Figure 5.6: Streamwise component of the mean flow fields at various Mach numbers

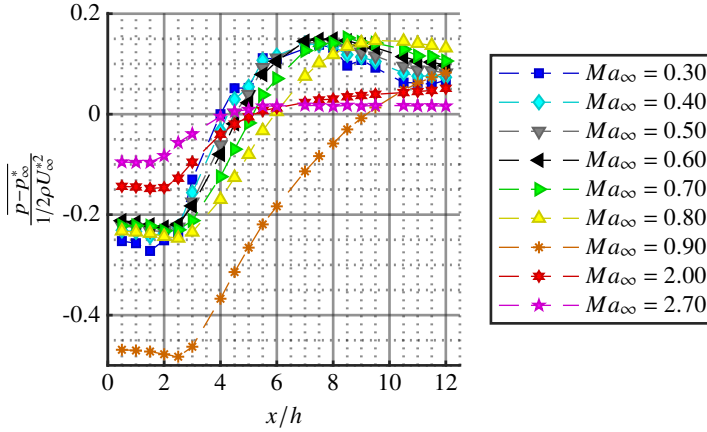


Figure 5.7: Mean pressure coefficients at various Mach numbers. The pressure p_∞^* and the velocity U_∞^* indicate the far-field quantities at $x/h \approx -2.5$ and $x/h \approx -58.5$ for the sub- and supersonic cases, respectively.

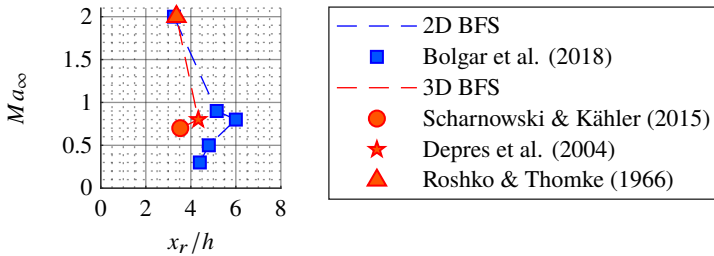


Figure 5.8: Free-stream Mach number vs. reattachment length for planar and axisymmetric BFS: $Ma_\infty = 0.7$ from [Scharnowski & Kähler \(2015\)](#), $Ma_\infty = 0.8$ from [Depres et al. \(2004\)](#), $Ma_\infty = 2$ from [Roshko & Thomke \(1966\)](#).

5.3.2 Dynamic flow field statistics

Looking at the back-flow ratios in close proximity of the reattachment surface at various free-stream Mach numbers gives an idea of the spatio-temporal flow behavior (refer to figure 5.9). The figure shows the number of back-flow events normalized with the total number of measurements extracted from instantaneous PIV vector fields at a height of $y/h = 0.1$, as a function of the streamwise location. In the secondary recirculation region, only little back-flow exists for either of the free-stream Mach numbers. The back-flow ratios increase to above 90 % for all Mach numbers, reaching around 95 % for $Ma_\infty = 0.80$ at $x/h = 2.65$. A back-flow ratio of 50 % is reached just slightly ahead of the mean reattachment location, since it was determined just above the surface. This shows that around the reattachment location the flow has approximately the same amount of forward as reverse flow events. As the back-flow ratio shows the temporal behavior at the horizontal locations, the negative slope of the ratio indicates the steadiness of the flow. A highly negative slope after the maximum back-flow location means that reverse flow events quickly fade away with increasing distance aft of the step. Therefore, the case with the steadiest reattachment dynamics is the $Ma_\infty = 2.00$ case, because it has the largest negative slope near reattachment. Its maximum back-flow ratio peaks around 75 %, whereas all other free-stream Mach numbers' back-flow maxima are around 95 %. $Ma_\infty = 0.90$ shows the least negative slope around reattachment, or most changes to the velocity directions at the respective streamwise locations. This behavior at a height of $y/h = 0.1$ reflects the results of the Reynolds shear stresses shown in figure 5.10, where at $Ma_\infty = 0.90$ the Reynolds shear stresses are relatively high close to the surface, when compared to the other free-stream Mach numbers. Thus, at this height above the surface the velocity fluctuations and the number of reverse flow vector counts are very high, likely caused by the interaction of the recompression shock aft of reattachment with the shear layer.

At $Ma_\infty = 0.80$ the portion from $x/h = 2.5 - 5$ is also less negative than the rest of the subsonic free-stream Mach numbers. Hence, the recirculation region shows a more unstable behavior in the transonic regime than in subsonic conditions. This is most likely due to the stronger presence of the flapping mode in transonic conditions (refer to chapter 5.3.3), causing a higher amount of momentum exchange with the flow outside of the shear layer.

The Reynolds shear stresses in figure 5.10 show the averaged velocity fluctuations taking place in the 2D flow fields, indicating the presence of turbulent vortical structures. From $Ma_\infty = 0.30 - 0.80$ the maxima of the absolute normalized intensities of the shear fluctuations are similar, reaching around 2.5 % of the square of the free-stream velocity. This is in good agreement with the results of Scharnowski (2013), who compared the Reynolds shear stress distribution aft of a BFS at $Ma_\infty = 0.70$ with different PIV evaluation methods. In the current results, when looking at the contour lines of constant intensity, one can notice how the area of the higher intensity fluctuations increases with increasing Mach number (up to $Ma_\infty = 0.80$), indicating a larger spread of vortices aft of the BFS. The

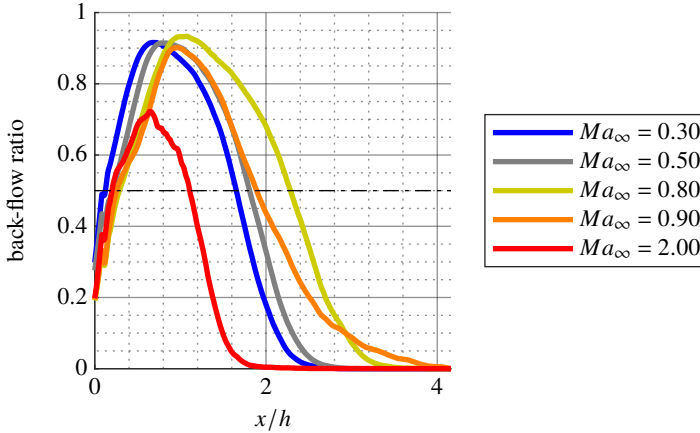


Figure 5.9: Back-flow ratio for various Mach numbers at $y/h = 0.1$

intensity and spread majorly increases at $Ma_\infty = 0.90$, where the maximum of the absolute mean intensity reaches 3.8% of the square of the free-stream velocity. These values should be viewed with caution though, as the values are normalized to the free-stream velocity, which is lower than the velocity right ahead of the step. Regardless, the high intensities just outside of the recirculation region indicate that the formation of the lambda shock is strongly interacting with the shear layer, thereby causing large changes in velocity. In supersonic conditions at $Ma_\infty = 2.00$ the Reynolds shear stresses already decrease substantially in their normalized magnitude as well as their spreading. It becomes clear that the major velocity fluctuations occur in close proximity of the reattachment surface. This is due to the fact that the region in between the supersonic expansion about the step and the oblique shock fan forming close to the reattachment location is very stable. This can be explained by the fact that both, the supersonic expansion and the oblique shock occur at defined angles, which are a function of the Mach number and the deflection angles imposed by the geometry. This is also the reason why the oblique shock seen in figure 4.5 is stable in time.

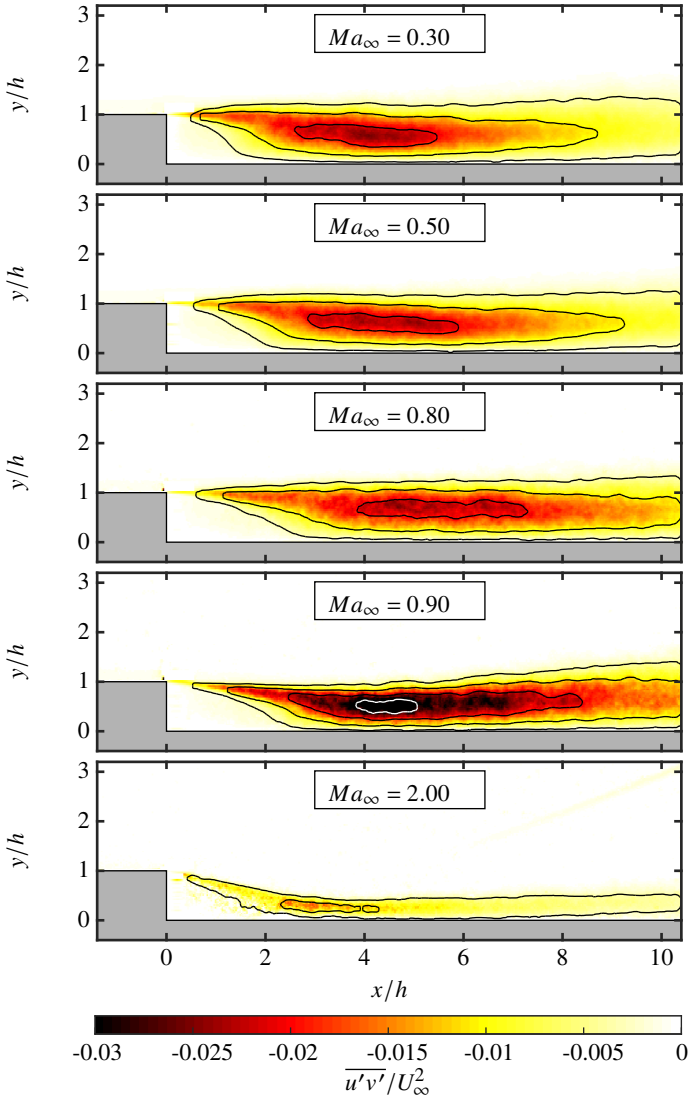


Figure 5.10: Reynolds shear stress distribution at various Mach numbers. Contour lines indicate $\overline{u'v'}/U_\infty^2 = -0.003, -0.01, -0.02, -0.03$ towards the center.

Figure 5.11 shows a line plot of the normalized Reynolds stresses at the reattachment locations of the various Mach numbers. From $Ma_\infty = 0.30 - 0.80$ it can be seen that the maxima of the absolute magnitudes decrease slightly while also moving further away from the reattachment surface, caused by the broadening of the shear layer. The highest stress magnitudes (normalized by the defined free-stream velocity ahead of the model) are experienced at $Ma_\infty = 0.90$. At this point the location of the maximum stresses start moving back towards the reattachment surface. At $Ma_\infty = 2.00$ the maximum absolute magnitude of the Reynolds stresses moves even closer to the reattachment surface, as the shear layer becomes thinner. The maximum of the normalized magnitudes also strongly decreases, indicating a steadier flow field. The normalized intensities of the Reynolds stresses however, do not give an indication of the trend of the normalized pressure fluctuations on the surface (refer to chapter 5.3.3) when comparing the various free-stream Mach numbers.

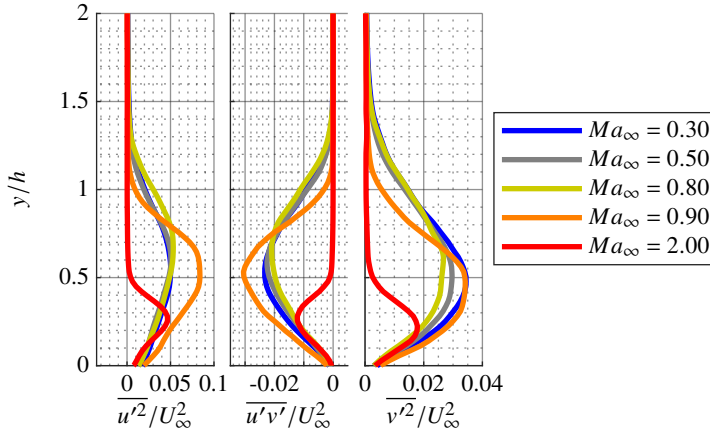


Figure 5.11: Reynolds stress profiles at x_r for various Mach numbers

5.3.3 Dynamic pressure measurements

Mean pressures and RMS fluctuations on the reattachment surface

For comparison reasons, the reference pressure for the processing of the dynamic pressure measurements was adjusted to be just in front of the step at $x/h \approx -2.5$ (up to $Ma_\infty = 0.90$) in order to compensate for the blockage effects present at during transonic flow (refer to figure 4.4 in section 4.2.5 for more details). The supersonic cases were referenced with a pressure port in front of the bow shock stemming off the model's nose. This port is located at $x/h \approx -58.5$. The pressure data in this section was normalized by the total pressure instead of the dynamic pressure q_∞ (refer to table 5.1). This allows for a direct comparison of the normalized pressure data at different Mach numbers, which is impossible when normalizing with q_∞ , due to the large increase in the dynamic pressure with increasing Mach number. For simplicity, this quantity will be referred to as the total pressure coefficient C_{p0} .

Similar to the pressure coefficient in figure 5.7, the total pressure coefficient starts converging to a value of zero towards the end of the reattachment surface (refer to figure 5.12 at the top). Due to the normalization, the mean total pressure coefficient exhibits a more pronounced rise in the suction as well as in its pressure recovery with increasing Mach number below sonic conditions, than the classically defined pressure coefficient shown in figure 5.7. The supersonic cases show the weakest expansion and recoveries.

The RMS pressure fluctuations provide a good overview of the dynamic loads that occur on the reattachment surface. In figure 5.12 at the bottom, it can be seen that the average pressure fluctuations start to increase slowly with increasing Mach number from $Ma_\infty = 0.30 - 0.50$. At $Ma_\infty = 0.60$ the average pressure fluctuations increase drastically, while from $Ma_\infty = 0.70$ the high-pressure fluctuations start to spread out, reaching the maximum overall intensities of approximately 2.1% of the total pressure. At $Ma_\infty = 0.80$ the intensities slightly decrease, while from $Ma_\infty = 0.90 - 2.70$ the average pressure fluctuations drastically decrease with increasing Mach number. The maximum of the average pressure fluctuations occurs at approximately reattachment from $Ma_\infty = 0.30 - 0.50$. At $Ma_\infty = 0.80$ however, the maximum average pressure fluctuations move downstream to $x/h = 7$, whereas the reattachment occurs at $x/h = 6$. Overall it can be concluded that the reattachment surface experiences the highest mean loads in the transonic regime. One should also note that the bending moment of the average loads is loosely coupled to the mean reattachment location, an important criterion in some engineering applications such as a space launcher. Thus, the most extreme bending moment dynamics also occur in the transonic regime.

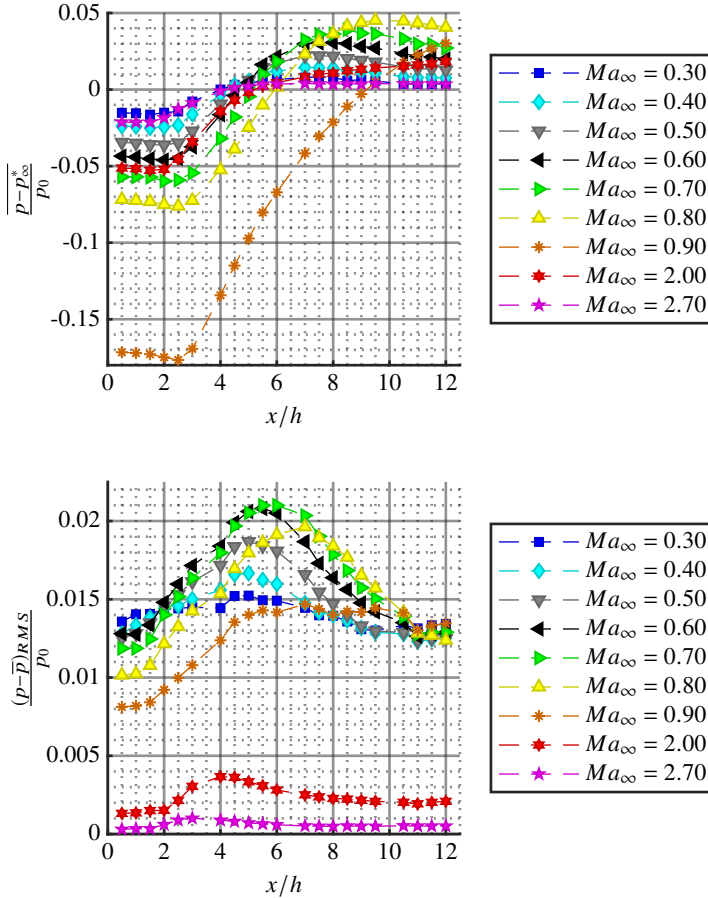


Figure 5.12: Mean (top) and RMS (bottom) total pressure coefficients at various Mach numbers. The pressure p_∞^* indicates the far-field pressure at $x/h \approx -2.5$ and $x/h \approx 58.5$ for the sub- and supersonic cases, respectively.

Pressure fluctuations in space and time

The behavior of the pressure fluctuations in space and time is shown in figure 5.13 for $Ma_\infty = 0.80$ and $Ma_\infty = 2.00$. In this figure 200 pressure samples are illustrated over a time period of approximately 8ms for each sensor. For the transonic case, coherent structures moving downstream can be tracked as diagonal patches, shown in either blue or red, moving towards the right top of the image. As the diagonal lines appear relatively often, the structures are occurring at quite a high and consistent frequency. In contrast, the supersonic case has less coherence, while the footprints of the pressure fluctuations are thicker and more widespread. Thus it seems that coherent eddies are not the cause of the load fluctuations on the surface in the supersonic regime, but rather a different mechanism of the subsonic layer close to the surface. This will be further elaborated on in chapter 5.3.4 and 5.3.4.

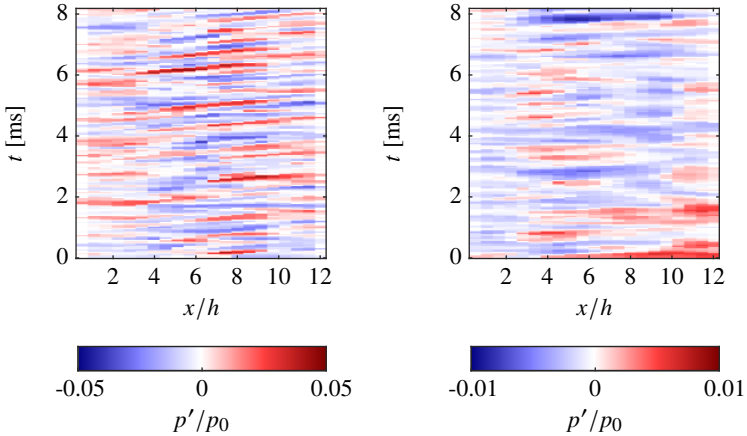


Figure 5.13: Normalized pressure fluctuations at $Ma_\infty = 0.80$ (left) and $Ma_\infty = 2.00$ (right) in space and time

Pressure spectra

In this section, the spatial spectra, or spectrograms, of the surface pressure fluctuations of various free-stream Mach numbers are compared amongst one another. For the ease of interpretation of the spectrograms, figure 5.14 provides an overview of a pressure spectrogram at $Ma_\infty = 0.60$ with a local 2D spectrum extracted at $x/h = 6$. The spectrogram visualizes the evolution of the power spectral density (PSD) of the pressure fluctuations over the length

of the reattachment surface from $x/h = 0.5 - 12$ on the horizontal axis. The PSD is given in units per kHz, since the pressure fluctuations were normalized by the total pressure for each measurement. Its value is indicated by the intensity of the color. The frequencies are provided on the left vertical axis. Additionally, the Strouhal number with respect to the step height is provided on the right vertical axis. The highlighted patches in the spectrograms are the modes of the shear layer experienced by the reattachment surface. These modes will be elaborated on later in this section. The dominant peaks (shown in the dark colors at $f \approx 400\text{Hz}$, 1100Hz , 1700Hz) spanning horizontally across the spectrogram, are the wind tunnel background noise. This can be deduced by the fact that the frequencies stay constant with the streamwise location and are consistent with increasing free-stream Mach numbers (refer to figure 5.15).

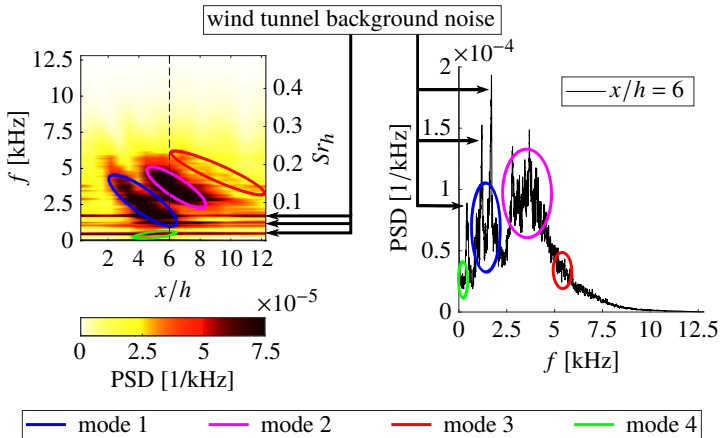


Figure 5.14: Illustration of the modes of the surface pressure fluctuations within a spectrogram (on the left) and its according 2D spectrum extracted at $x/h = 6$ (on the right) at $Ma_\infty = 0.60$

The spectrograms provided in figure 5.15 compare the evolution of the PSD of the pressure fluctuations at various free-stream Mach numbers. A plot for $Ma_\infty = 0.3$ is not provided due to the sensor sensitivity at low pressure fluctuations (refer to sensor pressure range in chapter 5.2.3).

The oval patches in figure 5.15 are the frequencies caused by the separated flow. The dominant peaks in the spectrum increase in their frequency range (at approximately constant Strouhal number Sr_{L_t}) as well as in their normalized intensities from $Ma_\infty = 0.40 - 0.70$. This is consistent with the findings of the mean pressure fluctuations, as they also reach their maximum at $Ma_\infty = 0.70$. From $Ma_\infty = 0.90$ the normalized intensities strongly

decrease and other patches start to appear.

Below sonic conditions, it can be said that there are various broadband patches or modes in the spectra, each being independent from one another. Each mode's frequency decreases while moving downstream. A decrease in frequencies of the spectra with increasing downstream distance was indicated by the findings of Eaton & Johnston (1980) as well, however the cause of the phenomenon was not certain back then. From $Ma_\infty = 0.4 - 0.6$ there are three clearly visible modes, each one being dominant at a different streamwise segment (modes 1,2 & 3 in figure 5.14). From $Ma_\infty = 0.70 - 0.80$ however, the two rearwards modes merge together. Additionally, a fourth distinct mode can be seen lightly around $x/h = 4 - 6$ below 1000Hz from $Ma_\infty = 0.60 - 0.80$ (mode 4 in figure 5.14).

The two major modes (modes 1 and 2) overlap right around the reattachment location, or the location of the highest mean pressure fluctuations. Mode 1 acts upon the recirculation region and exhibits Strouhal numbers ($Sr_h \approx 0.07$ at the patch's center at $Ma_\infty = 0.80$ for example) typical for the cross-pumping mode of the shear layer, as described by Statnikov et al. (2016a). The overall dimensionless frequencies of these modes are evidently decreasing with increasing free-stream Mach numbers and can be found between Strouhal numbers of $Sr_{L_r} \approx 0.4 - 0.6$, similar to previous findings (Eaton & Johnston 1981, Le et al. 1997, Statnikov et al. 2016a). Thus, this mode can be characterized as the pumping, or the more recently discovered cross-pumping mode. This mode's dimensionless frequency with respect to the model thickness is $Sr_t \approx 0.23$ at the patch's center at $Ma_\infty = 0.80$. According to Marie et al. (2011), the natural frequency of the structural pendulum mode of the Vulcain 2 nozzle is around $Sr_D = 0.2$ with respect to the Ariane 5's main stage diameter. Thus, the aerodynamic cross-pumping mode is very likely the mode which excites the structural pendulum mode of Ariane 5's nozzle at transonic flight conditions.

Mode 2, having a Strouhal number of $Sr_{L_r} \approx 0.7$ at the centers of its patches, can be characterized as the step mode as defined by Hasan (1992). This mode's normalized frequency range falls right into the scope of values found in literature, ranging from $Sr_{L_r} = 0.6 - 1.0$ (Cherry et al. 1984, Driver et al. 1987, Hasan 1992, Heenan & Morrison 1998). The large spread in those results can now be explained by the fact that the dominant frequency of this mode decreases while moving downstream. This makes the dominant frequency of a PSD measured with one sensor very sensitive to its streamwise location. At $Ma_\infty = 0.80$, this mode has a Strouhal number of $Sr_h \approx 0.13$ at the patch's center, or $Sr_D \approx 0.43$. The natural frequency of the structural ovalization mode of the Vulcain 2 nozzle was shown to be around $Sr_D = 0.5$ by Marie et al. (2011). Depending on the streamwise location of the step mode, its frequencies therefore align rather well with the frequencies which excite nozzle ovalization. Therefore, the aerodynamic step mode is most likely the source which excites the structural ovalization mode of Ariane 5's nozzle at transonic flight conditions. The step mode is dominated by Kelvin-Helmholtz vortices, which will be further verified in chapter 5.3.4.

The decrease in the frequencies with increasing distance away from the step can be explained by the fact that the smaller scale structures start to grow together in three-

dimensional space to form larger ones while moving downstream, which was also hypothesized by McGuinness1978 (1978). This hypothesis is supported by the fact that the two major modes both have a continuous trend and can clearly be separated into distinct phenomena. Opposing opinions that contradict this model also exist in literature, which suggest that an intermittent upstream motion of the large-eddy structure is responsible for the decrease in the frequencies (Bradshaw & Wong 1972, Hasan 1992). The intention of this theory is that the shear layer structures are split at reattachment, causing the eddies to alternately move up- and downstream, thereby decreasing the frequency of the mode downstream. According to Troutt et al. (1984) the pairing interactions are strongly inhibited in the reattachment region. When looking at the spectra around reattachment in this work, it becomes clear that the nature of the problem is more complex, as two different modes act upon that location. However, when following the step mode further downstream, the pairing of vortices is a very feasible explanation. The decrease in the frequencies noticed in previous literature when moving upstream is a different mode in reality.

The centers of the weaker mode 4 below 1000Hz between $x/h = 4 - 6$ from $Ma_\infty = 0.60 - 0.80$ are found at around $Sr_h \approx 0.01$, coinciding with the low-frequency cross-flapping mode described by Statnikov et al. (2016a). In contrast to the other modes, this mode's dominant frequency slightly increases with increasing distance away from the step. This is very likely due to the fact that the structures causing the cross-flapping motion are spatially concentrated closer to reattachment, rather than a breakdown process into the upstream direction.

Looking at the spectrogram at $Ma_\infty = 0.90$, it becomes clear that a large change in the flow physics is taking place when the flow is locally sonic ahead of the step. Suddenly, the intensity of modes 1 & 2 decreases drastically while moving further downstream. With a further increase in the free-stream Mach number to supersonic conditions, the two previously registered dominant modes do not show up on the surface pressure signatures anymore.

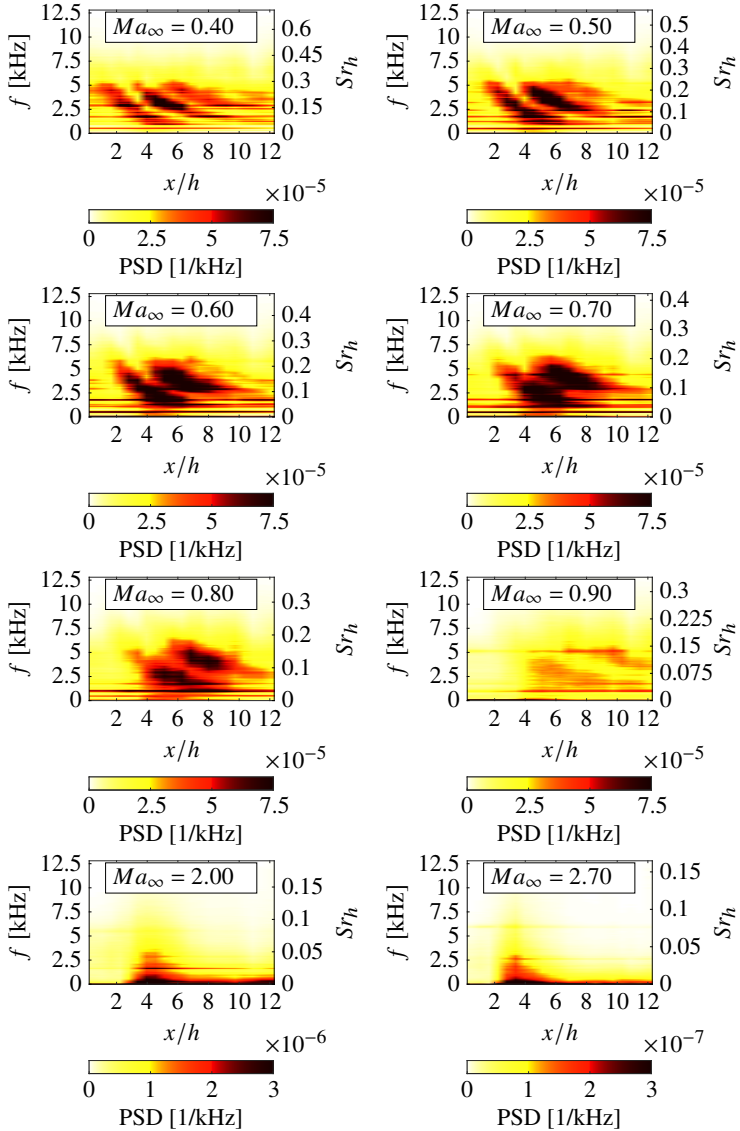


Figure 5.15: Streamwise evolution of the power spectral density of the surface pressure fluctuations at various free-stream Mach numbers

However, a broadband peak close to reattachment can be found above 1000Hz, as well as a widespread low-frequency patch below that. Figure 5.16 provides a more detailed illustration of these modes at $Ma_\infty = 2.00$. In that figure one can clearly see the higher frequency mode (mode 2s) being dominant around 3000Hz, or $Sr_h \approx 0.05$, just aft of the mean reattachment location at $x/h = 4$. Due to the peak's spatial location and its relatively broadband characteristic, this is assumed to be a mode induced by spatial fluctuations of the recompression shock. Below 1000Hz, or $Sr_h = 0.006$, the strong low-frequency band spans from just ahead of the reattachment location all the way to the end of the measurement domain for both, $Ma_\infty = 2.00$ & 2.70. This is highlighted as mode 1s in figure 5.16. Thus a low-frequency motion within the subsonic layer and the boundary layer of the reattached flow becomes the dominant mechanism for the dynamic loads on the surface in the supersonic regime. This will be elaborated on in chapter 5.3.4. This low-frequency mode is likely of the same nature as the low-frequency behavior found in other supersonic separated flows, which is probably caused by the dynamics of the separated bubble suggest by Kistler (1964), Dolling (2001), Pipponiau et al. (2009). It is important to point out that this phenomenon extends all along the length of the reattachment surface and is not confined to the recirculation zone. More importantly, the normalized intensities of these two modes are over an order of magnitude lower than of those at transonic free-stream velocities.

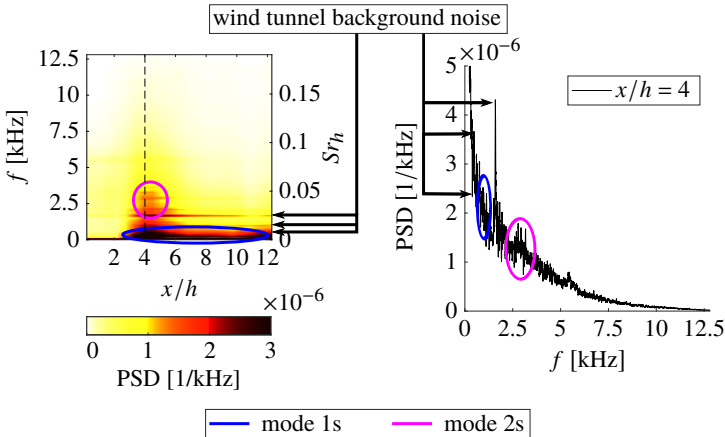


Figure 5.16: Left: Streamwise evolution of the PSD of the surface pressure fluctuations at $Ma_\infty = 2.00$ for the baseline case. Right: PSD extracted at $x/h = 4$ from the spectrogram in the left illustration.

5.3.4 Pressure-velocity correlations

Subsonic correlations

When comparing the intensities of the velocity fluctuations in figure 5.10 with the pressure fluctuations in figure 5.12 at the bottom at different wind tunnel conditions, the trend of their changes in magnitude with increasing Mach number do not correlate. The maximum normalized velocity fluctuations at reattachment for instance, occur at $Ma_\infty = 0.90$, showing high intensity fluctuations close to the surface. At that Mach number the pressure fluctuations are already quite low however. This indicates that the dynamic loads on the reattachment surface are not purely a function of the magnitude of the velocity fluctuations. In order to find a driving force for the dominant pressure loads on the reattachment surface, they were correlated with the velocity fluctuations in the 2D PIV plane.

When looking at the correlations at $Ma_\infty = 0.80$ in figure 5.17, it can be seen that the shape of the dominant flow structure causing the pressure fluctuations strongly resembles Kelvin-Helmholtz instabilities. This can especially be seen when correlating the y -component of the velocity fluctuations with the pressure fluctuations at $x/h = 7$, as seen on the right side of that figure. When there is a positive pressure fluctuation p' at a certain streamwise sensor, the red color in the figure spatially indicates that it is accompanied by a positive velocity fluctuation v' , while the blue color indicates a negative velocity fluctuation $-v'$. Through the orientation of the scalars, a circular motion across neighboring red and blue patches can be inferred. As they occur periodically in space, spanwise vortices, or Kelvin-Helmholtz instabilities, can be deduced from the correlations.

At $\Delta t = 0$ (left center image in figure 5.17) the correlation peak of R_{pu} , indicated by the red color, is right above the pressure transducer at $x/h = 7$. This type of correlation without a temporal shift is similar to the pressure velocity correlations carried out by Hudy et al. (2007), or the recently published work of Chovet et al. (2017). However, by having correlated the temporally offset pressure signals at $\Delta t = -117 \mu\text{s}$ and at $\Delta t = 117 \mu\text{s}$ (3 time steps before and after $\Delta t = 0$) to the PIV images, one can statistically track the most dominant structures in space and time, as shown in the work of Bolgar et al. (2017). This allows for the computation of the convection velocities, as well as the frequency of the most dominant phenomenon.

The most dominant frequency at $Ma_\infty = 0.80$ for instance, occurs around 4200Hz ($Str_h \approx 0.12$), according to the pressure-velocity correlations. This was also verified with the spectrum of the same sensor (located at $x/h = 7$), showing a broadband peak around the same frequency, which corresponds to the step mode. The cross-pumping mode found in the spectrogram (refer to figure 5.15) around 2400Hz ($Str_h \approx 0.07$) does not appear in the pressure-velocity correlations, meaning it does not have such a strong statistical impact on the load dynamics.

For the subsonic regime, it can be concluded that the Kelvin-Helmholtz vortices acting upon the reattachment surface in form of the step mode are the driving factor for the most

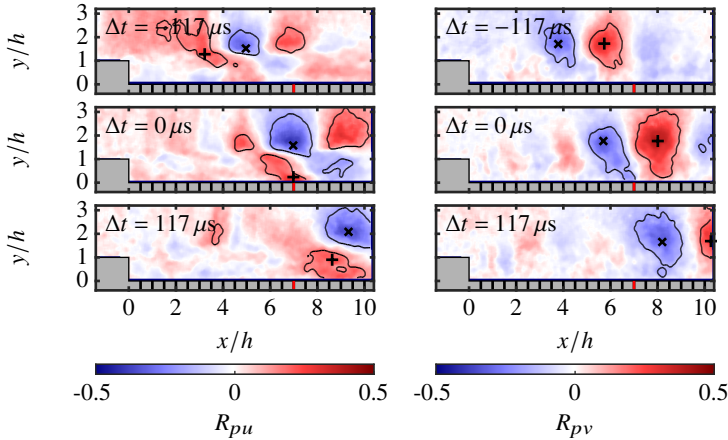


Figure 5.17: Correlation of pressure fluctuations at $x/h = 7$ to the scalars of the velocity field fluctuations at $Ma_\infty = 0.80$. Left column shows R_{pu} , right column shows R_{pv} . Images from top to bottom are offset by two time steps of the pressure transducers or $\Delta t = 117 \mu s$. The contour lines indicate a correlation of $R = \pm 0.15$.

dominant pressure fluctuations, which could also be deduced from figure 5.13. Even though they are three-dimensional in nature, statistically they clearly occur in a coherent way when displayed on a 2D plane. For the future it would be interesting to investigate a streamwise horizontal FOV, to see whether the structures correlate with the finger-like structures shown by [Scharnowski et al. \(2017\)](#). From these results, overall it can be stated that the step mode would be the main contributor towards buffeting by exciting the nozzle's ovalization mode (refer to section 5.3.3), when considering the example of Ariane 5.

Supersonic correlations

In contrast to the subsonic case, the dominant pressure fluctuations occurring on the reattachment surface do not come from Kelvin-Helmholtz vortices in the supersonic case. When looking at the pressure-velocity correlations in figure 5.18, the pressure fluctuations strongly correlate with the x -component of the velocity fluctuations of the entire shear layer, indicating a pumping motion for the most dominant mode. The y -component of the velocity fluctuations has an apparent anti-correlation in the expansion area behind the step, while the shock correlates well with the pressure fluctuations. This indicates that the motion of the shock is coupled to the pressure fluctuations. Overall, it is obvious that in the supersonic the coherent structures from the shear layer do not have an effect on the

pressure fluctuations close to the surface. It seems that the entire streamwise shear layer movement, or pumping, causes the most dominant pressure loads. It could be inferred that there is a distinct separation between the outer region, or the supersonic flow, with the recirculation region and the newly developing boundary layer, or the subsonic flow. In other words, it seems that the supersonic flow is decoupled from the subsonic region in terms of the effects reaching the surface in the form of pressure fluctuations. In the pressure-velocity correlations this is indicated by the clear distinction of the colors as well as the recompression shock terminating at the subsonic layer, assumed to be in red color (on the R_{pu} correlations in figure 5.18 on the left). This would indicate that the phenomena that act upon the outer regions do not protrude into the flow regions close to the surface, thus they do not have an effect on the wall pressure fluctuations. This could also be one of the reasons, why the normalized loads at $Ma_\infty = 2.00$ decrease by about an order of magnitude when comparing it to the loads at $Ma_\infty = 0.80$ (refer to the average pressure fluctuations in figure 5.12).

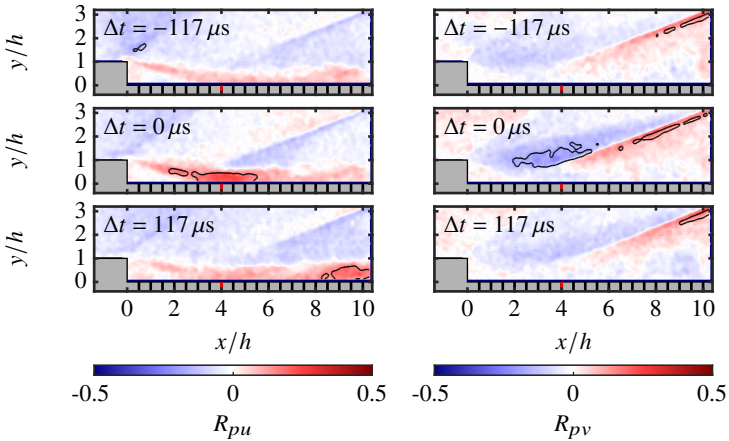


Figure 5.18: Correlation of pressure fluctuations at $x/h = 4$ to the scalars of the velocity field fluctuations at $Ma_\infty = 2.00$. Left column shows R_{pu} , right column shows R_{pv} . Images from top to bottom are offset by two time steps of the pressure transducers or $\Delta t = 117 \mu\text{s}$. The contour lines indicate a correlation of $R = \pm 0.15$.

The spectrum at $Ma_\infty = 2.00$ (refer to figure 5.15) shows a dominant peak around 1800Hz, which is a natural frequency of the TWM as stated previously. At approximately $x/h = 4$, a broadband peak extends from above 1000Hz to 4000Hz ($Sr_h = 0.015 - 0.06$). This peak does not appear in the pressure-velocity correlations, since the pumping motion

of the recirculation area occurs at substantially lower frequencies, as can be seen in the spectrogram between 50 – 400 Hz, depending on the streamwise location.

Overall, for the supersonic regime, it can be concluded that the driving mechanism for the load fluctuations on the reattachment surface are vastly different than below sonic conditions. This could also be seen in figure 5.13 through the tracking of the pressure fluctuations in space and time, where the mechanism for the supersonic case is vastly different from the transonic one. The most dominant flow motion resolved with the combined pressure-velocity correlations is a low-frequency pumping motion of the recirculation area. This is in good agreement with literature, where only low-frequency motions caused by the dynamics of the separated bubble have been identified thus far (Kistler 1964, Dolling 2001, Pignonau et al. 2009).

5.4 Summary & conclusions on the separated shear layer aft of a BFS

Experiments on a BFS in sub-, trans- and supersonic conditions have been carried out in order to determine the effects of the Mach number on the separated flow region, and to identify the main mechanisms responsible for the most dominant pressure loads experienced by the reattachment surface. Measurements were conducted with PIV, dynamic pressure transducers, and a combination thereof. It was shown that the intensities of the normalized pressure fluctuations do not correlate with the intensities of the normalized Reynolds shear stresses between the various Mach numbers. However, the location and distribution of the Reynolds shear stresses close to the surface give a good indication of the distribution of p'_{RMS} . The highest pressure dynamics occur in the transonic regime, explaining the difficulties and resulting failures of the Ariane 5 launcher. Furthermore, the mean reattachment location increases till sonic flow occurs ahead of the step. This poses an additional problem to a space launcher due to the longer moment arm about which the dynamic forces can act. After the transonic phase, the dynamic loads, as well as their moment arm drastically decrease with increasing Mach number throughout the supersonic regime.

Three modes acting on the reattachment surface in the form of pressure fluctuations could be identified for the transonic cases. The step mode, the cross-pumping mode, and the cross-flapping mode. In the supersonic regime, a low frequency pumping mode of the subsonic portion of the flow, as well as a shock oscillation mode are present at very weak intensities. It was shown that at $Ma_\infty = 0.80$, the aerodynamic cross-pumping and step mode would excite the structural pendulum and ovalization mode of the Vulcain 2 nozzle, respectively. This answers the first research question defined in chapter 2, which asks what major flow phenomena affect the nozzle structure of an Ariane-like launcher.

The second research question defined in chapter 2, asks if there is a major aerodynamic contributor to buffeting. This can be answered with the pressure-velocity correlations, which clearly show that the dominant pressure fluctuations in transonic conditions are caused by Kelvin-Helmholtz instabilities. The shape of these structures is already an

indicator that the step mode is the main contributor towards buffeting. This was verified by temporally offset correlations, which allowed for tracking these structures in space and time. This analysis method revealed that Kelvin-Helmholtz structures are convected at a dominant dimensionless frequency of $Str_h = 0.12$, which is the characteristic frequency of the step mode, clearly identifying the step mode as the major contributor towards buffeting.

In the supersonic regime however, a low-frequency pumping of the recirculation zone is the dominant motion. This indicates that the underlying physics governing flow separation and reattachment in sub- and supersonic flows are vastly different, and thus lead to distinct dynamics. The dynamic loads on the reattachment surface increase up to transonic conditions, however they drastically decrease once the flow aft of the BFS becomes locally supersonic. This could be an indication that the pressure fluctuations occurring aft of a BFS in supersonic flow are more comparable to that of supersonic boundary layer pressure fluctuations. This is supported by the fact that for instance p_{RMS}/q_∞ of 0.4 is nearly identical to that found in supersonic boundary layers at $Ma_\infty = 2.00$, shown by [Bernardini & Pirozzoli \(2011\)](#). The fact that the correlations clearly separate the area of the outer flow (assumed to be supersonic as explained in chapter 5.3.4) from the recirculation region and the newly developing boundary layer (assumed to be below sonic conditions) supports this hypothesis. This indicates that mainly the subsonic flow has an effect on the pressure loads on the surface. The fact that the supersonic flow above a boundary layer, for instance, does not protrude into the subsonic regions is also one of the challenges of getting particles for PIV into boundary layers at supersonic flow conditions. Similarly, the lack of mixing between sub- and supersonic regions do not mix, is one of the challenges in supersonic combustion.

It can be concluded that the transonic phase of the ascent is the most critical for the structural loads on the nozzle of a space launcher similar to Ariane 5. Defusing the step mode, as well as the cross-pumping mode, would be an important criterion for the design of structurally lighter nozzles. More importantly, if the severity of the step mode could be decreased, the use of longer nozzles with higher expansion ratios would become feasible again. This would ultimately increase the performance of a space launcher, which was the initial idea with the longer nozzle extension on Vulcain 2 prior to the failure on its first use on Ariane flight 517 (refer to chapter 2.2.2).

6 Load reduction with passive flow control

This chapter shows how passive flow control can decrease the static and dynamic loads aft of a BFS. Three different shapes of flow control devices were investigated, with a dimensional parameter study on two of those geometries. It is shown that the harmful step mode described in chapter 5 can be weakened efficiently by forcing streamwise vorticity onto the flow through the presence of the PFC geometry. The fact that the loads and the harmful modes can be reduced and weakened, respectively, makes it feasible to use longer nozzle extensions with higher expansion ratios, or even novel adaptive nozzle concepts. This would yield a performance increase for a space launcher, such as the Ariane 5, over the course of its trajectory. Thus, with an identical amount of propellant, higher orbits could be reached, or the gross takeoff weight could be increased. This chapter is structured as follows:

- 6.1 Literature review of flow control on BFS
- 6.2 Test cases and analysis methods
- 6.3 Detailed overview and discussion of the results
- 6.4 Summary and conclusions of the gathered insights

Part of this chapter is published in [Bolgar et al. \(2019b\)](#)¹.

6.1 Literature review of flow control on a BFS

In order to manipulate an unfavorable flow such as that aft of a BFS, technological approaches can be categorized into two distinct subsets; passive flow control (PFC) and active flow control (AFC). The main difference between the two methods is that AFC requires some sort of energy input for flow manipulation, while PFC manipulates the flow by adding a favorably shaped static body to the system ([Gad-el Hak et al. 2003](#)). Therefore, PFC offers a clear advantage by not requiring any external energy sources or additional accessories. On the other hand, a drawback of PFC is that it cannot be turned on when needed, or off when not required. However, for most applications PFC offers an economically as well as technologically efficient solution, as they are simple and more effective than AFC. Meanwhile, AFC is mainly advantageous when instabilities need to be triggered. On a backward-facing step, flow control is classically applied for the reduction

¹Reprinted by permission of the American Institute of Aeronautics and Astronautics, Inc.

of the mean reattachment length. For an applied case of a space launcher, this is a critical parameter, since a reduction in the mean reattachment length also decreases the length of the moment arm that the dynamic loads act upon. Next to reducing this quantity, the reduction of the dynamic pressure loads is another point of concern.

Flow control attempts have been made on the scaled down model of Ariane 5 at subsonic Mach numbers up to $Ma_\infty = 0.8$ (same model that was mentioned in the buffeting experiments in chapter 2), however with very limited success. Hannemann et al. (2011) and Schrijer et al. (2011) tried to reduce the buffeting loads on the nozzle by using passive skirt extensions, which basically elongated forebody of the launcher. The results showed that a decrease in the RMS pressure fluctuations in a very far downstream location is accompanied by an increase close to the base surface. An airfoil shaped guide vane on top of the forebody, referred to as scoop, was also tested. The use of the scoop resulted in a clear shortening of the mean reattachment length by routing the air towards the nozzle. Due to its extreme camber of approximately 90° , the scoop would inherently yield a large drag penalty.

On the simplified case of a BFS, various research on active flow control exists in literature. For example, Chun et al. (1999) experimented with local forcing just ahead of the step's edge. He used a speaker to excite the oncoming flow, which forces some air to move into and out of a spanwise slit at various forcing amplitudes and frequencies. At the most effective forcing frequency at the highest amplitude, the mean reattachment length was reduced by approximately 35%. The most effective forcing frequency was around $Sr_h \approx 0.25$, or close to the natural vortex shedding frequency, which agreed with the findings of Sigurdson (1995), who investigated acoustic forcing on separated flow around bluff bodies. Similarly, Kang & Choi (2002) achieved a reduction in the mean reattachment length of about 20% with the use of suction and blowing through a slit similar to the one used by Chun et al.. Here the most efficient actuation frequency of the excitation was at $Sr_h = 0.2$, which is also very close to the vortex shedding frequency.

Another similar AFC concept next to the acoustic excitation of the shear layer is to discharge energy via plasma actuators into the boundary layer just ahead of the BFS. Recently, Bernard et al. (2016) excited the oncoming flow at $Sr_h = 0.25$ and achieved a 22% reduction in the mean reattachment length. However, the pressure fluctuations on the reattachment surface were amplified by up to 105% in intensity, while the PSD of the pressures showed several dominant peaks with flow control, whereas only one dominant broadband peak was observed without flow control. Thus, active flow control applied on a BFS can achieve a considerable reduction in the mean reattachment length, when the natural frequency of the shear layer is amplified. On the downside, amplifying the natural frequency of the shear layer strengthens its effects with respect to the dynamic loads. Furthermore, the integration of AFC on a launcher is not very feasible due to its complexity, which inherently introduces another critical source of error into the system that could lead to catastrophic failure.

The framework of this chapter lies in the investigation of PFC devices. Therefore, this literature review will use the above mentioned quantities for AFC as a reference and move

its focus onto PFC. In comparison to the amount of literature available for AFC aft of a BFS, very little work exists for PFC, even though passive devices are much more feasible to adapt into complex systems such as space vessels.

Nonetheless, passive devices are not necessarily less effective than active devices. In low speed conditions at 12 m/s, [Isomoto & Honami \(1989\)](#) showed that by increasing the near-wall turbulence level from 10% to 12.5% via a cavity or rod ahead of the step, a reduction of up to 25% in the mean reattachment length can be achieved. A reduction of 14% was also achieved by [Neumann & H. \(2003\)](#) in large eddy simulations (LES), who placed a fence into the spanwise direction ahead of the step. They also compared the fence to an array of actively pulsed blowing and suction actuators, and found identical results with respect to the reduction in the mean reattachment length. A further reduction was achieved by [Park et al. \(2007\)](#) by placing so-called tabs onto the edge of the BFS. They experimented with various tab sizes and distributions, reaching a 50% reduction in the reattachment length with the most effective configuration. These tabs increase the three-dimensional turbulent mixing aft of the step similarly as other passive approaches, thereby forcing the shear layer to reach equilibrium with the surrounding flow sooner. In other words, high-momentum flow from above the shear layer is brought into the recirculation region close to the wall. This results in an earlier reattachment process.

Another technological concept of increasing the three-dimensional turbulent mixing within the shear layer is the chevron mixer. On an axisymmetric BFS, [Schrijer et al. \(2010\)](#) investigated chevrons with several geometrical parameters, periodicities, as well as shapes at $Ma_\infty = 0.7$. According to their results, the mean reattachment location shifted downstream rather than upstream. The maximum backflow velocities increased as well in comparison to the baseline configuration. The influence of the flow control devices on the RMS fluctuations in the velocities was also minimal, however negative in the sense that the fluctuations actually increased. A minor positive effect was a slight reduction in the oscillatory growing and shrinking of the reverse flow region.

[Nilsson et al. \(2016\)](#) applied the chevrons on a planar BFS. Similar to the axisymmetric findings mentioned above, the effects of this type of flow control device were minimal with respect to the Reynolds stresses and negligible with respect to the reattachment location. Thus, it can be concluded that chevrons that do not protrude into the oncoming flow with an angle of attack do not add enough streamwise vorticity into the shear layer. A stronger means of streamwise vortex generators are required to achieve the desired effects. Chevrons are nowadays employed in gas turbines as a means of flow mixers in order to reduce jet noise. Another shear layer mixer used in gas turbines is the lobed mixer. According to [Mengle \(2005\)](#), they provide a higher sound pressure level reduction than chevron mixers, thus a more effective mixing process. Their drawback is that they cause higher thrust losses than the chevron mixer mainly due to the higher degree flow direction manipulation. For the purpose of solely reducing the loads experienced on the reattachment surface aft of a BFS where the drag is of secondary interest, the lobes could supply sufficient streamwise vorticity to the flow.

When the lobed mixer applied to gas turbine, a high-momentum, or -energy, core flow co-flows next to a low-momentum/energy bypass flow. Naturally, a shear exists between these two layers, a driving factor for mixing. In order to increase the mixing rate, a lobed mixer geometrically induces aerodynamic loading along the spanwise direction of the lobes. [Waitz et al. \(1997\)](#) showed that the streamwise vortices shedding off of such a wavy trailing edge are much larger in both, intensity and scale than the ones naturally developing in boundary layers and shear layers. Consequently, the turbulent mixing within the shear layer is enhanced, as counter-rotating vortices from neighboring lobes diffuse into one another. This ultimately breaks down the coherent structures, allowing the flow to become fully three-dimensional, which is a driving criterion for reattachment according to [Simpson \(1989\)](#). The results of [McCormick & Bennett Jr. \(1994\)](#) showed that in addition to the streamwise vorticity that a lobed mixer imprints onto the flow, Kelvin-Helmholtz instabilities stemming off of the convoluted trailing edge of such a mixer have a major effect on the mixing efficiency downstream. Thus, implementing such a convoluted trailing edge on a BFS provides for the enhanced mixing conditions of the shear layer, as there only exists flow on one side of the lobes, creating a large shear at their trailing edge.

By modifying the trailing edge of a BFS with lobes similar to the ones found in gas turbines, [Bolgar et al. \(2015, 2016\)](#) achieved a more than 75% reduction in the mean reattachment length. However, the work at that time did not give detailed insights into varying the size and the shape of the lobes. Also the dynamic pressure loads on the reattachment surface were not analyzed back then. [Scharnowski et al. \(2019a\)](#) implemented the lobes from [Bolgar et al.](#) onto an axisymmetric BFS in transonic conditions. The application of the lobes led to a 55% reduction in the mean reattachment length and up to a 30% reduction in the RMS pressure fluctuations on the reattachment surface. These results clearly show that the lobes provide the necessary flow manipulation to add streamwise vorticity to the shear layer, thereby decreasing the mean reattachment length as well as the load dynamics on the reattachment surface.

Therefore, a parameter study on lobe sizes and geometries on a planar BFS is conducted in this chapter. The first goal is to quantify the lobes' effectiveness in reducing the mean reattachment length. Another aim is to determine the lobes' ability to reduce the dynamic pressure loads on the reattachment surface. Lastly, the spatial spectra of the pressure loads need to be advantageous when compared to those of a generic BFS, in order for flow control not to pose any unforeseen disadvantages regarding harmful modes. In the previous chapter it was shown that the step mode is the main driving factor for the most dominant load fluctuations on the reattachment surface, while the reverse flow region is dominated by the cross-pumping mode. The effects of passive flow control on these modes are of paramount interest. Additionally, a space launcher has to accelerate through the supersonic regime. Therefore it is an important criteria for flow control not to provide disadvantages past the transonic regime, otherwise technologies would have to be developed to eject these devices after having successfully traveled through the transonic phase of flight.

6.2 Experimental setup

6.2.1 Test cases & BFS model

The transonic measurements were conducted at a total pressure of 1.73 bar and a Mach number of 0.80 ($Re_h = 180,000$), while the supersonic measurements were conducted at a total pressure of 2.20 bar and a Mach number of 2.00 ($Re_h = 210,000$). Table 6.1 provides an overview of the experimental conditions. The \pm values in the table indicate the standard deviation of each quantity during the measurements.

Table 6.1: Free-stream flow conditions of TWM for the two Mach numbers under investigation

Ma_∞	p_0 [bar]	p_∞ [bar]	T_0 [K]	U_∞ [$\frac{m}{s}$]	Re_h
0.80 ± 0.0008	1.73 ± 0.0017	1.129 ± 0.0012	291 ± 1.2	259	180,000
2.00 ± 0.0010	2.20 ± 0.0023	0.282 ± 0.0004	292 ± 1.6	509	210,000

Figure 6.1 shows essential details of the BFS model, as well as the PIV FOV used for the investigations. For more details about the model, the reader is referred to chapter 4.1.

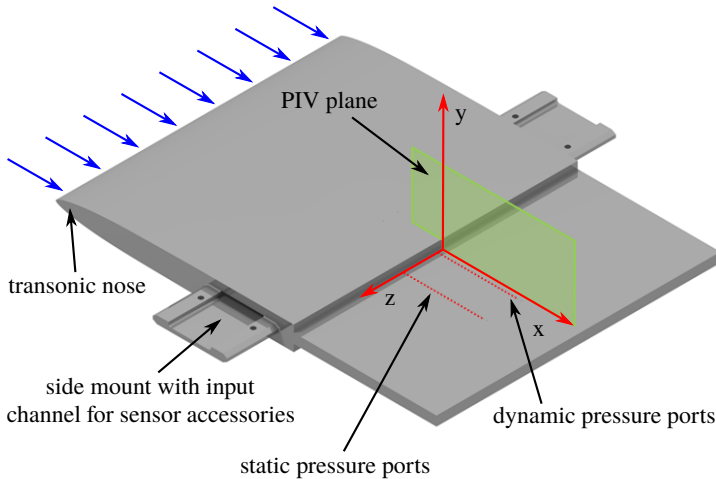


Figure 6.1: Illustration of the planar space launcher model with its pressure ports and the field of view under investigation

6.2.2 Flow control devices

The design of the flow control devices' shape emerged from the lobed mixer design used in gas turbines. As mentioned in the literature section of this chapter, the results of [Mengle \(2005\)](#) for instance, implied that these sort of mixers provide for the highest mixing efficiency in gas turbine shear layers. In other experiments, the author of this work noticed the existence of finger-like streamwise large-scale coherent structures, which was eventually published in [Scharnowski, Bolgar, & Kähler \(2015\)](#) and [Scharnowski, Bolgar, & Kähler \(2017\)](#). This led to the idea to imprint streamwise vorticity into the shear layer with the spatial frequency of the naturally appearing finger-like structures by means of a convoluted trailing edge, which closely resembles the shape of a lobed mixer.

A total of 7 PFC devices, where the trailing edge of the generic BFS was modified with the lobes, were investigated. These were comprised of 3 'full circular lobes' with different sizes, 3 'full square lobes' with similar sizes as the circular ones, and a 'half circular lobes' model, where the lobes protruding into the flow were replaced by a flat surface in order to reduce aerodynamic drag (refer to figure 6.2). For the remainder of this work the various geometries will be referred to as 'FC', 'FS', and 'HC', denoting either 'full circular', 'full square' or 'half circular' lobes, respectively. An additional letter 'S', 'M' or 'L' at the end will denote the lobe size for 'small', 'medium' or 'large', respectively. For example, 'FCS' will indicate 'full circular small' lobes. The generic BFS serving as a reference will be referred to as the 'baseline' case.

All lobes had a deflection angle of 18° either upwards or downwards from the horizontal plane. The lobes' radii of the 3 different sizes were $0.2h$, $0.3h$ and $0.4h$, while the periodicity was therefore 4 times the respective lobe radii. Similarly the square lobes had lobe protrusion heights of $0.2h$, $0.3h$ and $0.4h$ with their periodicity also being 4 times their protrusion height. The spatial periodicity of the largest lobes therefore closely represents the natural spatial periodicity of the streamwise coherent large-scale structures described by [Scharnowski et al. \(2017\)](#). Figure 6.2 also provides a schematic drawing of the different lobe geometries with dimensionless parameters. A shifted version of each flow control device exists, so that it is possible to measure the velocities from a vertically aligned PIV plane in the spanwise center of the test section (refer to figure 6.1), as well as to measure the pressure dynamics downstream of either the lobe peaks or valleys.

6.2.3 Particle image velocimetry

The PIV setup described in chapter 4.2.2 was used for the two-dimensional velocity field measurements. For each test case, 500 double images were recorded. The time separation between an image pair was $1.6\ \mu\text{s}$ and $0.8\ \mu\text{s}$ for $Ma_\infty = 0.80$ and $Ma_\infty = 2.00$, respectively. For data processing, the same pre-processing, evaluation methods, and post-processing steps were applied as described in chapter 4.2.2. During the PIV evaluation the final interrogation window size was reduced to 12×12 pixel with 50 percent overlap, yielding a vector grid

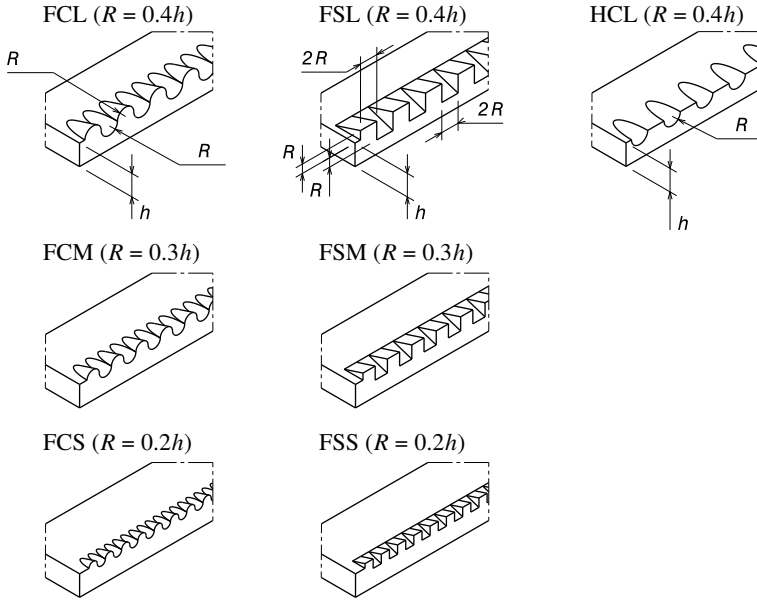


Figure 6.2: Modified BFS: Flow control devices under investigation

spacing of $210\ \mu\text{m}$.

6.2.4 Dynamic pressure measurements

The PIV measurements were complemented by dynamic pressure measurements identical to the ones described in chapter 5.2.3. The 24 available dynamic sensors were sampled simultaneously at a frequency of 25.6 kHz, gathering 128,000 samples in 5 s for each model configuration at both free-stream Mach numbers. All pressure ports were given a reference pressure from a static pressure sensor located on the wind tunnel wall at $x/h \approx -30$. For more details about the pressure measurements and its calibration the reader is referred to chapter 5.2.3.

6.3 Flow control results & discussion

6.3.1 Mean flow field & reattachment

Figure 6.3 compares the mean flow fields at $Ma_\infty = 0.80$ for the baseline case as well as the FCL and FSL configurations measured at the lobe peak and valley locations. One can

see that the mean reattachment location decreases drastically when flow control is applied, regardless of the measurement location (refer to table 6.2 for quantitative results). The mean reattachment for the baseline case occurs at $x_r/h = 6.0$. The FCL configuration reduces this by about 82% and 73% to $x_r/h \approx 1.1$ and $x_r/h \approx 1.6$ at the lobe valley and peak, respectively. A further reduction is achieved by the FSL configuration, reducing mean reattachment to $x_r/h \approx 1.0$ and $x_r/h = 1.2$ by 83% and 80% at the lobe valley and peak, respectively. The mean reattachment locations were determined by taking the first reliable vector above the surface, whose x -component of the velocity is positive. Since the mean reattachment locations were determined using standard PIV (refer to chapter 5.2.2) and not single-pixel ensemble correlation, the first reliable vector above the surface is at $y/h = 0.028$ or $200 \mu\text{m}$.

The large reduction in the mean reattachment is mainly achieved by introducing streamwise vorticity into the shear layer in a similar fashion as the tabs used by Park et al. (2007). The streamwise vortices add three-dimensionality to the flow, which according to Simpson (1989) is essential for a shear layer to reattach. The three-dimensional vortices enhance the entrainment and mixing behind the step, increasing the momentum close to the reattachment surface directly behind the step. This then leads to a shorter reattachment. This increase in momentum, for instance, can be seen in the larger absolute global minimum and maximum values of the mean streamwise component of the velocities in table 6.2. These minimum and maximum values were determined by applying a two-dimensional median filter with a dimension of 3×3 vectors over the mean flow field in order to smooth irregularities. Subsequently, a global search for the minimum and maximum scalars within the FOV yielded the listed quantities.

The results clearly reveal the higher effectiveness of the square lobes in reducing the mean reattachment length. This can also be attributed to the greater momentum exchange indicated by the larger absolute global minimum and maximum of the mean velocity scalars (refer to table 6.2). At the peak measurement locations, the upper reverse flow region is more distinctly separated from the reverse flow region close to the surface for the FSL case. This indicates that the two separated regions are independent from each other for the FSL case, while the reverse flow regions of the FCL case might rather be connected to each other. This will be further elaborated on in chapter 6.3.4.

With decreasing lobe size the mean reattachment increases, while remaining drastically shorter than the baseline case. At the lobe peak the FCS and the FSS configurations reduce the mean reattachment by approximately 48% and 57%, respectively. This can also be attributed to a lower momentum exchange with decreasing lobe size, which is supported by the fact that the absolute global minimum and maximum of the mean velocity scalars decrease in magnitude as seen in table 6.2. Hence, there is a direct relation between the amplitude of the streamwise vorticity and the entrainment, whereas the higher spatial frequency of the smaller lobe geometries does not counteract the smaller amplitude of its lobes in terms of three-dimensional mixing aft of the step. In figure 6.4 it can also be seen

Table 6.2: Mean flow field statistics at $Ma_\infty = 0.80$

BFS type	x_r/h	\bar{u}_{\max}/U_∞	\bar{u}_{\min}/U_∞	\bar{v}_{\max}/U_∞	\bar{v}_{\min}/U_∞
baseline	6.0	1.13	-0.22	0.05	-0.10
FCL valley	1.1	1.16	-0.03	0.35	-0.03
FCL peak	1.6	1.17	-0.31	0.12	-0.21
FCM peak	2.0	1.15	-0.15	0.13	-0.11
FCS peak	3.1	1.14	-0.26	0.10	-0.12
FSL valley	1.0	1.20	-0.02	0.42	-0.02
FSL peak	1.2	1.20	-0.32	0.10	-0.22
FSM peak	1.6	1.19	-0.32	0.25	-0.09
FSS peak	2.6	1.17	-0.31	0.10	-0.20

that the two distinct reverse flow regions, visible in the FSL case behind its peak, merge closer together with decreasing lobe size, combining into one common reverse flow region for the FCS and FSS cases. When only one common reverse flow region exists, it is to be expected that the phenomena and the intensities of the otherwise two separate reverse flow regions combine and amplify (refer to figure 6.9 for the increasing RMS pressure fluctuations with decreasing lobe size and to figure 6.13 for changes in the spatial PSD thereof). Overall, the results show that forcing the streamwise vorticity into the shear layer with the spatial periodicity of the naturally occurring finger-like structures results in the greatest reduction in the mean reattachment length. The square lobed geometries add more streamwise vorticity into the flow than their circular counterparts. Either configuration decreases the mean reattachment length significantly more than anything published in literature on BFS previously.

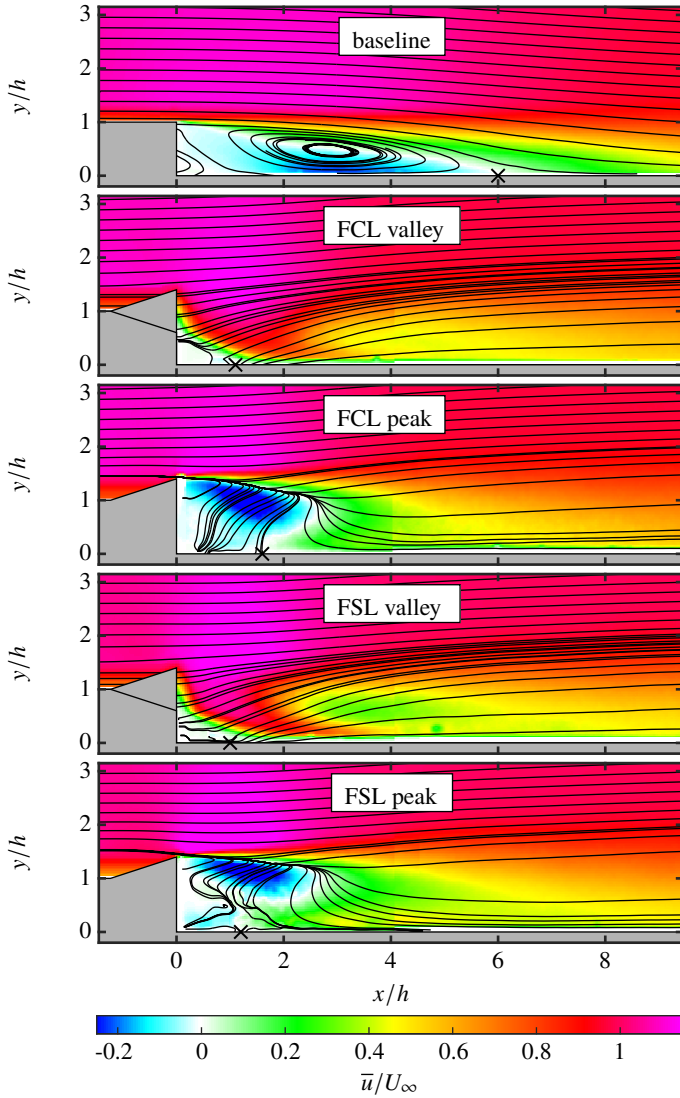


Figure 6.3: Streamwise component of the mean flow fields at $Ma_\infty = 0.80$ of the baseline vs. the FCL and FSL geometries at the lobes' valleys and peaks

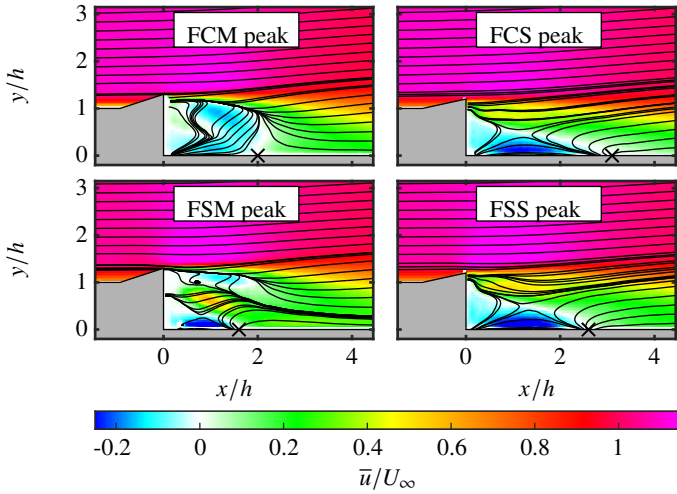


Figure 6.4: Streamwise component of the mean flow fields at $Ma_\infty = 0.80$ for decreasing lobe sizes of the full circular and full square lobes measured at the lobes' peaks

Even though the results with respect to reducing the mean reattachment length are positive in the transonic regime when using flow control, the flow control devices may cause excessive drag in the supersonic regime if they were to be placed on a space launcher, for instance. Figure 6.5 shows that the mean reattachment length aft of the lobe peaks is decreased by about 67% with the use of flow control in the supersonic regime as well. However, the existence of an oblique shock ahead of the FSL configuration's lobe peak protruding towards the incoming flow at $Ma_\infty = 2.00$ is visible as well. In contrast, the baseline case only has the supersonic expansion about the step. Thus, for supersonic applications it would be beneficial to have a lobe geometry that does not protrude into the incoming flow. For this reason the HCL configuration was developed, where only the valley part of the lobes exists and the lobe peaks are eliminated. This configuration was only investigated with dynamic pressure sensors, where the results are provided in chapter 6.3.3 and 6.3.4.

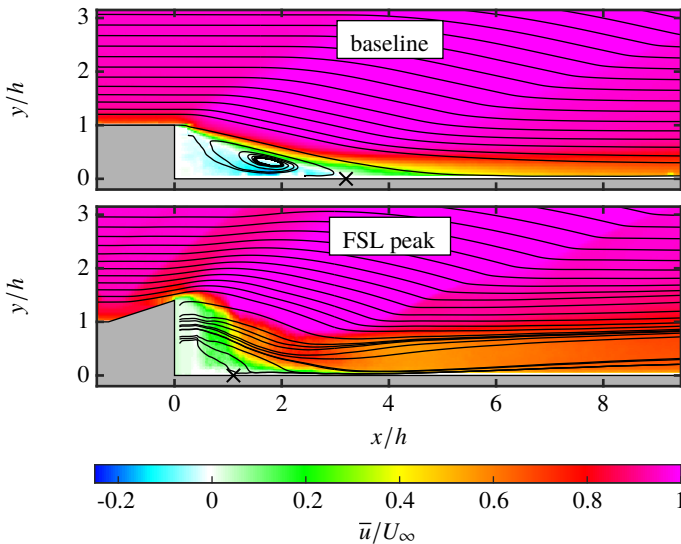


Figure 6.5: Streamwise component of the mean flow fields at $Ma_\infty = 2.00$ showing a local shock ahead of the step with flow control

6.3.2 Dynamic flow field statistics

When looking at the Reynolds shear stresses in figure 6.6, it can immediately be seen that the maximum values of the stresses increase behind the lobe peaks when comparing them to the baseline case. Behind the lobe valleys the Reynolds shear stresses remain around the same intensities. This indicates that the turbulence production occurs behind the lobe peaks outside of the recirculation region, far away from any surface as visualized by the contour lines of constant intensity. More importantly, from around $x/h = 3$ the stresses in near proximity of the reattachment surface are drastically lower with either flow control device (FCL and FSL) at both measurement locations (refer to outer most contour line of $\overline{u'v'}/U_\infty^2 = -0.003$). This already serves as an indicator that the pressure loads imposed on that surface will be lower with flow control than for the baseline case. This will be outlined in chapter 6.3.3. Furthermore, the FSL configuration provides lower stresses close to the surface when compared to the FCL configuration, making it better suited for reducing the velocity fluctuations just above the reattachment surface.

With decreasing lobe sizes, the shear stress regions of maximum intensity not only move closer towards the reattachment surface, but also new high intensity regions right above the reattachment surface develop (refer to figure 6.7). As previously seen with the reverse flow regions aft of the lobe peaks, the patches of high stresses merge together with decreasing lobe size, bringing the high intensity regions closer to the reattachment surface. This further implies that the phenomena from two distinct reverse flow regions combine and amplify in intensity. Again, the square lobed configurations have a greater distinction between the two patches than their circular lobed counterparts. Even though high intensity Reynolds stress regions develop close to the reattachment surface with decreasing lobe size, the intensities close to the surface aft of $x/h = 3$ are lower than for the baseline case.

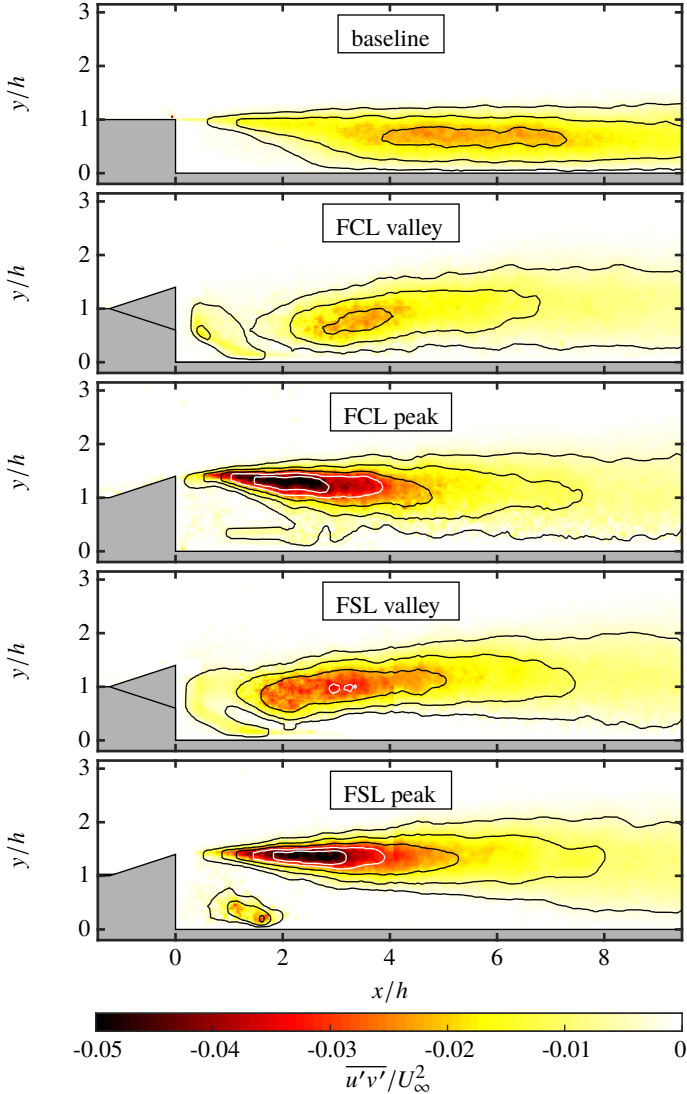


Figure 6.6: Reynolds shear stress distribution at $Ma_\infty = 0.80$ for the baseline vs. the FCL and FSL geometries at the lobes' valleys and peaks. Contour lines indicate $\overline{u'v'}/U_\infty^2 = -0.003, -0.01, -0.02, -0.03, -0.04$ towards the center.

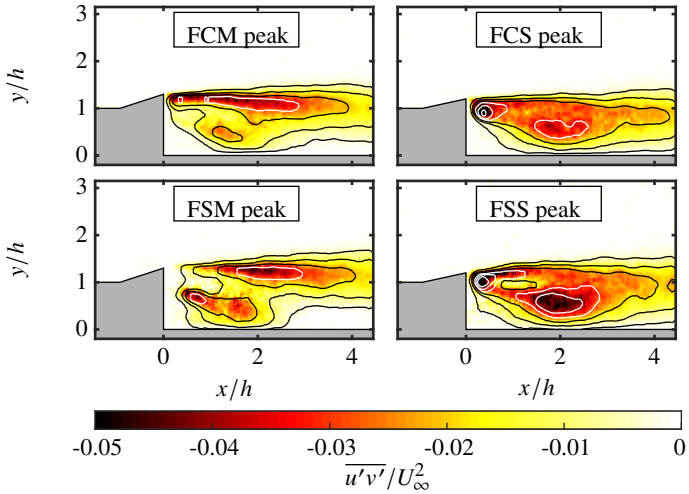


Figure 6.7: Comparison of the Reynolds shear stress distribution at $Ma_\infty = 0.80$ for decreasing lobe sizes of the full circular and full square lobes measured at the lobes' peaks. Contour lines indicate $\overline{u'v'}/U_\infty^2 = -0.003, -0.01, -0.02, -0.03, -0.04$ towards the center.

6.3.3 Mean pressures and RMS fluctuations on the reattachment surface

Transonic load reduction

As was the case in section 5.3.3, the reference pressure for the processing of the pressure data was adjusted to be at $x/h = -2.5$ and $x/h = -58.5$ for the sub- and supersonic cases, respectively. Figure 6.8 provides the mean and the RMS pressure coefficients normalized by the total pressure in the free-stream at $Ma_\infty = 0.80$ for the FCL, FSL, and HCL configurations measured behind the lobe peaks and valleys. On the top of the figure, the mean total pressure coefficient shows that the pressure recovery aft of the step occurs much further upstream with flow control. This is in good agreement with the drastic upstream shift of the mean reattachment location with flow control. The maximum positive gradient of the total pressure coefficient curve of the HCL configuration also indicates that for this configuration the mean reattachment would occur upstream of the baseline case, but further downstream than for the other flow control devices. For either flow control configuration, the respective pressure distributions behind either the lobe peaks or valleys are nearly matching, which is in contrast to the flow fields recorded with PIV. On the flow field images in figure 6.3, the large difference in the reverse flow region from peak to valley are rather noticeable. However, the flow velocities in near proximity of the reattachment surface are nearly identical, explaining the similarity of the mean pressure distributions behind the lobe peaks and valleys.

On the bottom of figure 6.8, the RMS pressures validate what the Reynolds shear stresses in chapter 6.3.2 already implied. With the FCL or the FSL configurations the RMS pressure fluctuations are decreased by nearly halved from around $x/h = 3$, when compared to the baseline case. The FSL configuration proves itself to be more effective in reducing the RMS pressure fluctuations by about 35% at $x/h = 7$. When calculating the integral between the baseline case's and the average of the FSL's RMS pressure fluctuations multiplied by the moment arm, an overall decrease of 25% in the dynamic moment about the step at $x/h = 0$ is achieved with this flow control device. An advantage of the FCL case's RMS distributions behind its lobe peaks and valleys is that they are more similar to each other. The HCL configuration reduces the RMS pressure fluctuations as well, but only from about $x/h = 5$, making it the least effective geometry. Ahead of $x/h = 5$, the HCL configuration also has slight differences in the distribution of the RMS pressure fluctuations behind the lobe peaks and valleys.

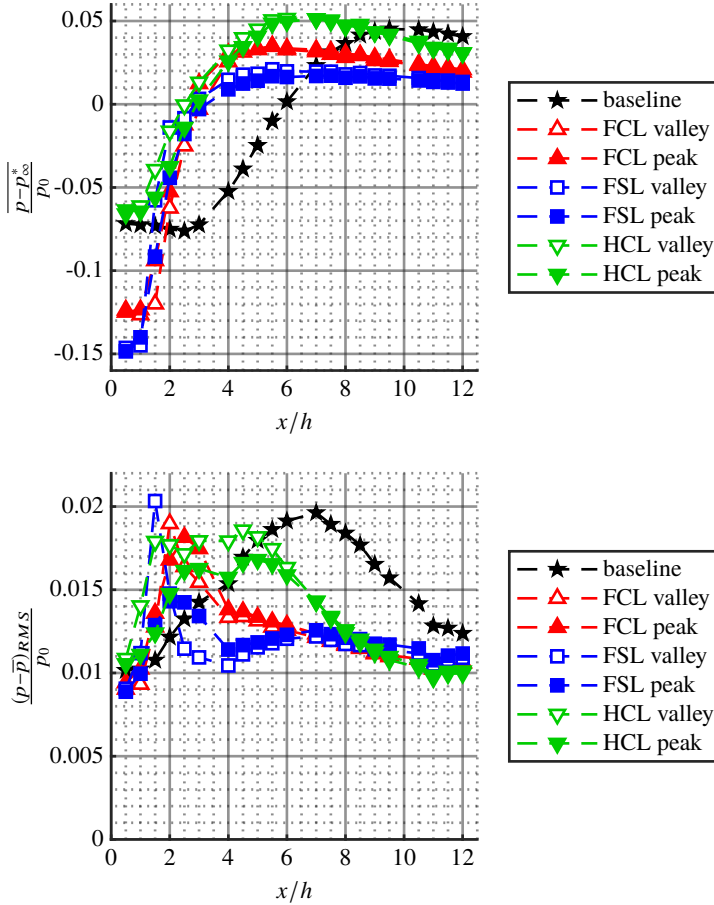


Figure 6.8: Comparison of the mean and RMS total pressures coefficients along the reattachment surface at $Ma_\infty = 0.80$ for all large lobe geometries measured behind the lobe valleys and peaks. The pressure p_∞^* indicates the far-field pressure at $x/h \approx -2.5$.

With decreasing lobe sizes, the flow control devices' effectiveness in pressure recovery, as well as in reducing the RMS pressure fluctuations, decreases slightly (refer to figure 6.9). Right away, the reader's attention is drawn to the large RMS peak value of the FSS case. In the Reynolds shear stresses it is visible how the two high intensity stress patches merged together into a common one. Thus, the peak in the RMS pressure fluctuations is probably to be caused by an amplification of the mode within this 'combined' reverse flow region. Nonetheless, all circular or square lobed configurations reduce the RMS pressure fluctuations aft of $x/h = 3 - 4$, depending on the geometry and size. In summary, the square lobe configurations are more effective in reducing the pressure fluctuations than their circular counterparts, while the circular lobe configurations have a more homogeneous distribution when comparing the data behind the lobe peaks and valleys. This can be attributed to the fact that the square lobes most likely generate more defined and stable vortex structures, which cause them to be more powerful, resulting in better shear layer mixing characteristics. The HCL configuration is the least effective, however it may be an attractive solution for objects traveling above sonic conditions. For the case of a space launcher, it is important that either flow control configuration not only reduces pressure fluctuations, but also the integral of the moment of the pressure fluctuations about the pivot point at $x/h = 0$.

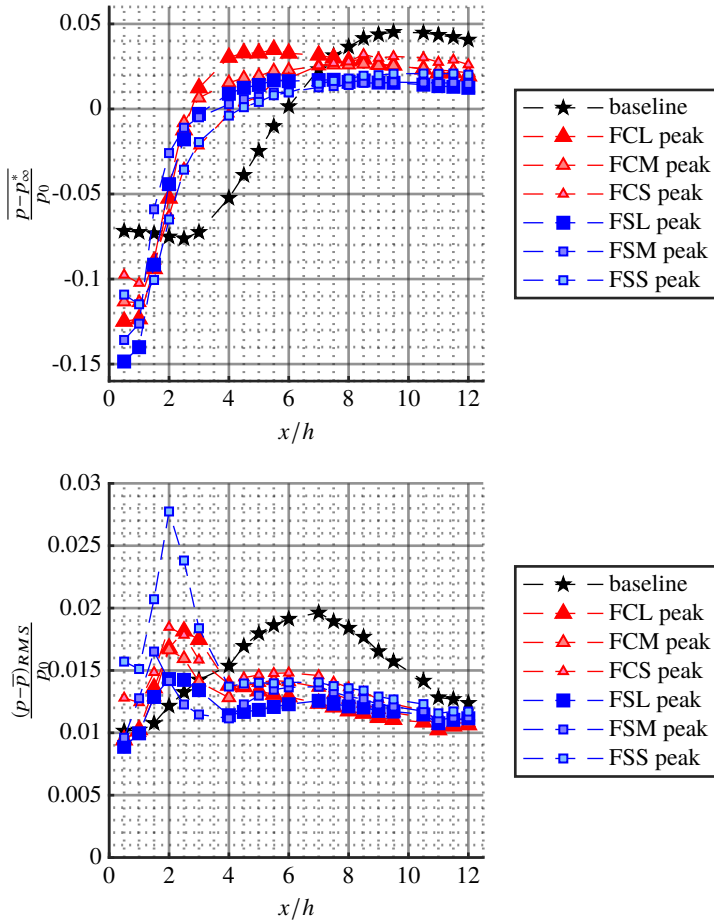


Figure 6.9: Comparison of the mean and RMS total pressures coefficients along the reattachment surface at $Ma_\infty = 0.80$ for the circular and square lobe geometries with decreasing size measured behind the lobe peaks. The pressure p_∞^* indicates the far-field pressure at $x/h \approx -2.5$.

Supersonic load reduction

Regardless of the drag deficit the FCL and FSL configurations provide in supersonic conditions ahead of the step, they still reduce the mean reattachment length as well as the RMS pressure fluctuations at $Ma_\infty = 2.00$, as can be seen in figure 6.10. For a space launcher, the pressure fluctuations in the supersonic regime are of secondary importance, since the maximum loads occur during the transonic regime. This is apparent in 6.10, where the RMS pressure fluctuations aft of the step are nearly an order of magnitude lower in the supersonic regime than in the transonic regime. Other applications might benefit from the fact that the passive flow control devices analyzed reduce the dynamics in these conditions from around $x/h = 3$. Again, the FSL geometry achieves a higher load reduction than the FCL geometry. Interestingly, the dynamic loads aft of the HCL peak are the lowest. For the HCL configuration, the RMS pressure fluctuation distributions behind the lobe peaks and valleys do not match as closely as for the other flow control devices. This can be attributed to the fact that behind the lobe peak of the HCL a supersonic expansion takes place, not allowing such a three-dimensional behavior as is forced onto the flow with the other lobes. It should be noted that when considering the mean total pressure coefficient distributions, all flow control devices reduce the pressure-induced drag aft of the step. Depending on the increase in friction drag on the reattachment surface due to the increased momentum of the flow, the HCL configuration could therefore lead to an overall drag reduction, since it does not provide an adverse pressure distribution ahead of the step like the other flow control devices.

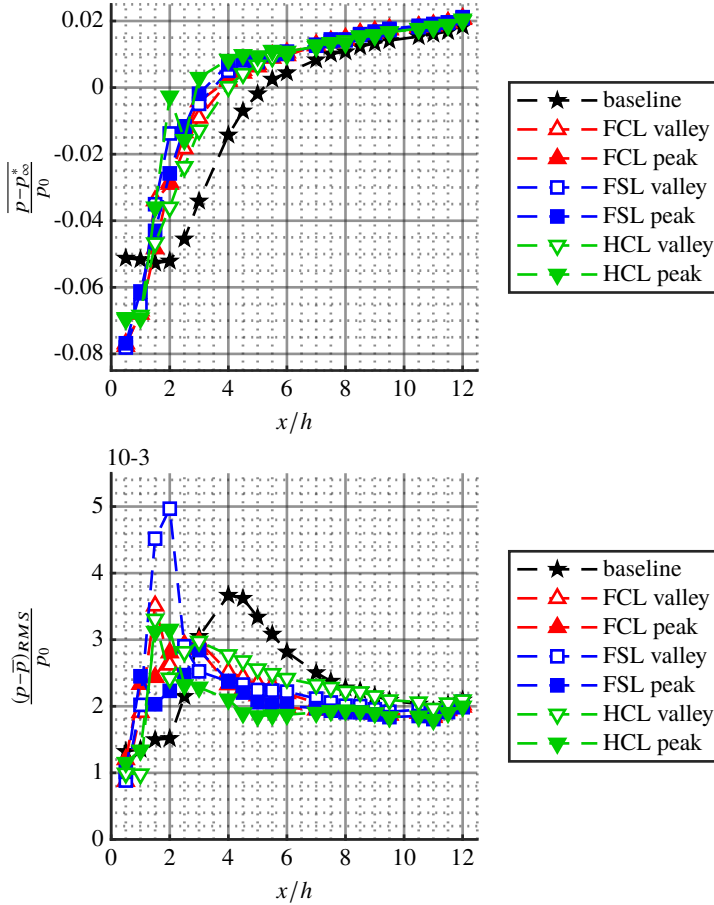


Figure 6.10: Comparison of the mean and RMS total pressures coefficients along the reattachment surface at $Ma_\infty = 2.00$ for all large lobe geometries measured behind the lobe valleys and peaks. The pressure p_∞^* indicates the far-field pressure at $x/h \approx -58.5$.

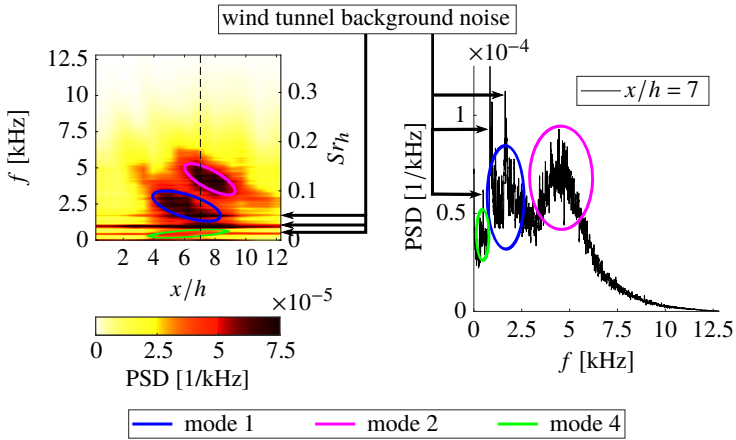


Figure 6.11: Left: Streamwise evolution of the PSD of the surface pressure fluctuations at $Ma_\infty = 0.80$ for the baseline case. Right: PSD extracted at $x/h = 7$ from the spectrogram in the left illustration.

6.3.4 Pressure spectra

Transonic spectra

The spectrograms provided in figures 6.11, 6.12 and 6.13 show the evolution of the PSD of the pressure fluctuations over the length of the reattachment surface from $x/h = 0.5 - 12$ for the baseline case and the controlled cases at $Ma_\infty = 0.80$. For a more detailed explanation of the spectrograms, the reader is referred to section 5.3.3.

For reference purposes, the baseline geometry's spectrogram at $Ma_\infty = 0.80$ with a 2D spectrum extracted at $x/h = 7$ is provided in figure 6.11. Identical to the results in chapter 5.3.3, the dominant peaks (shown in the dark colors at $f \approx 400\text{Hz}$, 1100Hz , 1700Hz) spanning horizontally across the spectrogram are the wind tunnel background noise. The patches in the spectrogram show the two major transonic modes identified in chapter 5.3.3 at $Ma_\infty = 0.80$ for the baseline case. As a reminder, mode 1 dominant around $Sr_h = 0.07$ is the cross-pumping mode, and mode 2 around $Sr_h = 0.13$ is the step mode. Mode 4 from section 5.3.3, can weakly be detected at $Ma_\infty = 0.80$. This was identified as the cross-flapping mode in chapter 5, with its frequency increasing between $x/h = 4 - 6$ below 1000Hz . Figure 6.11 on the right shows the spectrum at $x/h = 7$, as indicated by the dashed line in the spectrogram on the left part of the figure. At $x/h = 7$ the broadband cross-pumping mode centered around 2500Hz , as well as the step mode centered around 5000Hz are clearly visible. For a more detailed analysis of the modes, the reader is referred

back to chapter 5.3.3.

Chapter 5 concluded that the baseline case's high-intensity pressure fluctuations are dominated by the step mode. Hence, it can be assumed that it is this mode that mostly contributes towards the buffeting problems on the Ariane 5 space launcher. Therefore, it should be a key objective for flow control to reduce the intensity, or to even completely diffuse this mode.

Looking at the spectrograms of the FCL, FSL, and HCL configurations aft of the peaks and valleys of the lobes in figure 6.12, one can see how the passive flow control devices all effectively weaken the step mode, to say the least. The circular lobed configurations FCL and HCL provide very homogeneous spectra behind their respective lobe peaks and valleys.

For the HCL configuration, the three modes from the baseline case are still present. The step mode, present with its center around $x/h = 6$, is however weakened in amplitude by around 35%. Similarly, the cross-pumping mode's intensity is also decreased by about 25%. On the contrary, the HCL geometry amplifies the intensity of the low-frequency cross-flapping mode centered around $x/h \approx 2$ by about an order of magnitude. As the influence of this mode is negligible in excitation of buffeting, this can be considered an acceptable trade-off for applications like a space launcher.

The FCL geometry already seems to be able to diffuse the step mode effectively. Looking at its spectrograms, two distinct modes might still be present with this flow control device, but even so, the more rearwards patch is at a significantly lower frequency than the classical step mode. Thus, the streamwise vorticity created by the lobes effectively diffuses the harmful step mode and might already create modes that aren't associated with the classical modes behind a BFS. Regardless, the present mode or modes have a significantly lower amplitude (30% lower than the step mode) than the ones present in the baseline case.

The FSL geometry does this in a more pronounced fashion. Due to its discontinuous mathematical formulation from the center of a lobe valley to the center of a lobe peak, the square geometry is more favorable for creating high intensity vortices. Its spectrograms show no signature of the step mode behind the lobe valleys, and nearly no signature behind the lobe peaks. Even the one mode present behind the lobe peak is very weak in its intensity. For the FSL case, a dominant mode aft of the lobe valley develops. This mode is most likely caused by small spatial fluctuations of a recompression shock, as the in- and out-of-plane flow acceleration caused by the lobes may put the local flow slightly above sonic conditions. This locally limited peak in the spectrum is very similar to high-frequency peak of the supersonic baseline case at $Ma_\infty = 2.00$ shown in figure 6.14, or mode 2s in figure 5.16 in chapter 5.3.3.

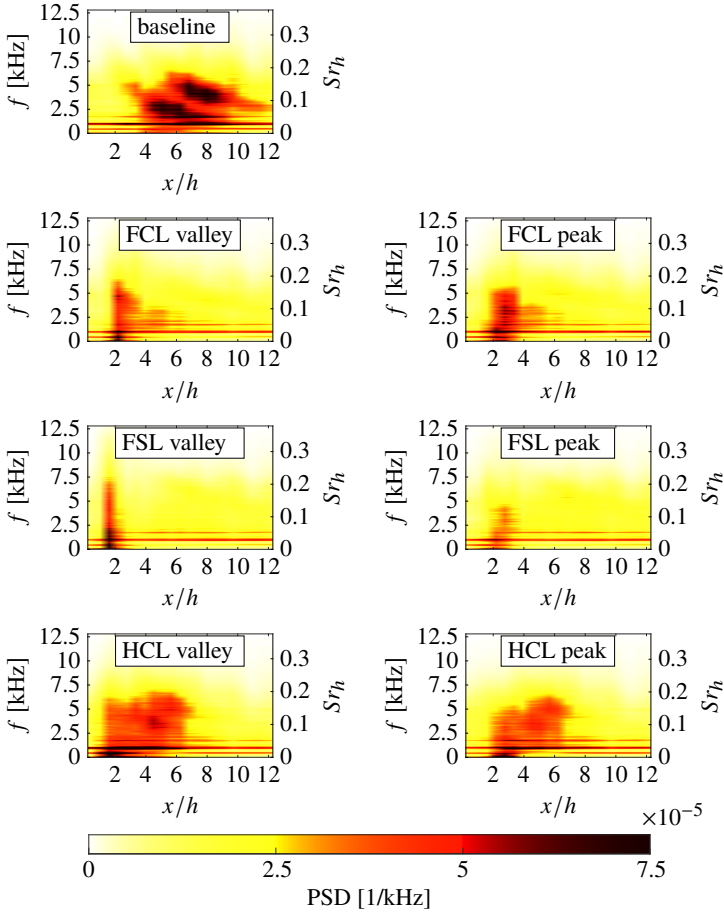


Figure 6.12: Comparison of the streamwise evolution of the PSD of the surface pressure fluctuations at $Ma_\infty = 0.80$ for all the large lobe geometries measured behind the lobe valleys and peaks

Figure 6.13 shows how the smaller lobes do not diffuse the step mode as effectively as their larger counterparts. For either configuration, both classical high-frequency modes, the cross-pumping mode further upstream, and the step mode downstream, are clearly present in the wall pressure signatures. This trend amplifies with decreasing lobe size. Again, the square lobed geometries are more effective in diffusing these classical BFS modes, however they are dominantly present for the FSS case. Furthermore, the intensity of the low-frequency mode close to the step also amplifies with decreasing lobe size. Due to its relatively high frequency for the FCS and the FSS cases, this mode is unlikely related to the cross-flapping mode found behind the baseline BFS. The peak in the RMS pressure fluctuations behind the FSS peak in figure 6.9 can be traced back to the amplification of this mode. In summary, even the smaller lobes are a beneficial passive flow control measure to not only lighten the dynamic loads as seen in chapter 6.3.3, but also to decrease the intensity of the harmful step mode.

The ability of the largest lobes (FCL & FSL) to diffuse the step mode successfully may be traced back to the lobes' periodicity, which was designed to be identical to that of the naturally developing large-scale streamwise structures aft of a BFS flow, as mentioned previously. However, it might also coincide with the fact that the largest lobes are just larger in their flow protrusion ($R = 0.4h$) than the boundary layer thickness ahead of the step ($\delta_{99} = 0.35h$). Studying the effect of these types of lobes' sizes by keeping their periodicity equal to the periodicity of the large-scale streamwise structures while changing their protrusion height, ultimately resulting in oval shaped lobes, could validate which parameter has a larger influence in diffusing the step mode.

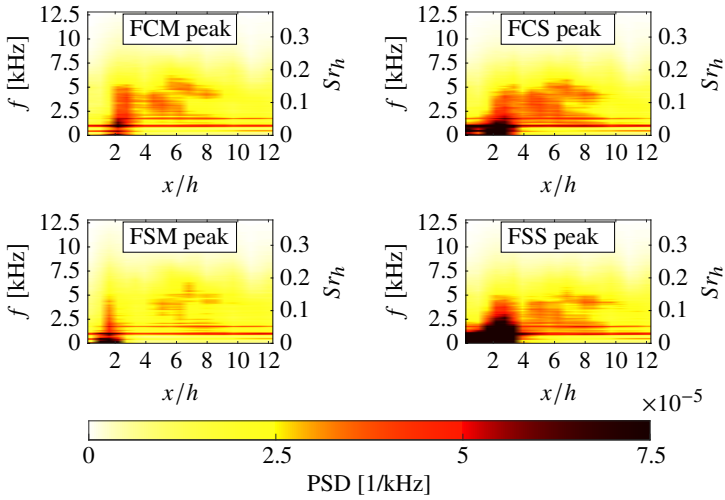


Figure 6.13: Comparison of the streamwise evolution of the PSD of the surface pressure fluctuations at $Ma_\infty = 0.80$ for the circular and square lobe geometries with decreasing size measured behind the lobe peaks

Supersonic spectra

In supersonic conditions at $Ma_\infty = 2.00$, the baseline case is dominated by a locally limited high-frequency mode dominant at $Sr_h \approx 0.05$ just aft of the mean reattachment location at $x/h = 4$, and a low-frequency mode below $Sr_h = 0.006$ spanning along the entire length of the reattachment surface downstream of mean reattachment (refer to chapter 5.3.3 for more details). The higher frequency mode can be characterized around 3000Hz. The narrow peak around 1600Hz is caused by the wind tunnel noise. As observed in chapter 5.3.3, the high-frequency band is most likely caused by small spatial fluctuations of the recompression shock, while the low-frequency mode is caused by pumping dynamics of the separated bubble. Previously, in chapter 6.3.2 it was shown that the RMS pressure fluctuations decrease in supersonic conditions compared to the transonic conditions, and that the application of flow control further reduces them. As buffeting does not occur in the supersonic regime, it is more important that the flow control devices do not have an adverse effect in this regime with respect to dominant modes.

Figure 6.14 compares the spectrograms of the baseline case versus the controlled cases at different measurement locations in supersonic free-stream conditions. It can be seen that the spectra stay very similar to that of the baseline case. The low-frequency pumping mode is present with all the flow control devices at similar amplitudes. Only the streamwise location from where this mode acts varies due to the different mean reattachment locations with flow control. This supports the hypothesis from chapter 5 that the supersonic flow regions are decoupled from the subsonic layer aft of flow separation.

The circular lobed FCL and HCL configurations also seem to stabilize the spatial fluctuations of the recompression shock, as that mode weakens and focuses in a smaller confined space.

The FSL configuration diffuses this mode completely behind the lobe valley, however amplifies its intensity aft of the lobe peaks by around a factor of 2.5 above 1000Hz. Below this frequency, the amplitudes are nearly identical. Considering the RMS pressure fluctuations, this is however within a reasonable limits.

In summary, when neglecting possible drag penalties, none of the flow control devices produce negative effects in supersonic conditions. The RMS pressure fluctuations decrease for all the flow control geometries and the spatial fluctuations of the recompression shock seem to be weakened and stabilized, besides aft of the FSL lobes' peaks. Therefore, in the supersonic regime the circular lobes have a small advantage with respect to the modes' intensity experienced by the reattachment surface. The HCL configuration is a good compromise for reducing the modes' intensity aft of a BFS, while not creating a large drag penalty in supersonic flight. Since the modes are over an order of magnitude weaker than in the transonic regime, this advantage can be of secondary interest.

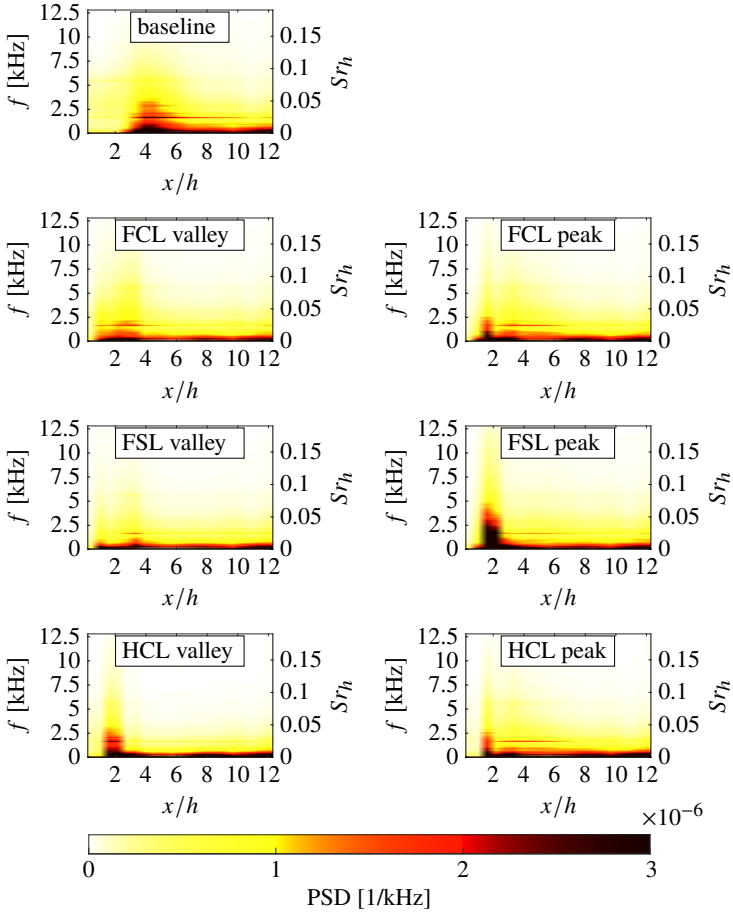


Figure 6.14: Comparison of the streamwise evolution of the PSD of the surface pressure fluctuations at $Ma_\infty = 2.00$ for all the lobe geometries measured behind the lobe valleys and peaks

6.4 Summary & conclusions on passive flow control aft of a BFS

Passive flow control devices aft of a BFS have been investigated with PIV and dynamic pressure transducers in transonic and supersonic conditions, and compared to a generic BFS. The PIV results show that the mean reattachment length can be reduced by as much as 80% (FSL) in the transonic regime, depending on the geometry and size of the flow control device. Even the least effective flow control device (FCS) investigated reduced the mean reattachment length by 48%. A parametric study was conducted with the flow control devices, comparing three different sizes of the same geometry for two different types of flow control devices. This showed that with decreasing lobe size the mean reattachment length increases. This is due to the fact that the larger lobes produce larger scale streamwise vorticity due to the higher momentum flow they receive from the upper portions of the boundary layer. As a reminder, the largest lobes protrude into the flow by nearly the height of the boundary layer. The results also show that the square lobed geometries provide shorter mean reattachment lengths than the circular ones. An alternative lobe design was developed in order to avoid excessive drag in supersonic conditions (HCL). According to the total pressure coefficients, this geometry also reduces the mean reattachment length, however not to the same extent as the other flow control devices in this chapter.

The dynamic pressure measurements showed that the RMS pressure fluctuations are also reduced from around $x/h = 3$ in the harmful transonic regime. Depending on the lobe geometry and size, the reduction was on the order of 35% at specific streamwise locations on the reattachment surface. This led to a decrease of 25% in the dynamic moment about the step. The most significant reduction was achieved by the FSL geometry. Thus, next to reducing the mean reattachment and with that the moment arm of the pressure fluctuations, also the mean intensity of the pressure fluctuations is reduced by applying the lobe geometries as a means for flow control. Even in the supersonic regime, the flow control devices provide a reduction in the dynamic loads from around $x/h = 3$ of up to 40%. When conducting the parametric study in transonic conditions, the dynamic pressure measurements showed a similar trend in the reduction of the RMS pressure fluctuations as the PIV results did for the reduction in the mean reattachment length. The effectiveness of the lobes in reducing the dynamic loads decreases with decreasing lobes size, while the square lobed geometries are more effective in doing so than the circular ones. Still, the FCS geometry still reduces the maximum RMS pressure fluctuations by over 25% in the transonic regime.

Lastly, the spatial spectra of the wall pressure signatures of the flow control devices were compared to the ones from the baseline case. In transonic free-stream conditions the results show that the harmful step mode is weakened with all flow control devices and measurably eliminated with the FSL configuration. Again, the square lobed geometries were more effective in weakening the step mode than the circular lobed geometries. This is due to the fact that the square geometries provide discontinuous edges aligned into the streamwise direction, which are more conducive to vortex production than the

mathematically continuous radii of the circular lobes. The weakening effect of the step mode decreases with decreasing lobe size. Thus, for the FCS configuration the classical BFS modes are visible in the PSD signatures. The ability to eliminate the step mode might be related to either the periodicity of the flow control devices, where the most effective geometries (FSL & FCL) had a periodicity of the naturally occurring large-scale streamwise structures aft of a BFS flow. The other possibility is that the effectiveness of the step mode's diffusion is related to the protrusion height of the flow control devices. As a reminder, the largest geometries' protrusion height was just above the boundary layer thickness ahead of the step. To validate which parameter is the driving factor in diffusing the step mode, future experiments should study lobes where either the periodicity of them is equal to that of the large-scale streamwise structures with changing protrusion heights, or keeping the protrusion height constant to the boundary layer thickness and changing the periodicity. In supersonic conditions none of the flow control devices provided any adverse effects when looking at the PSD. In order to avoid a large drag penalty in supersonic conditions when using the FSL configuration for instance, it would be possible to eject the flow control device after having passed the critical transonic phase. For example, a space launcher could abandon such a passive flow control device along with its boosters.

In conclusion, it can be said that the scientific results of the analyses lead to a better understanding of the key geometrical criteria of a passive flow control device applied to a BFS flow, and make it possible to design an effective solution for trans- and supersonic applications. The diffusion of the harmful step mode achieved with the FSL configuration answers the third research question defined in chapter 2, whether the most dominant driving factor of buffeting can be eliminated. All of the flow control devices are very useful for stabilizing the shear layer aft of a BFS flow. When a reduction of the mean reattachment or the RMS pressure fluctuations is of key interest, these passive flow control devices provide an easily implementable solution for future aerospace vessels that travel in, through, or above transonic conditions.

7 Design and validation of a nozzle model

This chapter outlines the design and the experimental validation of a supersonic nozzle integrated into the planar BFS model from the previous chapters. The successful control of the afterbody aerodynamics in the previous chapter allows for longer nozzle concepts for a better trajectory performance to be mounted on space launchers. Prior to the investigations of the Dual-Bell nozzle concept, which may contain more unknown flow features due to its higher complexity, a conventional rocket nozzle's interaction with an external flow is investigated in this chapter. For one, this provides insights on effects of the presence of a jet plume on the shear layer stemming off of a BFS. Vice-versa, the effect of the shear layer on the jet plume is also analyzed. This answers the question whether the shear layer dynamics from the BFS can cause a highly overexpanded nozzle flow to separate, a condition that can damage the nozzle structure. The results show that the presence of the jet plume has negligible effects on the shear layer dynamics, while the separated shear layer does not cause nozzle flow separation. This chapter is structured as follows:

- 7.1 Literature review of supersonic nozzle flow
- 7.2 Digital design of the nozzle model
- 7.3 Experimental setup
- 7.4 Integration and validation of the nozzle model in the TWM
- 7.5 Summary & conclusions on the TOC nozzle model

7.1 Literature review of supersonic nozzle flow

A convergent-divergent nozzle, such as proposed by [de Laval \(1894\)](#), allows a flow to accelerate into supersonic conditions. As with any nozzle, the flow acceleration converts the potential energy stored in a gas to kinetic energy. This relation can be deduced from the energy equation provided in equation 3.3. During the time of his invention, [de Laval](#) observed that the flow accelerated past the speed of sound but couldn't mathematically describe the governing physics behind it. By 1924, [Stodola \(1924\)](#) compiled an extensive book on steam and gas turbines, deriving the basic principles of sonic flow, summarizing the one-dimensional nozzle theory, and discussing the behavior of supersonic jets, amongst others. The key relation to explain the flow acceleration in a Laval nozzle past sonic conditions is given by the following derivation:

$$\frac{du}{u} = \frac{1}{Ma^2 - 1} \cdot \frac{dA}{A}$$

where $dA/A < 0$ for $Ma < 1$
 $dA/A = 0$ for $Ma = 1$
 $dA/A > 0$ for $Ma > 1$

(7.1)

where A is the cross-sectional area in a pipe. This equation basically describes that for below sonic conditions, a pipe flow can only accelerate if the pipe's cross-section decreases with streamwise distance. In contrast, in supersonic flow, a pipe flow can only accelerate if the pipe's cross-section increases. This is the reason why supersonic nozzles have the convergent-divergent shape, where sonic conditions are reached in the narrowest section of the nozzle, also referred to as the throat. A schematic of a convergent-divergent nozzle is provided in figure 7.1

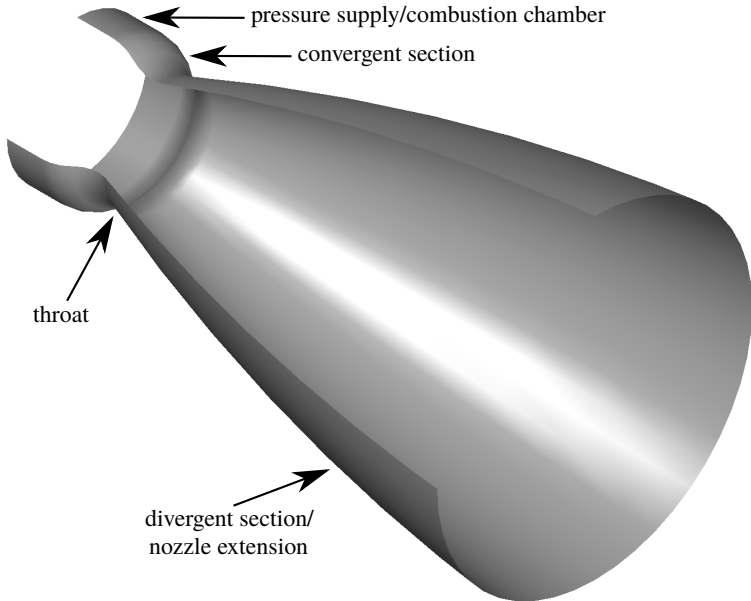


Figure 7.1: Illustration of a convergent-divergent nozzle with a thrust optimized contour

The jet plume exiting a supersonic nozzle can take on three fundamental shapes, depending on the relation of the nozzle exit pressure to the external pressure p_e/p_∞ .

This quantity is sometimes referred to as the static nozzle pressure ratio ($sNPR$) in rocketry and should not to be confused with the nozzle pressure ratio (NPR) defined with the total pressure of the nozzle flow such as:

$$NPR = \frac{p_{n,0}}{p_\infty} \quad (7.2)$$

Stodola showed the existence of an overexpanded jet when $p_e/p_\infty < 1$, an ideally expanded jet when $p_e/p_\infty \approx 1$, and an underexpanded jet when $p_e/p_\infty > 1$ (refer to figure 7.2 for a detailed sketch of the plume shapes). The overexpanded condition turned out to be the most critical one over the following years. This is due to the fact that an overexpansion inherently causes a shock within, or at the exit of the nozzle. As p_e/p_∞ decreases, the strength of the shock increases. Once a certain $sNPR$ is reached ($p_{\text{wall}}/p_\infty \approx 0.4$ as a rule of thumb) the flow cannot overcome the large pressure gradient across the shock, ultimately leading to flow separation at the foot of the shock within the divergent section of the nozzle. At this point, the shock starts to move into the nozzle with any further increase in the external pressure or decrease in the nozzle's total pressure. The flow separation in supersonic nozzles is a very dynamic process where the shock fluctuates three-dimensionally in space and time. This creates large pressure fluctuations on the nozzle contour, thus a structural problem. Therefore, nozzle flow separation is a critical condition to be avoided at all cost. Due to the increased interest in rocketry, a research interest on separated nozzle flow was sparked in the late forties.

First presented in the framework of the Jet Propulsion laboratory in 1948, the investigations on overexpanded nozzle flow by Summerfield et al. (1954) showed that an oblique shock forms within the nozzle, aft of which the flow separates along the nozzle contour due to the strong adverse pressure gradient. This was in contrast to the prevailing assumption that a normal shock would form within the nozzle. In his observations, the flow was deflected towards the center axis directly aft of the shock, forming a jet plume without reattachment to the nozzle contour. Wall pressure measurements along the nozzle contour showed that flow separation occurs only if the pressure along the wall drops below 40% of the ambient pressure, thus $p_{\text{wall}}/p_\infty \approx 0.4$. This was the first criterion for nozzle flow separation and is known as the Summerfield criterion today, which provides a good reference value for the initial design of nozzles. As research advanced with the years, it has been shown that lower $sNPR$ can be reached if certain criteria are met.

Experimental investigations on nozzle flow separation continued into the sixties in parts with rocket engines (Foster & Cowles 1949, Sunley & Ferriman 1964, Kalt & Badal 1965) and in parts with cold-gas nozzles (Scheller 1953, Fraser et al. 1959, Arens & Spiegler 1963, Lawrence 1967, Lawrence & Weynand 1968). Next to this, the research on supersonic nozzles also started to focus on the divergent section's contouring (Farley & Campbell 1960, Campbell & Farley 1960, Ahlberg et al. 1961, Bloomer et al. 1962). Summarizing the various results, it can be seen that the Reynolds number, the nozzle contour, planar versus axisymmetric nozzles, or the type of gas have very little influence on the p_e/p_∞ at which the

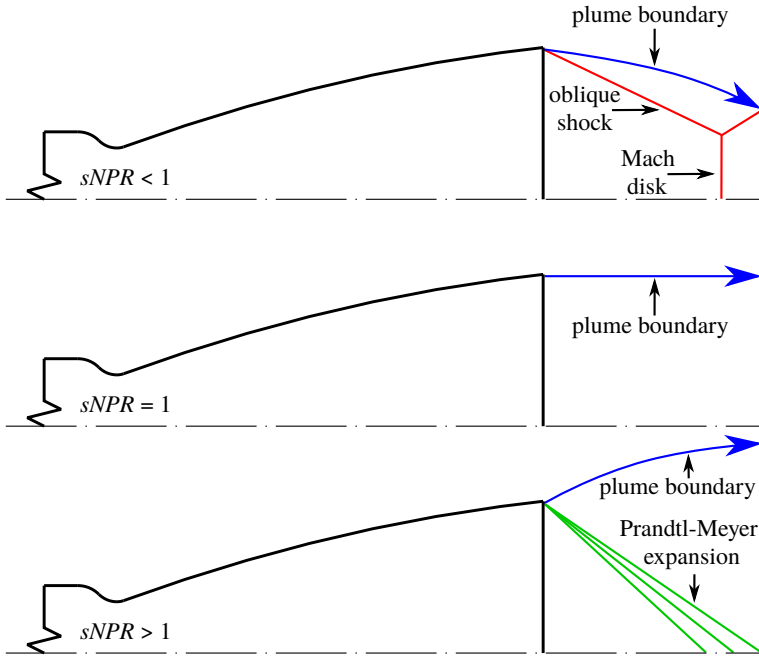


Figure 7.2: Various plume shapes dependent on $sNPR$

flow separates. However, a trend can be deduced that with increasing flow Mach numbers, a lower p_e/p_∞ can be reached before separation occurs. Subsequently, [Schmucker \(1973a\)](#) provides an empirically derived nozzle separation criterion as a function of the Mach number ($p_{sep}/p_\infty = f(Ma_{wall})$), using the available data from hot-gas experiments.

[Lawrence \(1967\)](#) identified two different mechanisms responsible for the pressure rise to ambient conditions when separation is present. The obvious mechanism is the pressure rise across the shock. However, aft of the shock the pressure is still below ambient conditions and further compresses to atmospheric conditions throughout the separated region. Thus, he suggested formulating future separation criteria within supersonic nozzles which account for each mechanism separately.

Nozzle flow separation with subsequent reattachment was first identified by [Nave & Coffey \(1973\)](#) in cold-gas experiments with a sub-scale J-2S rocket engine model. The authors were able to capture this phenomenon with a combination of pressure measurements along the streamwise direction of the nozzle wall and schlieren recordings. [Nave & Coffey](#) believed that this phenomenon was limited to small-scale nozzles, hence a function of the

Reynolds number which could be traced back to a laminar boundary layer. A phenomenon of relaminarization is known to occur in small-scale nozzles, where the initially turbulent flow accelerates towards the throat of the nozzle, thereby becoming laminar again (refer to e.g. [Krevskovsky et al. \(1974\)](#) for wind tunnel nozzles or [Stark & Wagner \(2009\)](#) for model rocket nozzles).

The investigations of [Nave & Coffey \(1973\)](#) also included full-scale test rig runs of the J-2S. A camera recorded a condensation ring along the inner wall of the nozzle, which gave a good indication of the separation location. For the first time it was shown that separation does not occur symmetrically about the axis of rotation, but rather in a three-dimensional fashion. This phenomenon causes side loads in rocket nozzles, which can lead to the ovalization of the nozzle, ultimately resulting in critical structural damage.

The omnipresent difficulty in dealing with side loads in rocket nozzles is also a major focus of research around the seventies. For example, [Lawrence \(1967\)](#) made the first side load calculations on a 2D nozzle with asymmetric separation. [Nave & Coffey \(1973\)](#) investigates the side loads on the J-2S engine, as well as on the previously mentioned sub-scale cold-gas nozzle. A major milestone in the characterization of nozzle side loads was achieved by [Schmucker \(1973b\)](#). He proposed that the side loads are a direct consequence of the flow separation within the nozzle, which occurs in an unsymmetrical dynamic fashion.

In more recent years, [Frey \(2001\)](#) investigated nozzle separation and its effect on side loads for different nozzle contours. He came up with a more accurate separation criterion, which accounts for the pressure rise across the shock and the pressure rise in the recirculation zone separately, as suggested by [Lawrence \(1967\)](#). Furthermore, it was shown that the RSS is not necessarily a low-Reynolds-number phenomenon, but rather caused by the shape of the nozzle contour. He discovered that reattachment within the nozzle is more likely to occur with a thrust optimized contour (TOC), due to the inner shock pattern generated by this type of geometry. The existence of a RSS was verified on a Vulcain rocket motor. [Frey](#) also found supporting evidence for [Schmucker's](#) hypothesis that the side loads are a direct consequence of nozzle flow separation. By measuring the dynamic pressure on opposing sides of the nozzle, an apparent anti-correlation in the pressure fluctuations due to the separated flow was found. It was also shown experimentally that the side loads increase with increasing amplitudes of the pressure fluctuations.

Since for the applied case of a rocket motor, the most critical phase for flow separation and the accompanying side loads is the start up procedure (rising pressure in the combustion chamber and high atmospheric pressure \rightarrow lowest p_e/p_∞), barely any attention has been paid to in-flight conditions. The previous chapters outlined how the rear section of an Ariane 5 launcher experiences high pressure fluctuations. [Depres et al. \(2004\)](#) investigated the effect of a jet plume on the recirculation region aft of a SR. In transonic conditions, the presence of the jet plume had very little effect on the pressure dynamics on the reattachment surface of a long nozzle fairing, when its length ratio was similar to that of Ariane 5. Even though the work of [Depres et al.](#) studied the effect of the jet plume on the shear layer, he neglected the effect of the shear layer on the jet plume. Therefore, it is one of the goals

of this chapter to analyze whether these highly dynamic pressure fluctuations close to the nozzle exit can cause nozzle flow separation for highly overexpanded nozzles in flight. In order to do so, the BFS step model used in the previous chapters is fitted with a planar thrust optimized contour (TOC) nozzle from which unheated pressurized air is exhausted, while subjected to an external flow in the wind tunnel.

7.2 Design of the nozzle model

7.2.1 Thrust chamber design

For the scope of this work, the thrust chamber is considered to be the streamwise aligned portion ahead of the convergent section of the nozzle (refer to figure 7.3). For a spanwise uniform nozzle flow, it is essential for the thrust chamber to provide an already spanwise uniform flow. Since the nozzle model used in the TWM had to fulfill many requirements with respect to its dimensions, shape, structural properties, and its integration and installation in the wind tunnel facility, the options on how to design a satisfactory thrust chamber were limited. One of the main requirements was that the nozzle would have a spanwise width of $1/3$ of the test section, or 100 mm. A honeycomb structure for homogenizing the flow aft of the 90° turn ahead of the thrust chamber would have required to be placed in the main body of the model with a thickness of 25 mm. This is due to the fact that the nozzle portion of the model has a thickness of 10 mm, where the thrust chamber has a channel height of 4 mm. Thus, the wall thickness on each side of the channel was already limited to 3 mm. Placing a honeycomb structure there, could possibly have compromised the structural integrity of the nozzle. More importantly however, the flow in the thrust chamber reaches velocities of around 150 m/s. Therefore, a honeycomb mesh with a finite thickness would have generated excessive losses and a wake.

2D CFD simulations of the thrust chamber

A channel, which allows for the placement of a honeycomb mesh in the main body, was analyzed with a two-dimensional CFD solver. For this, a structured mesh on one of the symmetrical sides of the model was created in ANSYS ICEM, resolving the boundary layer on the walls up to a dimensionless wall unit of $y^+ < 1$. The 2D flow simulations were carried out in ANSYS FLUENT, where the domain was defined with a velocity inlet, a pressure outlet, and adiabatic no-slip walls for its boundaries. The solver was set up to solve compressible Reynolds-averaged Navier-Stokes equations (RANS), modeling the turbulence with the shear stress transport (SST) turbulence model. The velocity at the model's inlet was reverse calculated with the one-dimensional nozzle theory from the nozzle's desired exit conditions. This yielded an inlet velocity of 32 m/s at the pressure reservoir's total temperature of 288 K. The pressure at the exit boundary, which is the start of the thrust chamber, was set at the maximum desired total pressure of 10 bar. The simulation

was iterated until the RMS residuals of the equations showed acceptable convergence. Due to the large regions of separated flow, the residuals were on the order of 1×10^{-3} .

One symmetrical half of the configuration under investigation had a slight cross-section decrease from a 52mm inlet to a 50mm outlet into the direction of the flow. This would yield the desired minimum of a 100mm wide thrust chamber. Large separated regions were present throughout the domain, as well as at the outlet boundary (refer to the streamwise velocity distribution on the lower half of figure 7.3). A streamwise maximum of approximately 65m/s is accompanied by a minimum of around -20 m/s at the outlet boundary. This is due to the large change in the pressure gradient after the bend in the channel. Thus, without an excessively large decrease in the cross-section, it was not possible to design a channel providing uniform flow conditions into the thrust chamber.

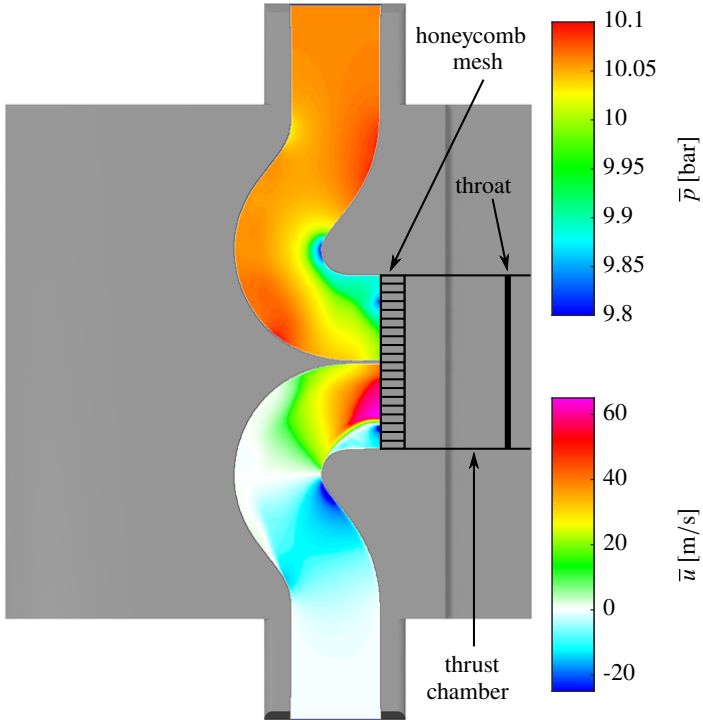


Figure 7.3: 2D CFD analysis of a flow channel for implementing a honeycomb flow straightener. The static pressure distribution is displayed on the upper symmetrical half of the flow channel. The streamwise component of the mean velocity is illustrated on the lower half of the flow channel.

3D CFD simulations of the thrust chamber

Without a honeycomb mesh as a flow straightener, the model's contouring had to provide the uniform flow distribution at the outlet boundary. One option was to place guide vanes into section where the flow has to turn by 90° . Another option was to fully rely on the decrease in the cross-section, which was implemented into the 90° turn, that leads to an increase in the flow velocity and a favorable pressure gradient, ultimately avoiding separation.

Amongst others, these two options were compared with CFD. Unstructured meshes with roughly 2.5M cells were generated with ANSYS ICEM, discretizing the wind tunnel model from its pressure supply up to the convergent section of the nozzle. The boundary layer was resolved up to a dimensionless wall unit of $y^+ < 1$ with a structured prism layer divided into 15 linearly growing portions. ANSYS CFX was used as the 3D solver, which was set up to solve compressible RANS, modeling the turbulence with the SST turbulence model. The boundary conditions were set up identical to those of the 2D simulation. The simulation was iterated until the RMS residuals of the equations showed a convergence of $< 1 \times 10^{-5}$.

The results show that the model with the guide vanes achieves the desired flow turning with a relatively uniform velocity and pressure distribution at the outlet boundary (refer to the upper half of figure 7.4). However, wakes from the guide vanes are present, where the streamwise component of the velocity is 125 m/s at the outlet boundary at the spanwise portions trailing the guide vanes. The rest of the outlet boundary has flow velocities on the order of 150 m/s. Therefore it was decided to compute a configuration without the guide vanes.

The configuration without guide vanes also achieves the flow turning without any flow separation (refer to the lower half of figure 7.4). Therefore, the significant contraction of the cross-section from $52 \text{ mm} \times 15 \text{ mm}$ to $50 \text{ mm} \times 4 \text{ mm}$ along the 90° turn sufficiently accelerates the flow, providing a favorable pressure gradient. Since this configuration does not generate a wake and the flow profile at the outlet boundary is uniform, it was decided to continue the design phase with this layout.

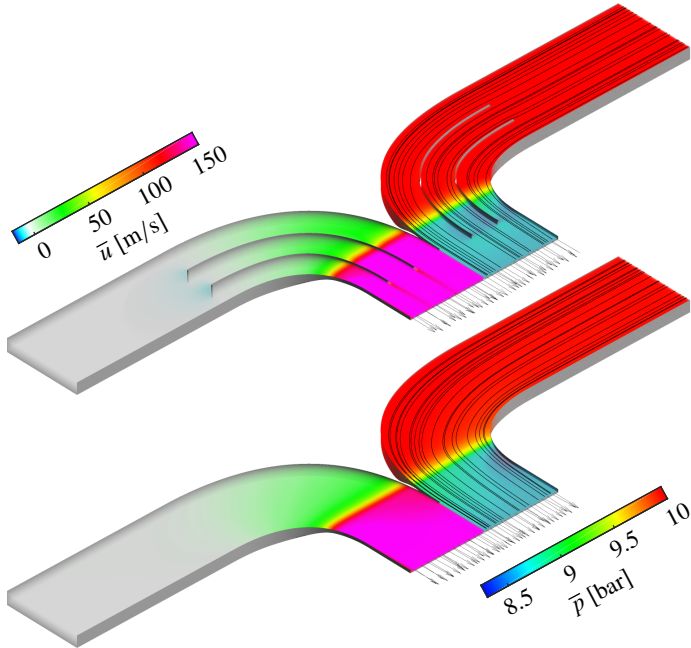


Figure 7.4: 3D CFD analysis of flow channels with decreasing cross-sections in the 90° turn. Top: Flow channel with guide vanes. Bottom: Flow channel without guide vanes. Note that only the lower symmetry half of the flow channel is shown. The streamwise components of the mean velocity are shown in the left-hand channels. The pressure distributions are shown in the right-hand channels.

7.2.2 Nozzle design

After having determined a viable thrust chamber design, the flow condition of the nozzle had to be verified prior to manufacturing. The main criterion for the nozzle flow was to provide a fully attached flow, without any nozzle flow separation, at the desired free-stream conditions. The TOC nozzle was designed to provide a $p_e/p_\infty = 0.5$ at a total pressure of $p_{n,0} = 8$ bar at free-stream conditions of $Ma_\infty = 0.80$ and $p_0 = 1.2$ bar. According to the one-dimensional nozzle theory, this yields a nozzle exit Mach number of $Ma_e = 2.61$. After an initial 2D CFD simulation on the nozzle contour, the total pressure losses in the thrust chamber and nozzle extension were determined separately. Combined they yielded a total pressure recovery factor of $PR = 0.96$. This quantity was considered in the final design of the nozzle's contour, ensuring the desired $sNPR$. When the PR is considered, the one-dimensional nozzle theory yields a nozzle exit Mach number of $Ma_e = 2.59$. For more details on the nozzle contour refer to chapter 7.3.1.

The 2D CFD simulations on the nozzle contour were carried out in ANSYS FLUENT on a structured mesh generated in ANSYS ICEM, resolving the boundary layer on the walls up to a dimensionless wall unit of $y^+ < 1$. The solver was set up to solve compressible RANS equations, modeling the near-wall turbulence with the Spalart-Allmaras turbulence model. According to a study on turbulence models for nozzle flow separation by Stark & Hagemann (2007), this turbulence model is the most reliable for predicting the occurrence and location of nozzle flow separation. The domain discretized one symmetrical half of the nozzle, including a 50 mm long thrust chamber which enables the build-up of a boundary layer, and one half of the TWM's test section. A 50 mm nozzle fairing extended upstream from the nozzle's lip to the inlet boundary of the TWM. This would ultimately allow for a cross talk between the external and the nozzle flow. The inlet boundary of the TWM was set up as a velocity inlet at 258 m/s. The nozzle's inlet boundary was set up as pressure inlet at a total pressure of 8 bar. The domain's outlet boundary was placed 600 mm downstream of the test section's inlet boundary, in order to avoid unsteady effects on the boundary. The outlet boundary was set up as a pressure outlet at a static pressure of 0.787 bar. All inlet and outlet boundaries were set at the TWM's reservoir total temperature of 288 K. The nozzle and test section walls were all set up as adiabatic no-slip walls.

The results in figure 7.5 show that the nozzle is fully flowing without any flow separation. The expansion, indicated in the pressure field above the symmetry plane, shows that the flow expands to around 0.4 bar at the nozzle exit as intended by the design $sNPR$. The flow velocity at the nozzle exit reaches around 580 m/s, which would correspond to $Ma_e = 2.59$ at the given temperature. Thus, the nozzle performs as desired at its design condition. Prior to manufacturing, a structural analysis had to be performed to validate the overall design. This is summarized in chapter 7.2.3.

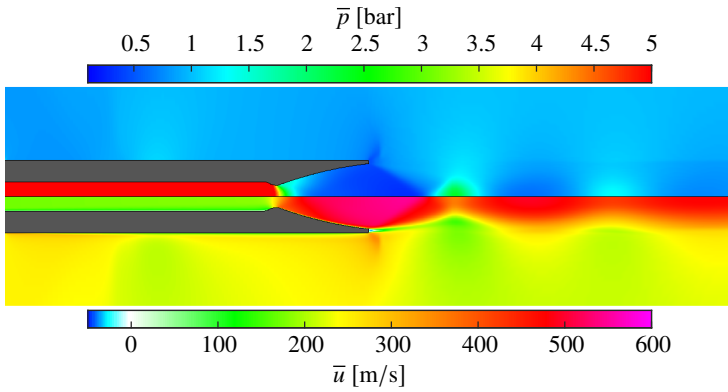


Figure 7.5: 2D CFD analysis of the final TOC nozzle at desired operating conditions. The upper symmetry half indicates the mean static pressure distribution. The lower symmetry half indicates the mean streamwise velocity distribution.

7.2.3 Structural analysis

The planar nozzle model is comprised of a main body with two halves and the various nozzle types, also milled from 2 halves. An illustration of the main body with a TOC nozzle attached to it is provided in figure 7.6 at the top. Since the internals of the models are pressurized by up to 10 bar absolute, a finite element method (FEM) structural analysis had to be carried out, in order to verify the structural integrity of the models.

This was carried out on CATIA V5 software by inputting the material properties, the pressure forces, and generating an unstructured mesh about the model. The model was to be milled from Toolox 33, a pre-hardened tooling steel. It is characterized by a metallurgically pure compound, a high impact toughness, and a good dimensional stability after machining due to low residual stresses. It has a hardness of 300 HBW and a tensile strength of 980 MPa, a yield strength of 850 MPa, and a Young's modulus of 210 GPa/m^2 at 20°C .

Applying a 10 bar pressure differential to the internal surfaces, the results of the FEM analysis show that the maximum stresses in three-dimensional space are around a factor of 2 lower than the yield strength of the material (refer to figure 7.6 in the middle). It is also to be noted that a deformation occurs, which reaches its maximum displacement of around 0.4 mm in the center of the nozzle lip (refer to figure 7.6 at the bottom). These are extreme values, since a 10 bar pressure differential between the model internals and its exterior is overestimated by at least 0.3 bar, depending on the free-stream conditions. Also, most nozzle tests are carried out at total pressures closer to 6 bar. However, one can see that these boundary conditions limit the spanwise width of the nozzle, for instance. Overall, the FEM analysis proved that the model is capable of withstanding high pressure levels without suffering plastic deformation or risking damage to the wind tunnel facility.

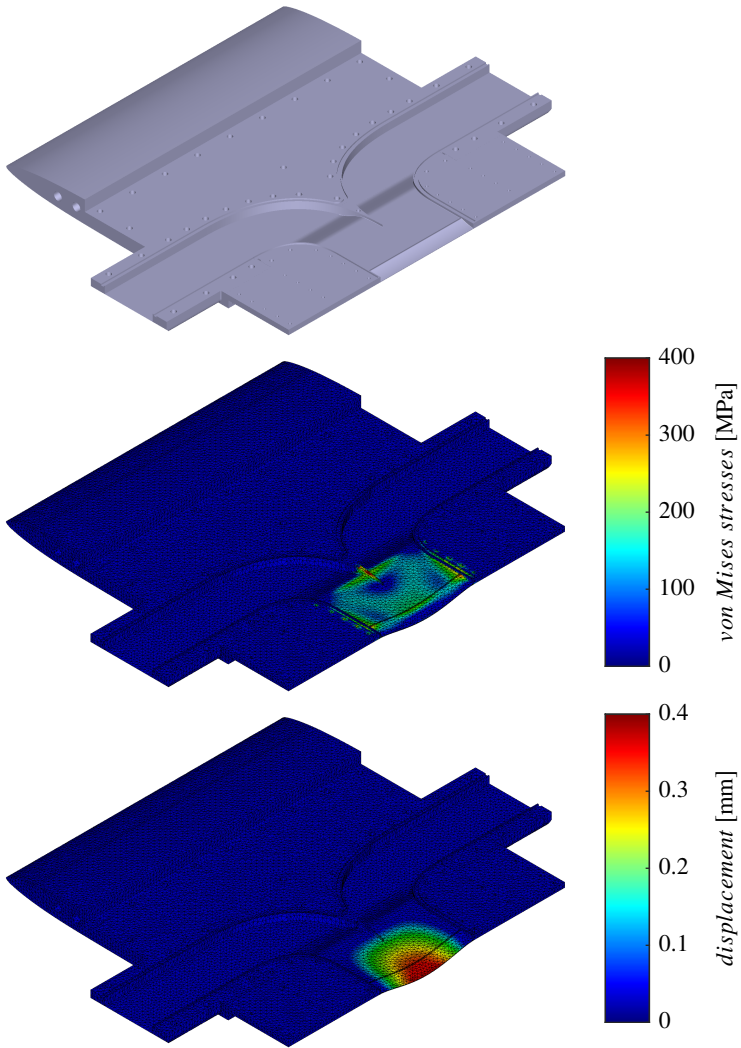


Figure 7.6: FEM analysis of the nozzle model at 9 bar pressure differential. Top: illustration of model internals. Middle: von Misses stress distribution. Bottom: model displacement.

7.3 Experimental setup

7.3.1 The thrust optimized nozzle model

The forebody of the model up to the BFS is nearly identical to the overall model dimensions described in chapter 4.1. The only difference is an increase of 5 mm in the flat plate portion's length prior to the step. The splitter plate's length has been decreased to 50 mm. This provides a similar nozzle fairing length with respect to the mean reattachment location at $Ma_\infty = 0.80$ to Ariane 5, where mean reattachment occurs around 90% of the afterbody's length (Hannemann et al. 2011). The nozzle fairing replaces the splitter plate from the previous model. It has an external height of 10 mm including the nozzle lips. The inner portion of the 2D nozzle is 9 mm in height and spans 100 mm across the model's center. It is a TOC nozzle designed according to Rao's criteria with a length ratio of 100% when compared to a 15° conical nozzle, an initial angle of $\theta_n = 20^\circ$ at the contour junction with the throat radius, and an exit angle of $\theta_e = 8^\circ$. The nozzle was designed to operate at a total pressure of 8 bar in the thrust chamber with a static pressure ratio of $p_e/p_\infty = 0.5$ at $Ma_\infty = 0.80$. However, it was only run at a total pressure of 6 bar, yielding a static nozzle pressure ratio of $p_e/p_\infty = 0.388$ at $Ma_\infty = 0.8$, which is much closer to the Summerfield criterion modified by Frey. The nozzle throat is 3.04 mm high, giving it an expansion ratio of $\varepsilon = 2.96$, resulting in a design exit Mach number of 2.59. Based on its throat height, the nozzle has a Reynolds number of $Re^* = 270,000$ at $p_{n,0} = 6$ bar. The thrust chamber is fed by two 2" hoses (refer to figure 7.7), one on either side of the model. The thrust chamber and the model are both symmetric about the horizontal and streamwise vertical planes. Figure 7.7 illustrates the TOC nozzle model. The boundary conditions of the TOC nozzle for the underlying experiments are given in table 7.1.

Table 7.1: Nozzle conditions for experiments under investigation

Ma_∞	$p_{n,0}$ [bar]	NPR
0.80	5.95 ± 0.05	≈ 7
2.00	5.95 ± 0.05	≈ 18.75

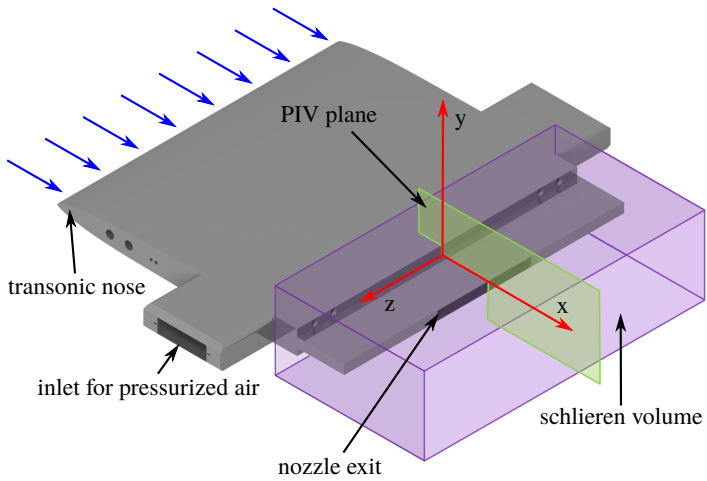


Figure 7.7: Illustration of the planar space launcher model with a 2D TOC nozzle and the measurement locations for PIV and schlieren

7.3.2 Test cases

An overview of the experimental free-stream conditions for the TOC nozzle experiments is provided in table 7.2. The \pm values in the table indicate the standard deviation of each quantity during the measurements. The measurement uncertainty is within $\pm 1\%$.

Table 7.2: Free-stream flow conditions of TWM for the experiments under investigation

Ma_∞	p_0 [bar]	p_∞ [bar]	T_0 [K]	U_∞ [$\frac{m}{s}$]
0.80 ± 0.0008	1.30 ± 0.0013	0.852 ± 0.0008	291 ± 1.2	259
2.00 ± 0.0010	2.50 ± 0.0022	0.320 ± 0.0004	292 ± 1.6	509

7.3.3 Particle image velocimetry

The PIV setup described in chapter 4.2.2 was used for the two-dimensional velocity field measurements. For each test case, 500 double images were recorded. The time separation between an image pair was $1.6 \mu s$ and $0.8 \mu s$ for $Ma_\infty = 0.80$ and $Ma_\infty = 2.00$ respectively. For data processing, the same pre-processing, evaluation methods, and post-processing steps were applied as described in chapter 4.2.2. During the PIV evaluation the final interrogation window size was reduced to 12×12 pixel with 50 percent overlap, yielding a vector grid spacing of $285 \mu m$. An approximate illustration of the FOV is provided in figure 7.7.

7.3.4 Schlieren measurements

For further analyses regarding the transitional behavior of the nozzle, the four color schlieren system described in chapter 4.2.3 was used. An illustration of the measurement volume is provided in figure 7.7. The images were recorded at a frame rate of 20kHz.

7.4 Integration and validation of the nozzle model in the TWM

7.4.1 Nozzle flow and seeding

Once the nozzle model had been designed and manufactured, the model had to be integrated into the TWM and the predictions of CFD had to be validated. After the model was successfully fitted into the TWM's test section, its stand-alone seeding system was tested. The goal was to achieve a homogeneous seeding distribution within the nozzle flow, and a similar particle density to the external flow. Figure 7.8 at the top left shows a raw image with its intensity distribution. This visualizes the particles in the flow. The particle image

densities are very similar for the external and the nozzle flow, besides the region downstream of the overexpansion shock from the jet plume. The particle images in the nozzle flow look bigger, which is due to the optical distortion generated by the large density difference. This however, did not affect the PIV processing's correlations for the calculation of the vectors, since the given change in the particle image diameters of these measurements cause an RMS uncertainty change of about a tenth of a pixel in the cross-correlation (Raffel et al. 2018). Figure 7.8 on the right shows an instantaneous vector field of the nozzle flow with an external flow at $Ma_\infty = 0.80$. It can be seen that the nozzle is fully flowing, meaning that there is no flow separation inside the nozzle.

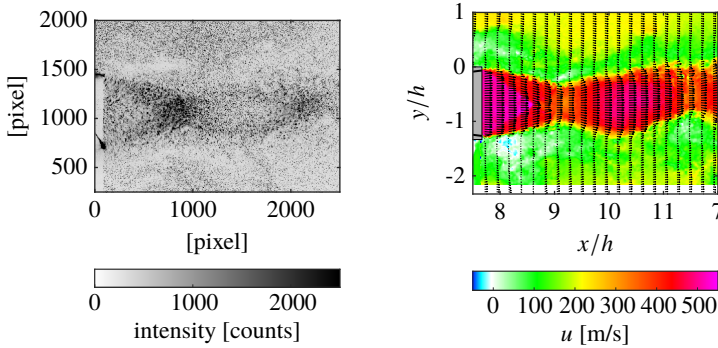


Figure 7.8: Left: Raw PIV image with seeding in the external and nozzle flow at $Ma_\infty = 0.80$. Right: Streamwise component of the vector field calculated from the raw PIV image.

7.4.2 Interaction between a nozzle flow and transonic external flow

The presence of the jet plume has an effect on the length of the recirculation region. This validates the results of Depres et al. (2004) on a planar model. At $Ma_\infty = 0.80$, even without a nozzle flow, the mean reattachment length of the shear layer on the nozzle fairing decreased to $x/h = 5.45$ (refer to figure 7.9 at the top), compared to $x/h = 6$ with the long splitter plate analyzed in chapter 5. This small difference is most likely caused by the low-pressure area developing in the cavity of the TOC nozzle, creating a favorable pressure gradient for an earlier reattachment. When the nozzle is in operation, the mean reattachment further decreases to $x/h = 5.15$ (refer to figure 7.9 at the bottom), showing an apparent effect of the jet plume. This is also due to a favorable pressure gradient created by the overexpanded nozzle flow, which is characterized by a low-pressure region at the nozzle's exit.

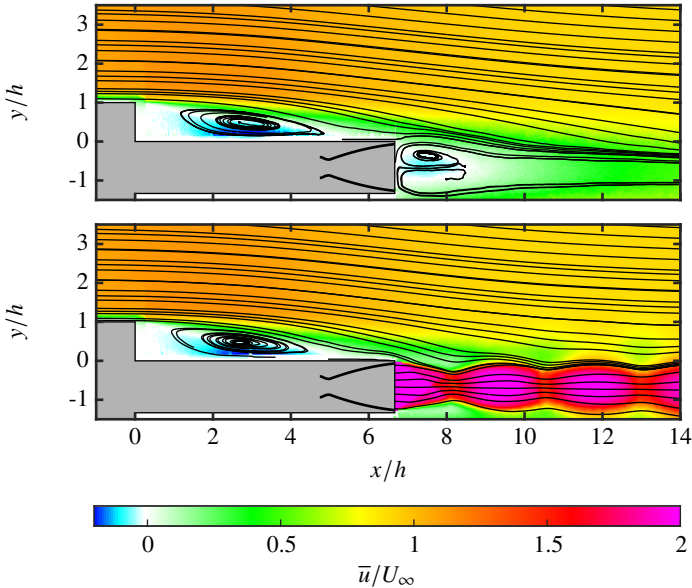


Figure 7.9: Illustration of the streamwise component of the mean flow field at $Ma_\infty = 0.80$ without a jet plume at the top, and with a jet plume at the bottom

The compressible effects of the overexpanded nozzle flow can also be seen in the schlieren recording in figure 7.10 at the same flow conditions. The overexpansion of the nozzle flow is clearly visible in the mean vector field and the schlieren image, since the plume's flow

moves towards the symmetry plane from the nozzle' lip.

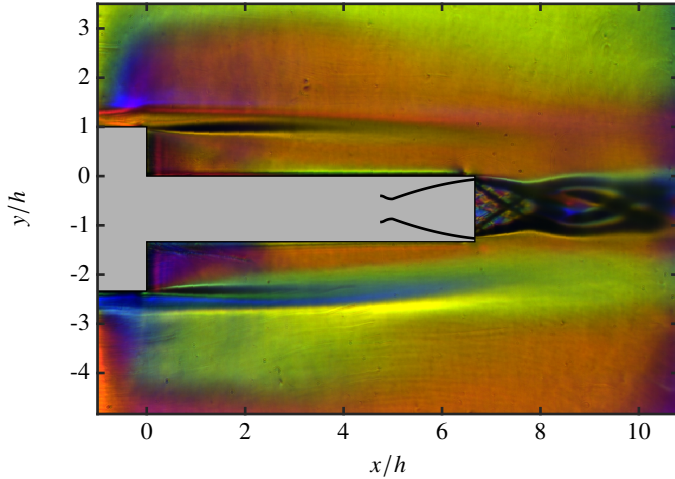


Figure 7.10: Schlieren shadowgraph at $Ma_\infty = 0.80$ with the jet plume in operation. The overexpansion of the nozzle is clearly visible through the presence of the characteristic overexpansion shocks stemming off the nozzle's lip.

The presence of the jet plume has negligible effects on the distribution of Reynolds shear stresses above the nozzle fairing. Figure 7.11 visualizes how the intensities remain on the same level, while the spatial distribution remains nearly identical as visualized by the contour lines of constant intensity. When the nozzle is in operation, the shear stresses in the first compression part of the shock train right behind the nozzle exit are very low. Thus, the jet plume has very little motion into the vertical direction, indicating a high stability of the jet plume. Since the Reynolds shear stress distribution upstream of the nozzle exit is nearly identical with and without the plume, it can be inferred that the presence of an overexpanded jet plume does not dynamically interact with the shear layer significantly.

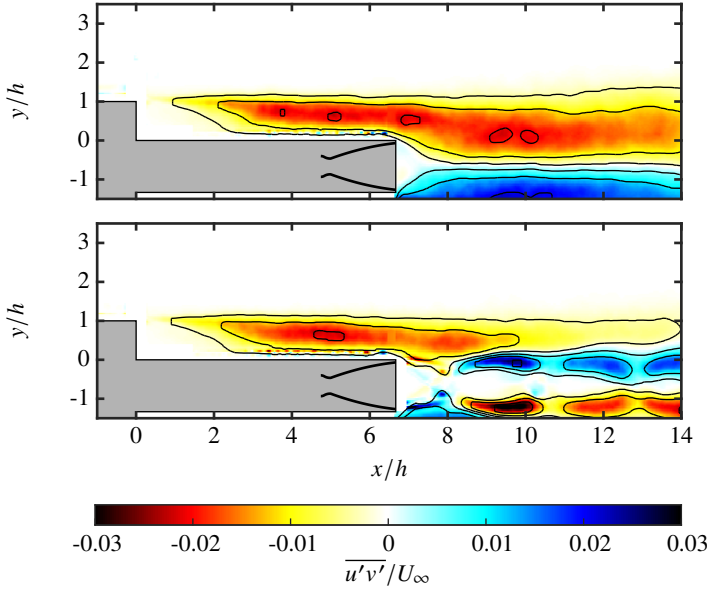


Figure 7.11: Distribution of the Reynolds shear stresses at $Ma_\infty = 0.80$ without a jet plume at the top, and with a jet plume at the bottom. Contour lines indicate $\overline{u'v'}/U_\infty^2 = \pm 0.003, \pm 0.01, \pm 0.02$ towards the center.

In order to study the effect of the shear layer on the jet plume, a two-point correlation of the fluctuating velocity component v' was carried out, similar to the correlations in chapter 5. Figure 7.12 provides the two-point correlation in the FOV, correlated at the location indicated by the +. With the presence of the jet plume, the same structures that characterize the step mode are visible in the two-point velocity correlation. This looks very similar to the structures found by the pressure-velocity correlation in chapter 5.3.4 without the jet plume. Within the jet plume, there is no apparent correlation to the rest of the FOV. Therefore it can be summarized that in the transonic regime the effect of a jet plume on main dynamic mechanisms of the shear layer is negligible. Vice versa, the shear layer does not cause nozzle instability or separation issues, even at a low $sNPR$.

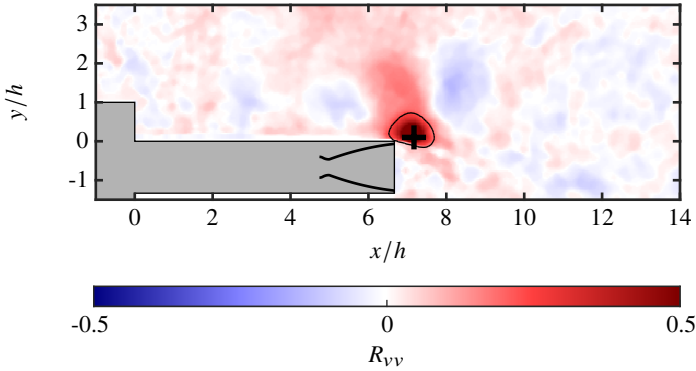


Figure 7.12: Two-point correlation of v' at $Ma_\infty = 0.80$ with a jet plume. The + sign indicates the location that is correlated to the rest of the FOV. Contour lines indicate $R = \pm 0.2$.

7.4.3 Interaction between a nozzle flow and a supersonic external flow

In supersonic free-stream conditions the nozzle flow is slightly underexpanded as can be seen in figure 7.13 and in figure 7.14. Therefore, nozzle flow separation is not a concern in this flight regime. The mean flow fields above the nozzle fairing are very similar with and without the jet plume. Since the external flow is supersonic, an upstream effect of the jet plume could only be possible through the subsonic portion of the boundary layer. Therefore the jet plume has negligible effects on the external flow in this flight regime. One should note that a more extreme underexpansion could prevent the shear layer from the BFS reattaching onto the nozzle fairing. This common condition on launchers is then comparable to a cavity flow.

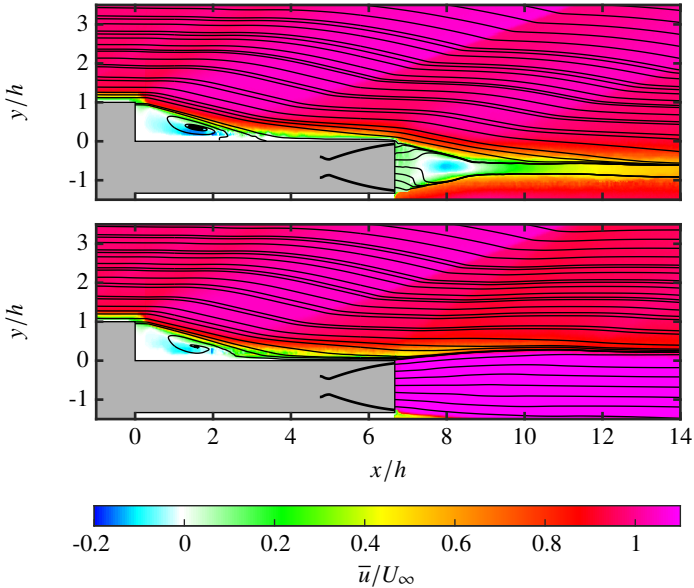


Figure 7.13: Illustration of the streamwise component of the mean flow field at $Ma_\infty = 2.00$ without a jet plume at the top, and with a jet plume at the bottom

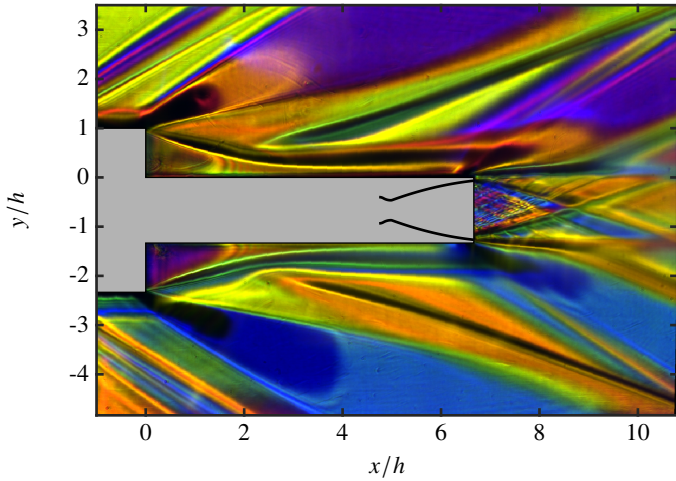


Figure 7.14: Schlieren shadowgraph at $Ma_\infty = 2.00$ with the jet plume in operation. The underexpansion of the nozzle is clearly visible through the presence of the expansion waves surrounding the triangular jet plume core.

The change in the distribution of the Reynolds shear stresses with the presence of the jet plume is negligible (refer to figure 7.15). In its underexpanded condition, the jet plume has no statistical fluctuations up to the end of the FOV. This was also observed when looking at successive single snap shots of the high-frequency schlieren recordings. This result is to be expected, as underexpanded nozzles provide higher plume stability.

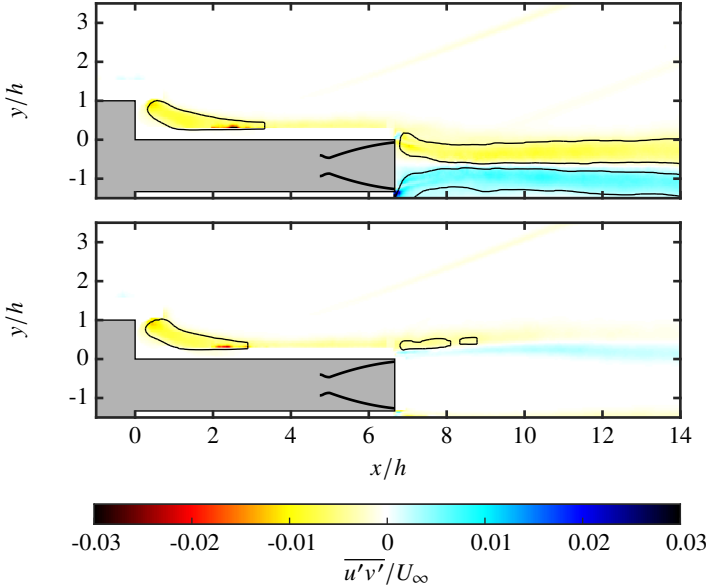


Figure 7.15: Distribution of the Reynolds shear stresses at $Ma_\infty = 2.00$ without a jet plume at the top, and with a jet plume at the bottom. Contour lines indicate $\overline{u'v'}/U_\infty^2 = \pm 0.003$.

The two-point correlations in figure 7.16 is similar to the correlation in chapter 5.3.4 above the nozzle fairing. When considering the jet plume as well, some of the shock-like structures of the external flow and the nozzle flow correlate with each other. This means that there is a slight interaction of the shocks' movement around the nozzle's lip. However, this does not result in any apparent negative effects anywhere in the FOV.

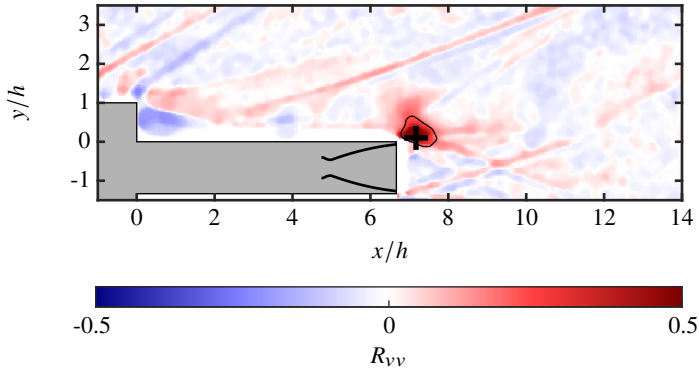


Figure 7.16: Two-point correlation of v' at $Ma_\infty = 0.80$ with a jet plume. The + sign indicates the location that is correlated to the rest of the FOV. Contour lines indicate $R = \pm 0.2$.

7.5 Summary & conclusions on the TOC nozzle model

This chapter outlined the design and integration of a planar space launcher model with a cold-gas nozzle. The predictions of the digital design phase were sufficient, since the model behaved as desired. The only unforeseen effect was that the planar nozzle experienced slight plastic deformation, which permanently deformed its shape to something similar to the deformed nozzle illustrated in figure 7.6. For this reason it was decided to reduce the spanwise width of future nozzle models.

The overexpanded nozzle flow behaved exactly as predicted by CFD. It was possible to reach an overexpanded condition without nozzle flow separation at the design point. The presence of the transonic shear layer did not cause the overexpanded nozzle flow to separate. The results indicate that the nozzle flow does not have a dynamic effect on the shear layer. A two-point correlation also shows that the shear layer does interact with the jet plume close to the nozzle exit.

An underexpanded nozzle condition was also reached with a supersonic external flow. In this condition, a slight interaction between the shock movements of two flows was observed. However, the effect of this interaction in real flight conditions does not lead to nozzle flow separation.

Thus, it can be summarized that the interaction between the shear layer and a generic rocket nozzle flow is negligible for the design considerations of a space launcher similar to Ariane 5. This statement is only valid for nozzle fairings that are long enough for the shear layer to reattach on the fairing. [Depres et al. \(2004\)](#) showed that there is a clear interaction between a nozzle flow and a transonic shear layer for shorter fairings, where the shear layer reattaches onto the jet plume itself.

8 The feasibility of a Dual-Bell nozzle at relevant flight conditions

This chapter investigates the feasibility of a Dual-Bell nozzle when it is exposed to an external flow, such as would be encountered during the ascent of a space launcher. Due to the promising results that flow control can achieve with respect to buffeting, longer nozzle concepts for better trajectory performance could become feasible. Therefore, the TOC nozzle, outlined in chapter 7, is replaced by a so-called 'Dual-Bell' nozzle. The results show that strong interactions are present between the Dual-Bell nozzle's flow and the external flow when the nozzle is operating in its sea level mode. Finally, the transition behavior of the Dual-Bell nozzle from sea level to altitude mode is investigated. The results show that a natural transition of the Dual-Bell nozzle flow during supersonic flight is not favorable, as several retransitions occur. This leads to the concluding suggestion for a Dual-Bell nozzle to transition in the transonic regime, in order for it to be a feasible alternative to current nozzle concepts. This chapter is structured as follows:

- 8.1 Literature review of nozzle flow and Dual-Bell nozzles
- 8.2 Test cases and analysis methods
- 8.3 Detailed overview and discussion of the results of a Dual-Bell nozzle
- 8.4 Summary and conclusions of the gathered insights

Part of this chapter is published in [Bolgar et al. \(2019a\)](#)¹.

8.1 Literature review on Dual-Bell nozzles

In chapter 2 it was mentioned how the Vulcain 2's nozzle extension was shortened in order to avoid structural problems. This in turn reduces the expansion ratio of the nozzle defined as the exit area divided by the throat area of the nozzle ($\varepsilon = A_e/A^*$), decreasing the thrust over the trajectory of the Ariane 5. For a rocket engine the one-dimensional time-averaged thrust is defined as:

¹Reprinted by permission from Springer Nature Customer Service Center GmbH: Springer, Cham, [New Results in Numerical and Experimental Fluid Mechanics XII](#), *Experimental Analysis of the Interaction Between a Dual-Bell Nozzle with an External Flow Field Aft of a Backward-Facing Step*, Istvan Bolgar, Sven Scharnowski and Christian J. Kähler, © Springer Nature Switzerland AG, part of Springer Nature 2020.

$$F_N = \dot{m} u_e + A_e(p_e - p_\infty) \quad (8.1)$$

where \dot{m} is the mass flow rate, A stands for the area and subscript e denotes the exit of the nozzle. Figure 8.1 plots the thrust versus p_e/p_∞ . For a certain energy stored in a gas the highest thrust is reached when all of the energy is converted to kinetic energy and the potential energy does not contribute towards thrust. This is the case when the gas is expanded to the ambient pressure at the nozzle exit. This is also called an ideally or perfectly expanded nozzle, where $p_e/p_\infty = 1$. A nozzle on a space launcher only reaches this condition at one specific altitude in its trajectory. Figure 8.2 compares three nozzles' thrust with different expansion ratios as a function of the altitude. A low expansion ratio, or high p_e/p_∞ , provides the highest thrust integral below 8 km of altitude but has a disadvantage compared to higher expansion ratio nozzles for the remaining trajectory. In contrast, a high expansion ratio or low p_e/p_∞ nozzle has the best performance above 20 km of altitude, but has a significantly lower thrust integral below that.

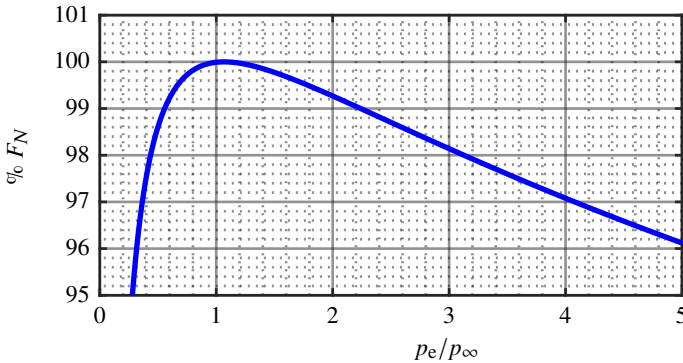


Figure 8.1: Thrust vs. p_e/p_∞

The application of the flow control solutions described in chapter 6 would allow Ariane 5 to use a longer nozzle extension due to the lower dynamics on the nozzle structure. This would decrease the thrust integral in the troposphere, however it would yield a significant thrust gain from the stratosphere onwards to about 200 km in altitude, where the main engine is shut down (refer to chapter 2.1). Regardless, an upper limit to the length of the nozzle extension still exists. For the Vulcain 2 this upper limit dictates that the nozzle must be fully flowing (no nozzle flow separation) in ground operation in order to avoid high side loads (Frey 2001) at takeoff. Therefore, another concept for a further increase in the thrust over the trajectory of a space launcher must be applied.

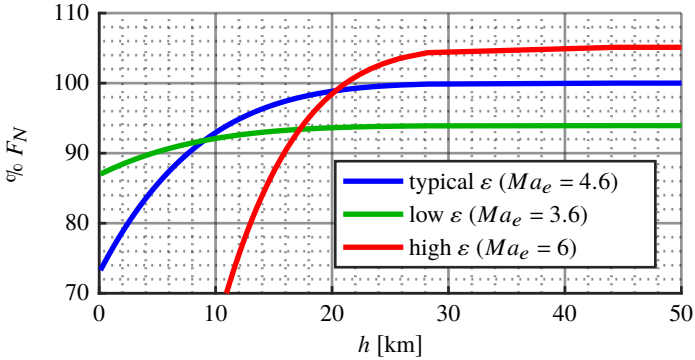


Figure 8.2: Thrust vs. altitude for different nozzle expansion ratios

An adaptive nozzle would be a feasible solution due to the fact that they provide a stable separation location along the nozzle contour. In order for the nozzle to be interchangeable on an existing space launcher system, the nozzle should be similar in its architecture to current internally flowing Bell nozzles. Without the need for additional actuators, the so-called 'Dual-Bell' nozzle, whose concept was first proposed by Foster & Cowles (1949), would be a viable alternative to currently used designs. The Dual-Bell contour is characteristic through its geometric discontinuity, or inflection, between the throat and the exit. This splits the nozzle into two separate bells, hence a Dual-Bell. The first Bell is termed the base and the second bell is termed the extension. A schematic is provided in figure 8.3.

In contrast to a conventional Bell nozzle, a Dual-Bell nozzle has two operating modes; the sea level mode and the altitude mode. In the sea level mode the flow expands into the base nozzle, where it separates at the contour inflection in a spatially and temporally steady manner (refer to the top part of figure 8.4). In this state, the nozzle is overexpanded, creating a low pressure jet plume and a favorable pressure gradient from the outside of the nozzle into the nozzle extension. However, even at takeoff the sea level mode's overexpansion is not as extreme as it is the case for a conventional rocket nozzle. This increases the thrust integral in the troposphere (refer to figure 8.2) while avoiding the risk of high side loads due to large separated flow regions during the start-up of the engine (Nürnberg-Génin & Stark 2009). As the launcher ascends and the pressure in the atmosphere decreases below a certain level, the flow naturally expands into the nozzle extension, filling it entirely (refer to the bottom part of figure 8.4). This operating state is defined as the altitude mode. In the altitude mode, the flow expands to a much lower pressure than with a conventional nozzle, leading to a comparatively increased thrust from the stratosphere to the main engine's shutdown

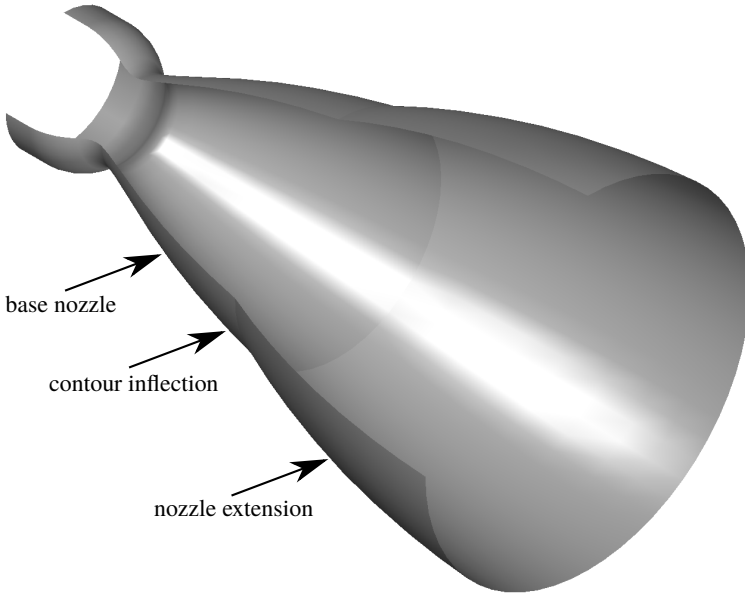


Figure 8.3: Illustration of a Dual-Bell nozzle

(refer to figure 8.2). The recently published work of [Stark et al. \(2016\)](#) showed how an Ariane 5 could expect a 490kg, or approximately 5%, increase in its payload on a typical GTO mission with a change of its conventional nozzle to a Dual-Bell. This can be deduced qualitatively from figure 8.2, when combining the thrust curves of the low ε and the high ε extensions in figure 8.2 to obtain a Dual-Bell's performance. The optimal transition point would be at an altitude of approximately 17 km, where the two curves intersect. However, the natural transition point is dependent on many geometrical parameters of the nozzle.

[Horn & Fisher \(1993\)](#) investigated various contour profiles of the second divergent section of Dual-Bell nozzles. The extensions included a conical contour, a Rao contour ([Rao 1958](#)), a constant pressure contour, and an overturned positive pressure gradient contour. All of the contours had identical expansion ratios. The transition stability proved to be a function of the pressure gradient about the contour inflection. A highly favorable pressure gradient about the inflection provides for the quickest and most repeatable transition. This was achieved with the overturned contour, which extremely expands the flow about the inflection point prior to compressing it again. The drawback of this type of contour is that the thrust comparatively decreases due to the non-optimal contour. Therefore, the

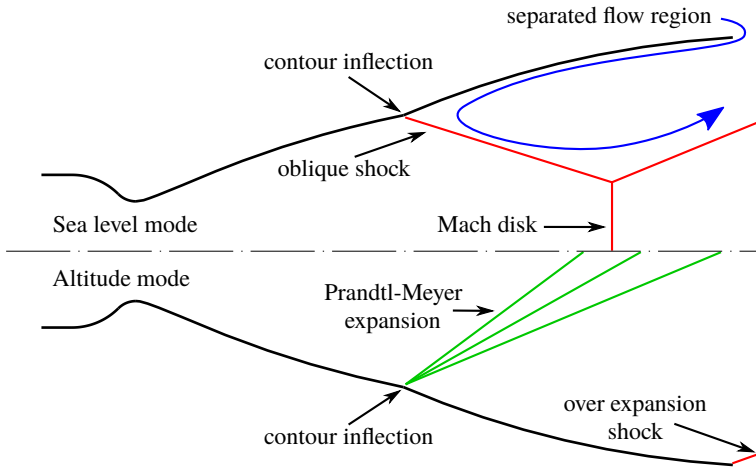


Figure 8.4: Sketch of the two Dual-Bell operating modes: Sea level mode is illustrated above the axis of symmetry. Altitude mode is illustrated below the axis of symmetry.

constant pressure extension, which keeps a constant pressure along the nozzle wall while gradually turning the flow axially, was considered the best trade-off. This contour provided repeatable transitions below 30ms, while nearly matching the thrust coefficient of a TOC with the same expansion ratio. Next to this, [Horn & Fisher](#) stated that the low-pressure recirculation region present during sea level mode causes an early transition, since this pressure is below ambient conditions. Additionally, this causes aspiration drag, which has to be taken into account when evaluating the thrust performance of a Dual-Bell nozzle over the mission's trajectory.

Following [Horn & Fisher's](#) results, the Dual-Bell concept started to receive serious consideration from Germany. [Immich & Caporicci \(1996\)](#) compared the performance of a generic nozzle to a Dual-Bell for a polar mission. Both nozzles were optimized using the ALTOS trajectory optimization software ([Buhl et al. 1992](#)). The Dual-Bell nozzle yielded a 33% payload increase over the generic nozzle. Thus, the performance advantage of this type of nozzle is significant, but its application can only be feasible if the transition event happens predictably.

For this reason the research interest in the transition event of Dual-Bell nozzles increased from the late 20th century. [Frey & Hagemann \(1999\)](#) critically assessed the effect of the overall contour of a Dual-Bell on the transition and conducted a parametric study on the performance. The assessment was based on analytical solutions and empirical data from conventional Bell nozzles. With respect to the transition, the conclusions were similar to

those of [Horn & Fisher](#), stating that a constant pressure or overturned contour would be the most advantageous. Using [Schmucker](#)'s separation criterion, it was shown that the side loads of the constant pressure contour would be high, however the transition would be so quick that side loads may not even play a role. The performance evaluation showed that the vacuum thrust of Dual-Bell contours suffer minor deficits, on the order of 1%, compared to an optimal Bell contour with the same expansion ratio. In sea level operation the performance deficit was less than 3% due to aspiration drag. This value is linearly dependent on the ambient pressure and therefore decreases with increasing altitude.

Consequently, [Hagemann et al. \(2002\)](#) conducted complementary experimental investigations based on [Frey & Hagemann](#)'s findings. The results confirmed the analytical predictions, showing that the constant pressure and the overturned extensions require short time scales of around 10ms for a complete transition. In addition, a strong hysteresis was observed with these contours, meaning that a retransitioning back to sea level mode would require a much higher ambient back pressure than the initial transition event. This is an important criterion for the feasibility of a Dual-Bell nozzle, as multiple 'flip-flops' between the modes would cause excessive side loads.

In the aftermath of these continuously positive results, the German Aerospace Center (DLR) carried out multiple investigations on transitioning, trying to characterize the most influential parameters for a controlled event with minimal side loads. For example [Nürnberg-Génin & Stark \(2009, 2010\)](#) investigated the influence of the length of the extension on the transition. Next to determining the transition nozzle pressure ratio NPR_{tr} , they showed that a longer extension length provides for a more stable and faster transition. The results also showed increasing hysteresis with increasing nozzle extension lengths. Furthermore, an intermediate state defined as sneak transition was found between the sea level and the altitude mode. This third mode is characterized by a stable separation shortly after the inflection and only occurs for certain wall contours.

The problematic of side loads during transition was also given attention by [Génin & Stark \(2011\)](#). The results showed that a Dual-Bell nozzle has lower side loads than a TIC nozzle during steady operation in either of its operating modes. During transition however, a brief peak side load was observed, which was up to a factor of four higher than the peak side loads of a TIC nozzle.

A shortcoming of all previous work carried out on transition is that the transition is triggered by either an increase in the thrust chamber pressure or a decrease of the external pressure. This can be achieved numerically ([Martelli et al. 2007](#)) as well as experimentally in a high-altitude simulation chamber ([Verma et al. 2010](#)), for instance. Even though the transition event is triggered somewhat realistically, the interaction of the nozzle flow with the external flow is completely neglected. Investigations in the past have tried to compensate this by imposing external pressure fluctuations as a boundary condition either numerically ([Pergio et al. 2003](#)) or experimentally ([Verma et al. 2014](#)). Regardless, this neglects many effects from the oncoming flow, which may interact with the nozzle flow, ultimately leading to the flip-flop effect (refer to figure 8.5 for a graphical illustration). Therefore, the major

goal of this chapter is to characterize the interactions of an external flow with a Dual-Bell nozzle flow in its sea level mode, its altitude mode, and during transition.

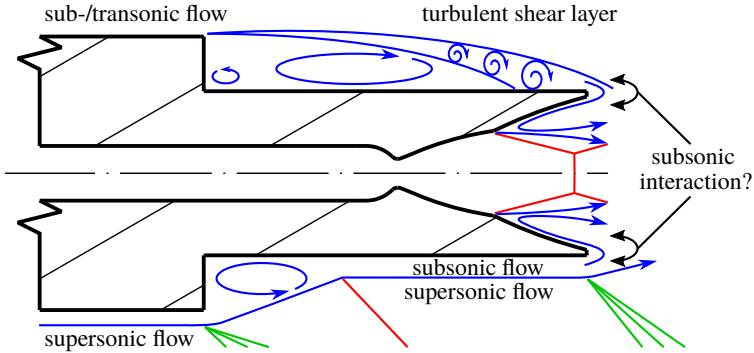


Figure 8.5: Possible interaction of a subsonic (above the axis of symmetry) or a supersonic (below the axis of symmetry) external flow with a Dual-Bell nozzle flow

8.2 Experimental setup

8.2.1 The Dual-Bell nozzle model

The Dual-Bell nozzle was integrated into the same forebody model as the TOC nozzle. However, the step's height has been decreased from 7.5 mm to 5 mm in order to allow for higher expansion ratios that Dual-Bell nozzles would provide on a space launcher. The splitter has a total length of 35 mm, or $7h$, allowing to keep the high dynamics of the shear layer close to the nozzle flow. At the center of the splitter plate with a height of 15 mm, a 2D Dual-Bell nozzle with a nozzle exit height of 14 mm spans 56 mm across the model. The nozzle contour was designed and provided by Chloé Génin from DLR Lampoldshausen. The base nozzle of the Dual-Bell is a truncated ideal contour (TIC), and the extension is constant pressure contour. The nozzle throat is 2.61 mm in height, giving it an expansion ratio of $\varepsilon = 5.36$, resulting in a design exit Mach number of 3.29. Based on its throat height, the nozzle has a Reynolds number of $Re^* = 230,000$ at $p_{n,0} = 6$ bar. The nozzle was designed to transition at $NPR_{tr} = 17.2$. Figure 8.6 illustrates the Dual-Bell nozzle model. Table 8.1 provides the boundary conditions of the nozzle for the underlying experiments.

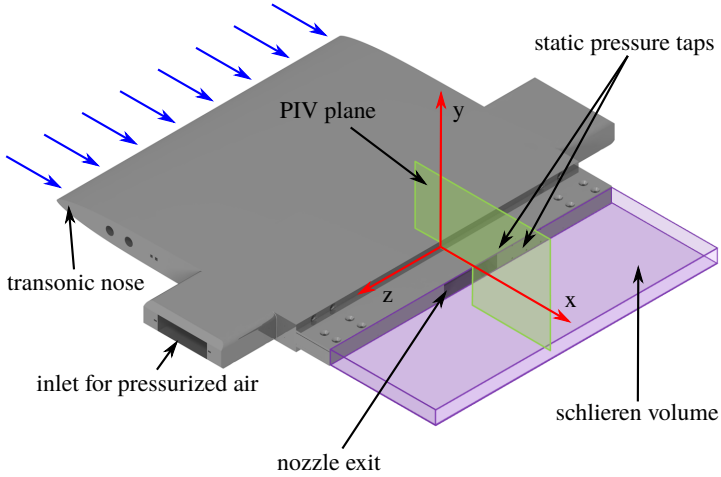


Figure 8.6: Illustration of the planar space launcher model with a 2D Dual-Bell nozzle and the measurement locations for PIV and schlieren

Table 8.1: Nozzle conditions for experiments under investigation

Ma_∞	$p_{n,0}$ [bar]	NPR
0.80	5.95 ± 0.05	≈ 7
1.60	3.95 ± 0.05	$\approx 4 - 4.7$
2.00	5.95 ± 0.05	≈ 18.75

8.2.2 Test cases

Table 8.2 provides an overview of the experimental free-stream conditions for the Dual-Bell nozzle measurements. The \pm values in the table indicate the standard deviation of each quantity during the measurements, while the measurement uncertainty is within $\pm 1\%$. In order to achieve transition of the nozzle at $Ma_\infty = 1.60$, the total pressure in the test section was linearly reduced from 4.3 bar to 3.6 bar in 4 s while keeping the thrust chamber pressure constant at 4 bar.

Table 8.2: Free-stream flow conditions of TWM for the experiments under investigation

Ma_∞	p_0 [bar]	p_∞ [bar]	T_0 [K]	U_∞ [$\frac{m}{s}$]
0.80 ± 0.0008	1.30 ± 0.0013	0.852 ± 0.0008	291 ± 1.2	259
1.60 ± 0.0050	4.3 to 3.6 in 4 s	1.01 to 0.85 in 4 s	292 ± 1.5	446
2.00 ± 0.0010	2.50 ± 0.0022	0.320 ± 0.0004	292 ± 1.6	509

8.2.3 Particle image velocimetry

The PIV setup described in chapter 4.2.2 was used for the two-dimensional velocity field measurements. For each test case 500 double images were recorded. The time separation between an image pair was $1.6 \mu s$ and $0.8 \mu s$ for $Ma_\infty = 0.80$ and $Ma_\infty = 2.00$ respectively. For data processing, the same pre-processing, evaluation methods, and post-processing steps were applied as described in chapter 4.2.2. During the PIV evaluation the final interrogation window size was reduced to 12×12 pixel with 50 percent overlap, yielding a vector grid spacing of $285 \mu m$. An approximate illustration of the FOV is provided in figure 8.6.

8.2.4 Schlieren measurements

For further analyses regarding the transitional behavior of the nozzle, the four color schlieren system described in chapter 4.2.3 was used. An illustration of the measurement volume is provided in figure 8.6. The images were recorded at a frame rate of 20kHz.

8.3 Results of the Dual-Bell nozzle

8.3.1 Nozzle mode prediction with CFD

Prior to the wind tunnel experiments, the Dual-Bell nozzle flow was investigated with 2D CFD in order to get a better understanding of the effect of an external flow on the Dual-Bell's

flow mode. The solver and the discretized domain were set up identical to the one in chapter 7.2.2. The boundary conditions were slightly altered in order to reach either sea level or altitude mode. This was simulated without an external flow, a transonic external flow set at $Ma_\infty = 0.80$, and a supersonic external flow set at $Ma_\infty = 2.00$. The total pressure at the nozzle inlet boundary was kept at 6 bar for each simulation. The total temperature in the entire domain was set at 288 K. As mentioned in chapter 8.2.1, the transition should occur at $NPR_{tr} = 17.2$. A detailed overview of the boundary conditions is provided in table 8.3.

Table 8.3: Flow conditions for the CFD simulations

External flow	desired mode	Ma_∞	p_∞ [bar]	NPR
off	sea level	–	0.4	15
	altitude	–	0.3	20
transonic	sea level	0.80	0.4	15
	altitude	0.80	0.3	20
supersonic	sea level	≈ 2	1.2	5
	altitude	≈ 2	0.6	10

Without an external flow, the results in figure 8.7 at the top show that if $NPR < NPR_{tr}$, the flow separates at the inflection point as predicted. In its sea level mode, the nozzle base has a fully attached flow along the nozzle contour. The mean pressure distribution above the symmetry plane has a pressure minimum at the inflection point, while below the symmetry plane the maximum velocity characteristic stems off of the inflection point at an angle downstream towards the symmetry plane. Past the inflection point the negative streamwise velocities close to the nozzle wall clearly indicate a reverse flow region in the nozzle extension.

When $NPR > NPR_{tr}$ at the bottom of figure 8.7, the nozzle flow transitions into altitude mode as predicted. The low-pressure region above the symmetry plane fills the entire nozzle extension, allowing the flow to accelerate to around 630 m/s at the nozzle exit, illustrated below the symmetry plane. The flow is fully attached along the contour of the extension, besides a small region close to the exit. A small separation region at the nozzle exit is very common in RANS simulations, and can therefore be neglected. Hence, it can be summarized, that without an external flow the nozzle contour behaves as predicted.

The addition of a transonic external flow along the nozzle fairing in figure 8.8 has no drastic influence on the behavior of the Dual-Bell nozzle. When $NPR < NPR_{tr}$ at the top of this figure, the nozzle is in sea level mode with very similar mean pressure and mean velocity distributions within the nozzle, as it is the case without an external flow. As soon

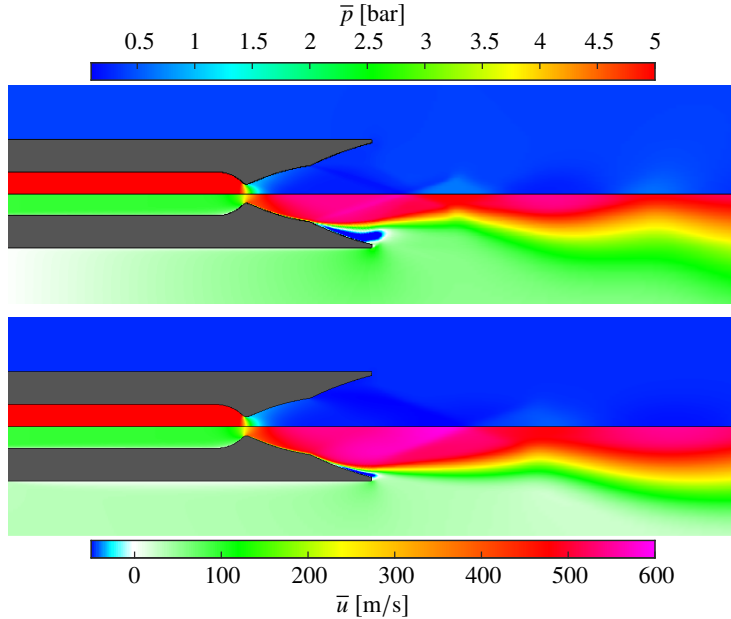


Figure 8.7: 2D CFD analysis of the final Dual-Bell nozzle without an external flow. Top: $NPR = 15$. Bottom: $NPR = 20$. The upper symmetry halves of each case indicate the mean static pressure distribution. The lower symmetry halves of each case indicate the mean streamwise velocity distribution.

as $NPR > NPR_{tr}$, which is illustrated at the bottom of this figure, the nozzle transitions into its altitude mode. Again, the pressure and velocity distributions within the nozzle are very similar to those of the case without an external flow. Note that the small reverse flow region close to the nozzle exit completely disappears with the presence of the external flow. This is caused by an expanding flow about the nozzle lip, which results in a slight decrease of the external pressure in the vicinity of the jet plume. Overall, the addition of a transonic external flow on a flat plate has no significant influence on the Dual-Bell's behavior. The effect of the BFS was intentionally neglected, since a 2D RANS simulation cannot replicate the dynamics of such a flow.

The TWM inlet boundary of the domain was set to $Ma_\infty \approx 2$ for the simulation shown in figure 8.9. Initially, the entire TWM inlet boundary was set at $Ma_\infty = 2.00$ with a constant velocity distribution on the boundary. This however, led to the formation of oblique shocks

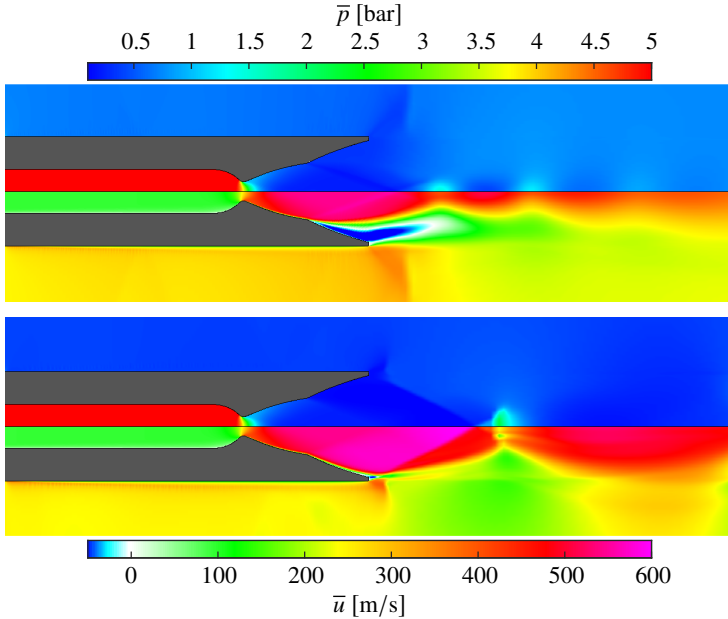


Figure 8.8: 2D CFD analysis of the final Dual-Bell nozzle with an external flow at $Ma_\infty = 0.80$. Top: $NPR = 15$. Bottom: $NPR = 20$. The upper symmetry halves of each case indicate the mean static pressure distribution. The lower symmetry halves of each case indicate the mean streamwise velocity distribution.

on the wall boundaries of the nozzle fairing and the TWM test section wall, starting directly at the TWM inlet boundary. This is due to the build up of a boundary layer, which deflects the streamlines and slightly changes the flow direction concavely close to the wall. When a flow is supersonic, a concave flow direction change can only occur across an oblique shock.

Therefore it was decided to input a supersonic velocity profile, which already included a boundary layer, at the TWM's inlet boundary. The velocity profile was extracted from the $Ma_\infty = 2.00$ PIV data described in chapter 5.3. The extraction took place at a location one step height downstream of the mean reattachment. This profile was mirrored to put an initial boundary layer onto the TWM wall in the CFD simulation as well. This method was able to avoid the formation of oblique shocks at the TWM's inlet boundary.

When looking at the result of the simulation with a supersonic external flow in figure 8.9, one can see that the nozzle is in its altitude mode, even though $NPR \ll NPR_{tr}$. An NPR of 5 was chosen, trying to model the sea level mode. However, a Prandtl-Meyer (PM)

expansion around the nozzle's lip leads to a significant decrease in the external pressure in the vicinity of the nozzle exit. Thus, with a supersonic external flow, NPR must not be defined as $NPR = p_{n,0}/p_\infty$, but rather by:

$$NPR_{\text{eff}} = p_{n,0}/p_{PM} \quad (8.2)$$

where p_{PM} signifies the static pressure downstream of the completed Prandtl-Meyer expansion process. The large change in static pressure acting upon the jet plume will be further elaborated on in chapter 8.3.3. When calculating the NPR_{eff} in both cases of figure 8.9, it yields values where $NPR_{\text{eff}} > NPR_{\text{tr}}$. Therefore, it can be summarized that in supersonic conditions transition occurs significantly sooner than predicted. On a real launcher, the travel through the sound barrier could potentially trigger a natural transition of the nozzle flow.

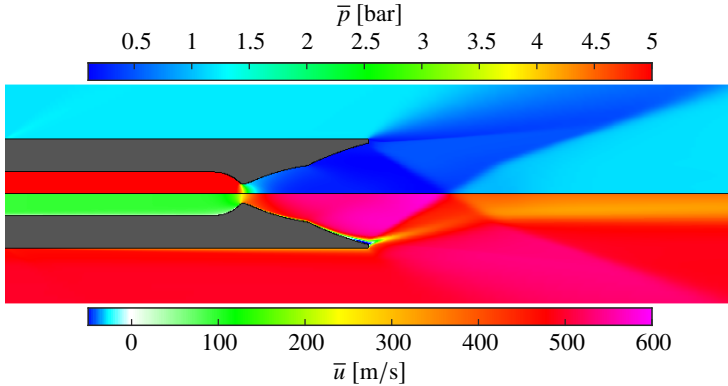


Figure 8.9: 2D CFD analysis of the final Dual-Bell nozzle with an external flow at $Ma_\infty \approx 2$ with $NPR = 5$. The upper symmetry half of indicates the mean static pressure distribution. The lower symmetry half indicates the mean streamwise velocity distribution.

Overall, the results of these simulations show that the nozzle should behave as predicted by DLR Lampoldshausen. Since the nozzle was initially designed for transition to occur during supersonic flight at $Ma_\infty = 2$, the nozzle is inherently limited to sea level mode only in transonic conditions in the experimental test facility. The CFD results confirm that altitude mode should not be possible in the TWM at transonic conditions. In supersonic conditions however, the sea level mode cannot be reproduced experimentally, unless the nozzle's total pressure is decreased and the free-stream Mach number is decreased to achieve higher static free-stream pressures. This is due to the limitations in the total pressure of the

measurement facility. For this reason, the total pressure in the nozzle and the free-stream Mach number were decreased in the experiments until transition was achieved. Due to the reflection of the shock stemming off of the model's nose from the wind tunnel walls, the lower limit in the free-stream Mach number for the shock to reflect past the end of the model is around 1.4 – 1.5. Therefore, the free-stream Mach number was reduced to $Ma_\infty = 1.60$. The total pressure in the nozzle was reduced to $p_{n,0} = 4$ bar, which allowed for transition to occur around a free-stream total pressure of $p_0 = 4$ bar. This is outlined in chapter 8.3.4.

8.3.2 Experiments in sea level mode

With the presence of the Dual-Bell nozzle and the reduced step height to 5 mm, the transonic flow field aft of the BFS is still similar in shape and its statistics to the ones in the previous chapters (refer to figure 8.10). At $Ma_\infty = 0.80$ and at $NPR = 4.7$ in figure 8.10, one can see that a reverse flow region develops in the second extension of the nozzle. This is to be expected, as the second extension of the bell has separated flow by definition in the sea level mode. Streamlines from the external flow extend into the nozzle, indicating that an interaction may be present. However, at this NPR there is a chance that the base nozzle is not fully flowing yet.

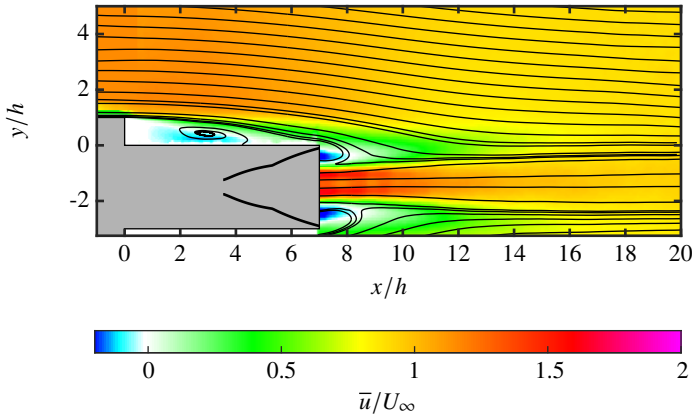


Figure 8.10: Illustration of the streamwise component of the mean flow field at $Ma_\infty = 0.80$ with $NPR = 4.7$

In order to investigate this further, the NPR was increased to 7. A similar result can be observed in the mean flow field in figure 8.11. However, a big difference in the shape of the jet plume can be observed. At this NPR it can now be assumed that flow in the base nozzle is fully established without separation. At $Ma_\infty = 0.80$, the acceleration about the BFS

decreases the free-stream's static pressure by 7%. A further reduction of the free-stream pressure occurs about the nozzle's lip, decreasing the static pressure by 8.8% compared to the free-stream's static pressure. This yields an increase in the effective NPR from $NPR = 7$ to $NPR_{\text{eff}} = 7.7$.

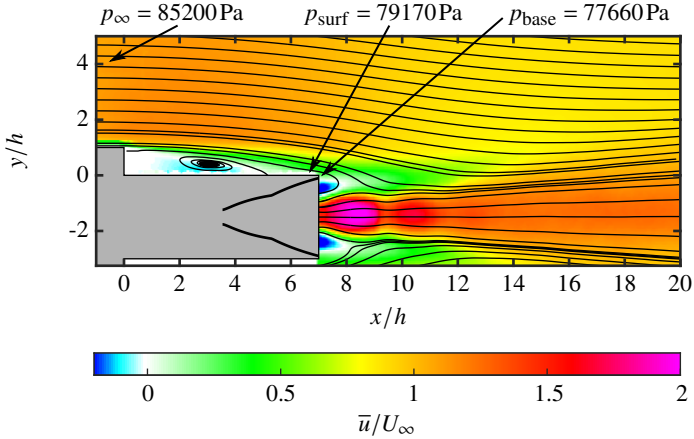


Figure 8.11: Illustration of the streamwise component of the mean flow field at $Ma_\infty = 0.80$ with $NPR = 7$ or $NPR_{\text{eff}} = 7.7$

For a more detailed statistical analysis, the fluctuating component of the vertical velocity scalar v' at a location close to the nozzle exit indicated by the + sign was correlated with itself in the entire 2D FOV. Figure 8.12 shows the resulting correlation in the 2D FOV, where strong correlations and anti-correlations are present throughout the entire flow field. Thus, a strong interaction is present at the nozzle exit with the rest of the flow field. The correlations are noticeably periodically organized and aligned with an angle and shape that closely resembles shocks. This is a significant contrast to the two-point correlation of the TOC nozzle in figure 7.12, where the correlation resembled the Kelvin-Helmholtz structures from the BFS, whereas the nozzle flow did not correlate with the external flow. Therefore, the shock-like structures present with the Dual-Bell nozzle were searched for in the instantaneous vector fields in the next step.

A set of two instantaneous vector fields at the previously described experimental conditions is shown in figure 8.13. The shock-like structures are present in the temporal snap shots as well. The way that these waves are developing after one another, as well as their shape and angle, very closely resemble that what has been defined to be nozzle screeching in literature (Panda 1998, Alkislar et al. 2003). Nozzle screeching has mostly

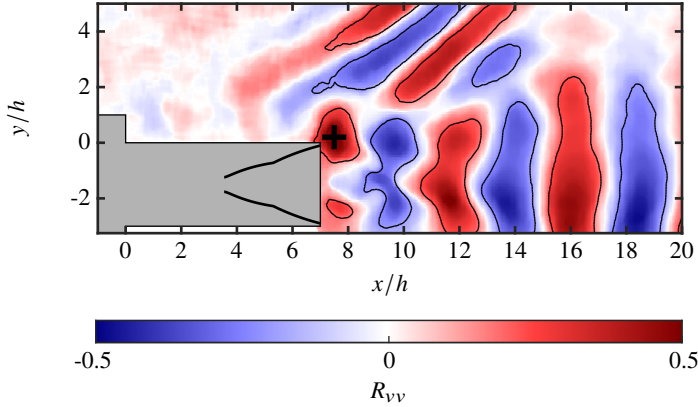


Figure 8.12: Illustration of a two-point correlation of v' at $Ma_\infty = 0.80$ with $NPR = 7$. The + sign indicates the location that is correlated to the rest of the FOV. Contour lines indicate $R = \pm 0.2$.

been observed in nozzle flows without an external flow or at subsonic external conditions. At that point, screeching can be seen in schlieren photographs as weak acoustic sound waves. However, the underlying results show that when an external flow close to sonic conditions is superimposed on these sound waves, the combination leads to shocks at velocities of $U = 250$ m/s, even though the speed of sound is around $c \approx 320$ m/s.

The frequency of these periodic shocks can be estimated by calculating the relative Mach number of the superimposed flows through the oblique shock wave theory (refer to the sketch in figure 8.14). This was done by approximating the sudden change in the flow direction across the shocks in an ensemble of vector fields. This yielded an average flow direction change of $\theta = 6.5^\circ$. The shock angle relative to the incoming flow is $\beta = 50^\circ$. By substituting these two values into the oblique shock wave theory equation for the shock angle, it is possible to calculate the Mach number ahead of the shock (Anderson 2007):

$$\tan \theta = 2 \cot \beta \frac{Ma^2 \sin^2 \beta - 1}{Ma^2 (\kappa + \cos 2\beta) + 2} \quad (8.3)$$

In this case, the weak solution of this equation yielded a relative Mach number of $Ma_{rel} \approx 1.5$, which is equivalent of a relative velocity of $U_{rel} \approx 480$ m/s when assuming the speed of sound from the physical reference frame stated above. Since the free-stream's flow velocity is around 250 m/s at that location, the shock moves upstream with the velocity difference of $|U|_{shock} = |U - U_{rel}| = 230$ m/s. Due to the small change in the flow direction, the magnitude of the streamwise velocity and its vector are nearly identical ($\cos \theta \approx 1$).

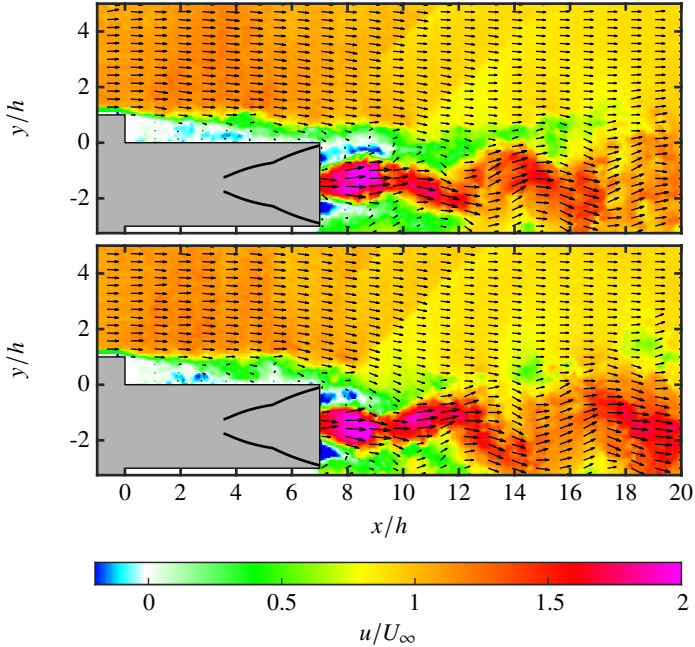


Figure 8.13: Illustration of the streamwise component of instantaneous vector fields at $Ma_\infty = 0.80$ with $NPR = 7$

Similarly, the average distance between shocks can also be approximated into the streamwise direction. This quantity was also extracted from the instantaneous vector fields, which is $d_{\text{shock}} = 0.018\text{m}$. Now, the screech frequency can be calculated by $f_s = U_{\text{shock}}/d_{\text{shock}} \approx 12,500\text{Hz}$. When considering the nozzle exit velocity and the height of the base nozzle at the contour inflection, the result yields a dimensionless screech frequency of $Sr_s \approx 0.3$. This is in good agreement with common screech frequencies for overexpanded jets (Rona & Zhang 2004, Singh & Chatterjee 2007). Even though other measurement methods would need to be utilized to determine a precise screech frequency, this rough estimation allows to identify the observed shock-like structures as screeching.

The formation of shocks as a result of screeching has not been reported in previous literature and could pose some complex structural difficulties for a space launcher. Another apparent phenomenon in the instantaneous vector fields in figure 8.13 is how the jet plume undergoes undulations with high amplitude deflections into the vertical direction. In other words, the jet plume is not as stable as it is the case with conventional nozzles used on

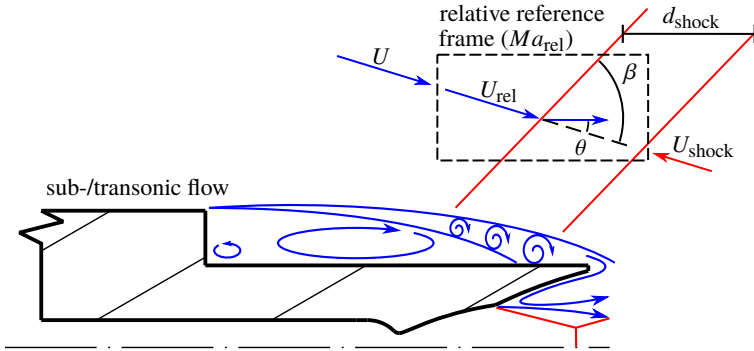


Figure 8.14: Graphical illustration of the calculation method of the screech frequency

common space launchers (refer to the results in chapter 7.4).

Combining the gathered insights from the instantaneous vector fields with the two-point correlation, certain assumptions about the interaction between the external flow and the nozzle flow, as well as screeching, can be made. The strong shock-like acoustical correlations seen around the nozzle systematically merge together with alternating Kelvin-Helmholtz structures. This can be seen in the proximity of the BFS between $x/h = 0 - 3$ in figure 8.12, as well as above the reattachment surface around $x/h = 5$. The structures close to these surfaces were identified to be instabilities caused by the step mode by [Bolgar et al. \(2018\)](#). According to the general knowledge of gas dynamics, the step mode should not be aware of screeching, due to the non-existing upstream cross-talk in supersonic flow, hence across shocks. Therefore, their coherent interaction should be limited. However, the seamless combination of the step mode structures with the screech shocks in the correlation image can be explained by the fact that the shear layer structures stemming off of the BFS influence the direction into which the nozzle flow is temporally deflected. This could be possible, if the generation of the step mode structures was shifted by half a phase between the upper and lower sides of the model. In other words, the vortices are being shed in an alternating sequence between the two sides. [Statnikov et al. \(2017\)](#) showed exactly this to be the case on an axisymmetric launcher model with an integrated nozzle. Thus, in the case of the current investigations, the presence of an alternating sequence of the step mode's vortices could lead to a periodic deflection of the jet plume. The deflection of the jet plume in turn creates the sound waves, or screeching, that are generated at a source further downstream. Therefore, the screech shocks also correlate with the upstream dynamics, since they're generation in time could be a direct effect of the BFS flow. Thus, a complex interaction between the nozzle flow and the external flow has been established. This causes an unstable jet plume when the Dual-Bell is in sea level mode. Further investigations have

to be carried out to see what conditions are conducive to screeching and to see whether the nozzle stability can trigger any negative effects that would make the thrust vectoring more difficult on a real space launcher, for example.

8.3.3 Experiments in altitude mode

In supersonic conditions a strong supersonic expansion occurs around the nozzle's lip. This drastically reduces the static pressure in the vicinity of the nozzle exit below ambient conditions, effectively increasing the NPR , which was emphasized in section 8.3.1 after having analyzed the CFD results. This static pressure can be referred to as p_{PM} denoting the influence of the Prandtl-Meyer expansion. Thus, during the design phase of a Dual-Bell nozzle the effective nozzle pressure ratio NPR_{eff} (refer to equation 8.2) has to be considered, in order for transition to occur at the desired condition, especially in supersonic flight conditions. The author of this work recognized this from preliminary CFD results in 2017, when he first introduced the corrected formulation of the nozzle pressure ratio (NPR_{eff}) in two consecutive internal project meetings (Bolgar & Kähler 2017a,b) with limited success amongst his peers. Back then it was concluded internally, that the existence of the extreme pressure reduction around the nozzle's lip would first have to be verified experimentally. The existence of this significant effect was verified experimentally by a project partner in 2018, who defined a so-called exit pressure ratio $EPR = p_{n,0}/p_{lip}$, where p_{lip} is the static pressure at the nozzle's lip (Barklage et al. 2018). Since EPR is a commonly used term in gas turbine technology to define the overall engine's pressure ratio, the author of this work will continue to use the notation of NPR_{eff} , which also reflects the chronological order of observation.

Figure 8.15 shows the mean flow field when the nozzle is in altitude mode, along with the static pressures present at the various locations. At $Ma_\infty = 2.00$, a Prandtl-Meyer expansion around the BFS, followed by a recompression shock at the reattachment surface decreases the free-stream's static pressure by 10%. Then, the previously noted Prandtl-Meyer expansion around the nozzle's lip drastically reduces the static pressure by 58% compared to the free-stream's static pressure. This makes $NPR_{eff} = 45.1$, which is more than twice as high as the regularly defined nozzle pressure ratio of $NPR = 18.8$. Figure 8.16 shows a comparison of NPR to NPR_{eff} at $Ma_\infty = 1.60$.

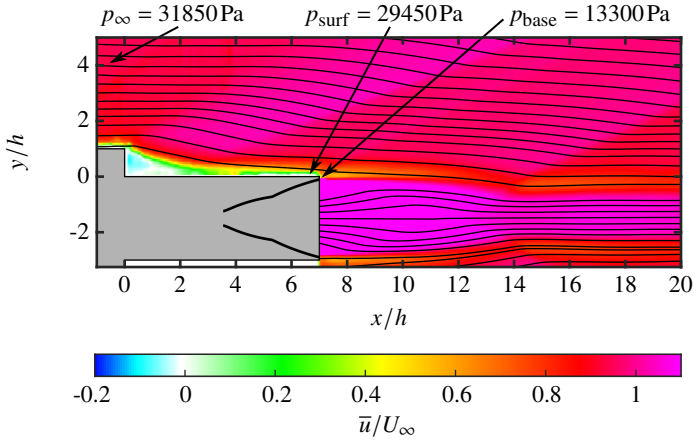


Figure 8.15: Illustration of the streamwise component of the mean flow field at $Ma_\infty = 2.00$ with $NPR = 18.8$ or $NPR_{\text{eff}} = 45.1$

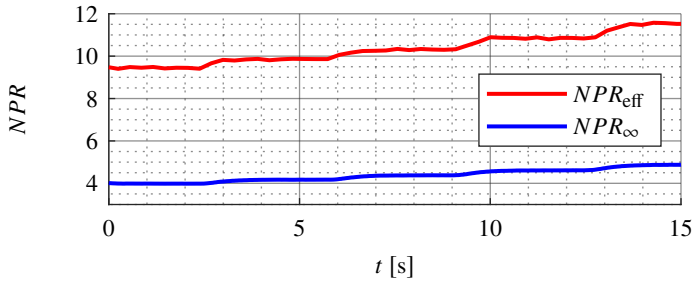


Figure 8.16: Comparison of NPR vs. NPR_{eff} when the total pressure in the TWM is decreased over time

In contrast to sea level mode, there is no apparent correlation between the nozzle and the external flow when correlating the fluctuating component of the vertical velocity scalar v' at a location close to the nozzle exit with the rest of the FOV (refer to figure 8.17). The correlation levels do not even reach the threshold for the contour lines of $R = \pm 0.2$, in contrast to the subsonic correlation in figure 8.12. Also, the dynamics of the nozzle, or the undulations, are not present when the nozzle operates in altitude mode. In other words, the strong interaction between the nozzle and the external flow only takes place during sea level mode, at least when transition is set to occur in supersonic conditions. Further investigations need to be carried out, to see whether an interaction would be present if the transition were to occur in transonic flight conditions.

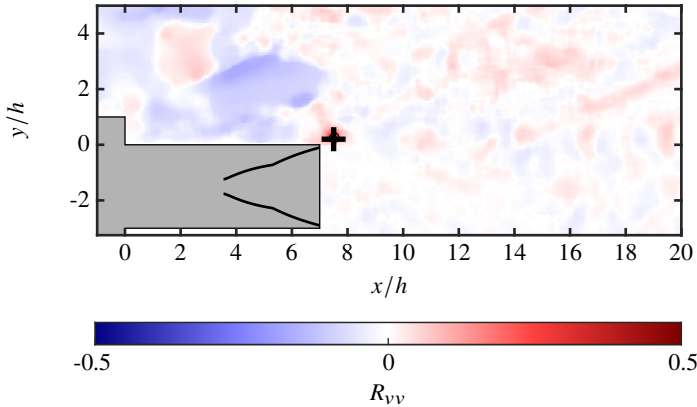


Figure 8.17: Illustration of a two-point correlation of v' at $Ma_\infty = 2.00$ with $NPR = 18.8$. The + sign indicates the location that is correlated to the rest of the FOV.

8.3.4 Experiments on transition

The transition from sea level to altitude mode occurs relatively sudden. Figure 8.18 shows the run time of the wind tunnel vs. a nozzle mode criterion, which was defined in the work frame of these experiments. The nozzle mode criterion evaluates the light intensity of each schlieren image in a defined evaluation window close to the nozzle exit (refer to white rectangle in the images of figure 8.19). As the average value of this evaluation window is usually close to either 0 or 1 (sea level or altitude mode, respectively) on a normalized scale, it gives very reliable information about the nozzle mode. For reference purposes, two schlieren images are provided in figure 8.19, displaying the nozzle at sea level and altitude modes, recorded at instances indicated by the asterisks in figure 8.18. During the time frame

in between the two asterisks in figure 8.18, two transition events, with one retransition in between, take place. The transition from sea level to altitude mode takes about 0.01 s. The retransition back to sea level mode takes about another 0.01 s, making a period last 0.02 s. If this phenomenon were to occur periodically, this would yield a frequency of around 50Hz.

The bottom part of figure 8.18 provides a longer time frame than the zoomed in graphic at the top of this figure in order to evaluate the envelope of NPR where retransition takes place. When looking at the entire time frame, one can see that from about 0.7 s to 2.7 s into the wind tunnel run, 40 transitions with retransitions, also known as flip-flop, take place. This is very problematic, especially when considering the relatively fast increase in NPR . It also becomes evident that the range of $NPR = 4.2 - 4.4$ is very critical for this nozzle.

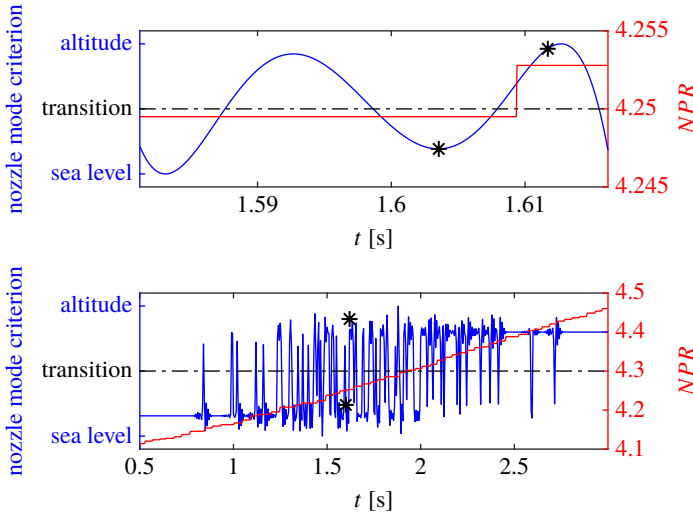


Figure 8.18: Time vs. nozzle mode criterion. Asterisks provide the instance of the schlieren images provided in figure 8.19.

Since retransition can take place throughout such a wide range of NPR , this could indicate that the nozzle has a low hysteresis. Another possibility would be that the flow within the nozzle relaminarizes in the nozzle throat like in the observations of Stark & Wagner (2009). However, the absence of relaminarization was verified by artificially tripping the boundary layer within the nozzle by placing tripping tapes of different thicknesses into the base nozzle. This was carried out symmetrically on both sides of the nozzle, as well as asymmetrically by only placing tripping tape onto one nozzle side. The results of these tests showed no measurable difference in the plume shapes, nor in the frequency of the flip-flop phenomenon.

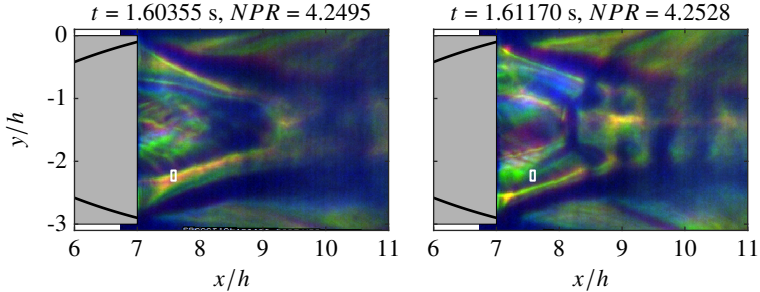


Figure 8.19: Schlieren shadowgraph of the nozzle in sea level mode (left) and in altitude mode (right)

Furthermore, the temporally unsteady RANS simulations of a project partner (Loosen et al. 2018), with the identical model geometry, showed that the shape factor along the nozzle's contour is comparable with the theoretical values of Fenter (1954) for a turbulent flow. Thus, the nozzle flow can be considered turbulent along the entire contour.

Another possibility for retransition, or ultimately the flip-flop phenomenon, is that it is triggered by an interaction of the jet plume with the external flow's Prandtl-Meyer expansion around the nozzle's lip, such as illustrated in figure 8.20. The portion below the axis of symmetry in this figure shows how the transition into altitude mode would cause an instant decrease in the Prandtl-Meyer expansion angle around the nozzle's lip, leading to an increased static pressure in the vicinity of the nozzle exit. This local increase in static pressure then decreases NPR_{eff} below NPR_{tr} , forcing the nozzle flow to retransition back into its sea level mode. On the contrary, the portion above the axis of symmetry shows that when the nozzle flow retransitions back into sea level mode, the Prandtl-Meyer expansion angle around the nozzle's lip instantly increases again, decreasing the static pressure in the vicinity of the nozzle exit. This increases NPR_{eff} back to above NPR_{tr} , triggering the transition back into altitude mode again. The coupled phenomena of the Prandtl-Meyer expansion angle around the nozzle's lip and the nozzle's mode would also explain the reoccurring flip-flop phenomenon taking place. In order to verify these considerations, experiments with a nozzle designed for transitioning in the transonic flight regime need to be carried out. This will yield important information regarding the hysteresis criteria of Dual-Bell nozzles, as well as their feasibility to be used on future space launchers without active control of the transition event.

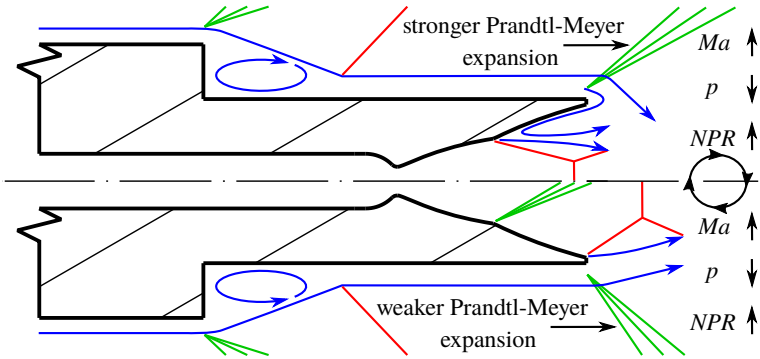


Figure 8.20: Sketch of the possible driving mechanism for the flip-flop phenomenon at supersonic external conditions

8.4 Summary & conclusions on the feasibility of Dual-Bell nozzles

Experimental measurements on planar Dual-Bell nozzle have been carried out in the TWM at both, transonic and supersonic conditions. Both, the sea level mode as well as the altitude mode can be achieved in this experimental setting with a broad range of NPR s. Furthermore, the transition from sea level to altitude mode has been captured via 4-color schlieren recordings at 20kHz.

The results in the sea level mode show that there is a very strong interaction between the nozzle and the external flow. Screeching plays a role in this, which transfers information from the nozzle flow upstream, and thereby leads to shocks above the reattachment surface. The apparently large dynamics of the jet plume in sea level mode could also lead to nozzle side loads or thrust vectoring difficulties on a real launcher application.

Once the nozzle has fully transitioned into the stable regime of the altitude mode, there is no apparent interaction between the nozzle flow and the external flow. Furthermore, the jet plume is very stable in this mode, not causing any potential thrust vectoring problems that may be present in sea level mode.

The presence of multiple flip-flop events over a broad range of NPR is also problematic for the structural integrity of a realistic nozzle. Due to the possible triggering of the flip-flop phenomenon caused by the interaction of the supersonic expansion around the nozzle's lip and the operating mode of the nozzle, a nozzle designed for the transition to occur in the transonic regime could yield more favorable results in the future.

Overall, these results show that an external flow has a dramatic influence on the behavior of a Dual-Bell nozzle. Its effects should always be considered in future investigations. The final research question defined in chapter 2.3 asks if the Dual-Bell concept is a feasible solution for future space launchers. Due to the dynamics of the flip-flop phenomenon, a Dual-Bell nozzle is not feasible for a space launcher application when the transition is designed to occur in supersonic flight. A solution to this problem would be to deliberately control the transitioning by either favorably throttling the combustion chamber pressure in the critical phase of flight, or with the application of active flow control within the nozzle, or to design a nozzle where the transitioning naturally occurs below sonic flight conditions. Therefore, the results do not yield a definite answer to the final research question, however they provide key design guidelines and a future research path for the Dual-Bell concept.

9 Summary & future outlook of space launchers

The beginnings of the Ariane 5 space program were troubled by two catastrophic failures. The second of these failures occurred due to an inherently inefficient, but unavoidable aerodynamic design, which led to a damaging aeroelastic interaction of a turbulent separated shear layer with the nozzle structure. Today, Ariane 5 still experiences the effects of this interaction, also known as buffeting. However, the nozzle structure has been reinforced and shortened in order to avoid damage. Unfortunately, this reduces the payload capacity of the launcher for a specific orbit and increases the cost of launch per unit mass of the payload.

This work identified the fundamental root cause of buffeting and characterized its effect throughout a relevant flight envelope. The existence of four shear layer modes was observed. With increasing free-stream Mach numbers up to sonic conditions, two of these modes merge together. At transonic conditions, the cross-pumping and the step mode were identified to be the cause for the excitation of the structural pendulum and ovalization mode of the Vulcain 2 nozzle, respectively. The step mode is mainly responsible for the high dynamic loads experienced by the nozzle structure, as well as for buffeting on Ariane 5, and is most predominant in the transonic flight regime. As soon as the external flow reaches supersonic conditions, a change in the underlying flow physics occurs, where only the subsonic portion of the flow has a statistical effect on the pressure forces experienced by the reattachment surface. From this point onwards, the dynamic forces decrease significantly, yielding the supersonic phase of flight less critical for a space launcher than the transonic one.

Following this, a solution for weakening the step mode in the transonic regime was presented. Through the application of passive flow control, the root mean square of the dynamic pressure loads was locally decreased by around 35%, while the mean reattachment length was reduced by over 80%. This reduced the dynamic moment about the step by 25%. Next to this, the most effective passive flow control device diffused the traces of the step mode in the pressure signatures on the reattachment surface. The most efficient geometry tested was comprised of square lobes, which nearly had a flow penetration height of the boundary layer and a periodicity similar to naturally occurring finger-like structures in the shear layer. Further testing with these types of lobes in the future could answer the question whether the height of these flow control devices, or their periodicity, have a greater effect on their performance. It should be emphasized that besides additional drag associated with most of the flow control devices, none of the geometries tested provided any negative effects regarding the load dynamics in the supersonic regime. This type of flow control device could be attached to current launchers as part of the boosters, which are ejected past the critical buffeting phase of flight. This would dispose of the excess weight at an early stage of flight.

Prior to investigating a novel nozzle concept, a planar launcher model with a generic rocket nozzle was designed. Its design process and experimental validation were summarized, while the interaction of the separated shear layer with the nozzle flow was also studied. The interaction of the two flows is negligible for the tested configuration. The presence of the jet plume did not have a notable effect on the velocity vector field statistics, besides shortening the mean reattachment length. *Vise-versa*, the shear layer does not have a statistical effect on the nozzle flow. Furthermore, the shear layer dynamics do not lead to nozzle flow separation even for a highly overexpanded nozzle flow.

The successful elimination of the root cause for buffeting allows for longer, hence more efficient, nozzle designs. Therefore, the feasibility of a Dual-Bell nozzle for the application on a space launcher was investigated at last. The experiments investigated the behavior of a Dual-Bell's jet plume subjected to an external flow. These are part of the first published investigations that consider the effects of an external flow on the jet plume. The effects of an external flow proved to be crucial, as its presence has significant effects on the external flow field topology and the behavior of the jet plume. For one, nozzle screeching was observed in the sea level mode at transonic free-stream conditions. When the sound waves produced by screeching are superimposed onto the transonic external flow, undulations of the jet plume and shocks close to the nozzle fairing are generated. This could pose difficulties to a space launcher's thrust vectoring and structural integrity, respectively. In addition, the nozzle's altitude mode was observed for $NPR \ll NPR_{tr}$ at supersonic external flow conditions. Therefore, a more precise formulation of the nozzle pressure ratio, the effective nozzle pressure ratio (NPR_{eff}), was introduced in this work, which takes the supersonic expansion around the nozzle's lip into account. This quantity should always be used when designing nozzles for applications that travel close to, or above the speed of sound. More importantly however, the interaction of a supersonic external flow with the transitioning Dual-Bell nozzle flow may excite multiple retransitions, or flip-flop, to occur over a wide range of NPR_{eff} , during which either operating condition of the nozzle is unstable. This observation limits the feasibility of a Dual-Bell nozzle, at least as long as it is designed for the transition to occur in supersonic flight.

Therefore, future research on this type of nozzle should focus on a transition below sonic free-stream conditions. If the flip-flop phenomenon is avoided in that flight envelope, then the hypothesis regarding the supersonic interaction being responsible for the flip-flop is verified. This would yield the Dual-Bell nozzle concept with a natural transition feasible again. If flip-flop were still to occur in transonic flight conditions, more complex solutions would have to be considered to control the transition from sea level to altitude mode. Such a solution could be the application of active flow control at the contour inflection of the nozzle, forcing the jet plume to maintain sea level mode past its natural transition point. Once the atmospheric pressure decreases below a certain threshold, the active flow control could be turned off, allowing transition to occur at $NPR_{eff} \gg NPR_{tr}$. Another idea that could avoid the use of active flow control would be a nozzle designed to transition just past $Ma_\infty = 1$. The sudden pressure drop around the nozzle's lip with the onset of a

Prandtl-Meyer expansion may be large enough to maintain altitude mode after the nozzle's transitioning.

In conclusion, the control of buffeting allows for more efficient nozzle concepts to be mounted onto today's space launchers. The Dual-Bell nozzle concept is a promising solution, which could easily be integrated on existing launcher systems. Further investigations are necessary in order to quantify the transitioning of this type of nozzle at relevant external flow conditions. If a natural transition without retransitioning can be achieved, the application of this type of nozzle could follow on the next generation of launchers, increasing their payload capacity on the order of 5 – 10% for geostationary transfer orbit missions.

LIST OF REFERENCES

- ABBOTT DE & KLINE SJ (1962). *Experimental Investigation of Subsonic Turbulent Flow Over Single and Double Backward Facing Steps*. J Basic Eng - T ASME 84:317–325, DOI: 10.1115/1.3657313
- ADRIAN RJ (1984). *Scattering particle characteristics and their effect on pulsed laser measurements of fluid flow: speckle velocimetry vs. particle image velocimetry*. Appl Optics 23:1690–1691, DOI: 10.1364/AO.23.001690
- ADRIAN RJ (2005). *Twenty years of particle image velocimetry*. Exp Fluids 39:159–169, DOI: 10.1007/s00348-005-0991-7
- AHLBERG JH, HAMILTON S, MGDAL D & NILSON EN (1961). *Truncated Perfect Nozzles in Optimum Nozzle Design*. ARSJ-AM Rocket Soc J 31:614–620, DOI: 10.2514/8.5577
- ALKISLAR MB, KROTHAPALLI A & LOURENCO LM (2003). *Structure of a screeching rectangular jet: a stereoscopic particle image velocimetry study*. J Fluid Mech 489:121–154, DOI: 10.1017/S0022112003005032
- ANDERSON JD JR (ed) (2007). *Fundamentals of Aerodynamics*, 4th edn. McGraw-Hill, New York, NY, USA, ISBN: 978-0-07-295046-5
- ARENS M & SPIEGLER E (1963). *Shock-Induced Boundary Layer Separation in Overexpanded Conical Exhaust Nozzles*. AIAA J 1:578–581, DOI: 10.2514/3.1598
- ARIANESPACE (2016a). *Ariane 5 user’s manual*. Arianespace
- ARIANESPACE (2016b). *Arianespace confirms its status as the most reliable launch services provider in the marketplace, while actively preparing for the future in order to always better serve its clients*. Press release, ArianeSpace website, Online; accessed 27-August-2018
- AVALLONE F, DISCETTI S, ASTARITA T & CARDONE G (2015). *Convergence enhancement of single-pixel PIV with symmetric double correlation*. Exp Fluids 56:1–11, DOI: 10.1007/s00348-015-1938-2
- BADRI NARAYANAN MAB, KHADGI YN & VISWANATH PR (1974). *Similarities in Pressure Distribution in Separated Flow Behind Backward-Facing Steps*. Aeronaut Quart 25:305–312, DOI: 10.1017/S0001925900007095
- BARKER DB & FORNEY ME (1977). *Measuring fluid velocities with speckle patterns*. Opt Lett 1:135–137, DOI: 10.1364/OL.1.000135
- BARKLAGE A, RADESPIEL R & GÉNIN C (2018). *Afterbody Jet Interaction of a Dual-Bell Nozzle in Supersonic Flow*. In: 2018 Joint Propulsion Conference, Cincinnati, OH, USA, DOI: 110.2514/6.2018-4468

- BARKLEY D, GOMES MGM & HENDERSON RD (2002). *Three-dimensional instability in flow over a backward-facing step*. J Fluid Mech 473:167–190, DOI: 10.1017/S002211200200232X
- BEAUDOIN J-F, CADOT O, AIDER J-L & WESFREID JE (2004). *Three-dimensional stationary flow over a backward-facing step*. Eur J Mech B/Fluids 23:147–155, DOI: 10.1016/j.euromechflu.2003.09.010
- BERNARD N, SUJAR-GARRIDO P, BONNET J-P & MOREAU E (2016). *Control of the coherent structure dynamics downstream of a backward-facing step by DBD plasma actuator*. Int J Heat Fluid Fl 61:158–173, DOI: 10.1016/j.ijheatfluidflow.2016.04.009
- BERNARDINI M & PIROZZOLI S (2011). *Wall pressure fluctuations beneath supersonic boundary layers*. Phys Fluids 23:1–11, DOI: 10.1063/1.3622773
- BITTER M, SCHARNOWSKI S, HAIN R & KÄHLER CJ (2011). *High-repetition-rate PIV investigations on a generic rocket model in sub- and supersonic flows*. Exp Fluids 50:1019–1030, DOI: 10.1007/s00348-010-0988-8
- BLOOMER HE, ANTL RJ & RENAS PE (1962). *Experimental Study of Effects of Geometric Variables on Performance of Conical Rocket-Engine Exhaust Nozzles*. Technical report NASA TN D-846, National Aeronautics and Space Administration NASA, Lewis Research Center, Cleveland OH, USA
- BOLGAR I & KÄHLER CJ (2017a). *Stand der Forschung und geplante Arbeiten im Teilprojekt B6*. DFG SFB-TRR40 meeting group B, Presentation slides are available online on the DFG SFB-TRR40 server, Project meeting on 29.06.2017 in Neubiberg, Germany
- BOLGAR I & KÄHLER CJ (2017b). *Stand der Forschung und geplante Arbeiten im Teilprojekt B6*. DFG SFB-TRR40 meeting group B, Presentation slides are available online on the DFG SFB-TRR40 server, Project meeting on 16.10.2017 in Braunschweig, Germany
- BOLGAR I, SCHARNOWSKI S & KÄHLER CJ (2015). *Control of the Reattachment Length of a Transonic 2D Backward-Facing Step Flow*. In: International Conference on Jets, Wakes and Separated Flows 2015, Stockholm, Sweden
- BOLGAR I, SCHARNOWSKI S & KÄHLER CJ (2016). *Control of the Reattachment Length of a Transonic 2D Backward-Facing Step Flow*. In: SEGALINI A (ed) Proceedings of the 5th International Conference on Jets, Wakes and Separated Flows (ICJWSF2015), Springer International Publishing, Cham, Switzerland, *Springer Proc Phys*, vol 185, pp 241–248, DOI: 10.1007/978-3-319-30602-5_30
- BOLGAR I, SCHARNOWSKI S & KÄHLER CJ (2017). *Correlations between turbulent wall pressure and velocity field fluctuations in backward-facing step flows*. In: Deutscher Luft- und Raumfahrtkongress 2017, Deutsche Gesellschaft für Luft- und Raumfahrt, Munich, Germany

-
- BOLGAR I, SCHARNOWSKI S & KÄHLER CJ (2018). *The Effect of the Mach Number on a Turbulent Backward-Facing Step Flow*. *Flow Turbul Combust* 101:653–680, DOI: 10.1007/s10494-018-9921-7, published online April 25th, 2018
- BOLGAR I, SCHARNOWSKI S & KÄHLER CJ (2019a). *Experimental analysis of the interaction between a Dual-Bell nozzle with an external flow field aft of a backward-facing step*. In: *New Results in Numerical and Experimental Fluid Mechanics*, Springer Nature Switzerland AG, Cham, Switzerland, *Notes on Numerical Fluid Mechanics and Multidisciplinary Design*, vol XII, pp 405–415
- BOLGAR I, SCHARNOWSKI S & KÄHLER CJ (2019b). *Passive Flow Control for Reduced Load Dynamics Aft of a Backward-Facing Step*. *AIAA J* 57:120–131, DOI: 10.2514/1.J057274
- BRADSHAW P & WONG FYF (1972). *The reattachment and relaxation of a turbulent shear layer*. *J Fluid Mech* 52:113–135, DOI: 10.1017/S002211207200299X
- DE BREDERODE VA (1975). *Three-Dimensional Effects in Nominally Two-Dimensional Flows*. Doctoral dissertation, Imperial College London, London, Great Britain
- BROWN GL & ROSHKO A (1974). *On density effects and large structure in turbulent mixing layers*. *J Fluid Mech* 64:775–816, DOI: 10.1017/S002211207400190X
- BUCHMANN NA, KÜCÜKOSMAN YC, EHRENFRIED K & KÄHLER CJ (2016). *Wall pressure signature in compressible turbulent boundary layers*. *Progress in Wall Turbulence* 2:93–102, DOI: 10.1007/978-3-319-20388-1_8
- BUHL W, EBERT K & HERBST H (1992). *Optimal Ascent Trajectories for Advanced Launch Vehicles*. In: *AIAA Fourth International Aerospace Planes Conference*, AIAA, Orlando, FL, USA
- CAMPBELL C & FARLEY J (1960). *Performance of Several Conical Convergent-Divergent Rocket-Type Exhaust Nozzles*. Technical report NASA TN D-467, National Aeronautics and Space Administration NASA, Lewis Research Center, Cleveland, OH, USA
- CHEMOUL B, LOUAAS E, ROUX P, SCHMITT D & POURCHER M (2001). *Ariane 5 flight environments*. *Acta Astronaut* 48:275–285, DOI: 10.1016/S0094-5765(01)00026-1
- CHERRY NJ, HILLIER R & LATOUR MEMP (1984). *Unsteady measurements in a separated and reattaching flow*. *J Fluid Mech* 144:13–46, DOI: 10.1017/S002211208400149X
- CHOVET C, LIPPERT M, FOUCAUT J-M & KEIRSBULCK L (2017). *Dynamical aspects of a backward-facing step flow at large Reynolds numbers*. *Exp Fluids* 58, DOI: 10.1007/s00348-017-2444-5
- CHUN S, LEE I & SUNG HJ (1999). *Effect of spanwise-varying local forcing on turbulent separated flow over a backward-facing step*. *Exp Fluids* 26:437–440, DOI: 10.1007/s003480050307

REFERENCES

- COUCH L & BROOKS CW JR (1973). *Effect of Blockage Ratio on Drag and Pressure Distributions for Bodies of Revolution at Transonic Speeds*. Technical report NASA TN D-7331, National Aeronautics and Space Administration NASA
- COULON D (2000). *Vulcain-2 Cryogenic Engine Passes First Test with New Nozzle Extension*. Bulletin 102, ESA
- DECK S & THORIGNY P (2007). *Unsteadiness of an axisymmetric separating-reattaching flow: Numerical investigation*. Phys Fluids 19:065103, DOI: 10.1063/1.2734996
- DEPRES D, REIJASSE P & DUSSAUGE JP (2004). *Analysis of Unsteadiness in Afterbody Transonic Flows*. AIAA J 42:2541–2550, DOI: 10.2514/1.7000
- DEPUYDT M, RMIANDRASOA F & JACQUOT F (1997). *Exploitation des essais buffeting Ariane 5 en l'absence et en présence de jets*. Campagnes ONERA 1,2 et 3 A5-RE-1-A-271-ASAI, Ariane 5, ONERA, YX/SA no. 124995 du 24/10/1997
- DOLLING DS (2001). *Fifty Years of Shock-Wave/Boundary Layer Interaction Research: What Next?* AIAA J 39:1517–1531, DOI: 10.2514/2.1476
- DRIVER DM, SEEGMILLER HL & MARVIN JG (1987). *Time-Dependent Behavior of a Reattaching Shear Layer*. AIAA J 25:914–919, DOI: 10.2514/3.9722
- DUDDERAR TD & SIMPKINS PG (1977). *Laser speckle photography in a fluid medium*. Nature 270:45–47, DOI: 10.1038/270045a0
- EATON JK & JOHNSTON JP (1980). *Turbulent flow reattachment: An experimental study of the flow and structure behind a backward-facing step*. Technical report, Dept. of Mech. Eng., Stanford Univ.
- EATON JK & JOHNSTON JP (1981). *A Review of Research on Subsonic Turbulent Flow Reattachment*. AIAA J 19:1093–1100, DOI: 10.2514/3.60048
- EATON JK, JOHNSTON JP & JEANS AH (1979). *Measurements in a Reattaching Turbulent Shear Layer*. In: Proceedings of the 2nd Symposium on Turbulent Shear Flows, London, UK
- EITEL-AMOR G, ÖRLÜ R & SCHLATTER P (2014). *Simulation and validation of a spatially evolving turbulent boundary layer up to $Re_\theta = 8300$* . Int J Heat Fluid Fl 47:57–69, DOI: 10.1016/j.ijheatfluidflow.2014.02.006
- ESA (2019). *European Space Agency – Images*. ESA website
- FARLEY J & CAMPBELL C (1960). *Performance of Several Method-of-Characteristic Exhaust Nozzles*. Technical report NASA TN D-293, National Aeronautics and Space Administration NASA, Lewis Research Center, Cleveland, OH, USA
- FENTER FW (1954). *A New Analytical Method for the Prediction of Turbulent Boundary Layer Characteristics on a Thermally Insulated Flat Plate at Supersonic Speeds*. Technical report DRL-343, University of Texas, Austin, TX, USA

-
- FOSTER C & COWLES F (1949). *Experimental Study of Gas-Flow Separation in Overexpanded Exhaust Nozzles for Rocket Motors*. JPL progress report 4-103, Jet Propulsion Lab., California Inst. of Technology
- FOX DG & LILLY DK (1972). *Numerical Simulation of Turbulent Flows*. Rev Geophys Space GE 10:51–72, DOI: 10.1029/RG010i001p00051
- FRASER RP, EISENKLAM P & WILKIE D (1959). *Investigation of Supersonic Flow Separation in Nozzles*. J Mech Eng Sci 1:267–279, DOI: 10.1243/2FJMES_JOUR_1959_001_031_02
- FREY M (2001). *Behandlung von Strömungsproblemen in Raketendüsen bei Überexpansion*. Doctoral dissertation, Universität Stuttgart, Stuttgart, Germany
- FREY M & HAGEMANN G (1999). *Critical Assessment of Dual-Bell Nozzles*. J Propul Power 15:137–143, DOI: 10.2514/2.5402
- GÉNIN C & STARK RH (2011). *Side Loads in Subscale Dual Bell Nozzles*. J Propul Power 27:828–837, DOI: 10.2514/1.B34170
- GEURTS EGM (2006). *Steady and unsteady pressure measurements on the rear section of various configurations of the Ariane 5 launch vehicle*. Technical report NLR-TP-2006-596, National Aerospace Laboratory NLR
- GINOUX JJ (1971). *Streamwise vortices in reattaching high-speed flows - A suggested approach*. AIAA J 9:759–760, DOI: 10.2514/3.6271
- GROUSSON R & MALICK S (1977). *Study of flow pattern in a fluid by scattered laser light*. Appl Optics 16:2334–2336, DOI: 10.1364/AO.16.002334
- HAGEMANN G, TERHARDT M, HAESLER D & FREY M (2002). *Experimental and Analytical Design Verification of the Dual-Bell Concept*. J Propul Power 18, DOI: 10.2514/2.5905
- GAD-EL HAK M, POLLARD A & BONNET J-P (eds) (2003). *Flow control: Fundamentals and Practices*, vol 53. Springer-Verlag, Berlin Heidelberg, Germany, ISBN: 3-540-63936-5
- HALUPOVICH Y, NATAN B & ROM J (1999). *Numerical solution of the turbulent supersonic flow over a backward facing step*. Fluid Dyn Res 24:251–273, DOI: 10.1007/s00348-006-0247-1
- HAMPEL A (1984). *Auslegung, Optimierung und Erprobung eines vollautomatisch arbeitenden Transsonik-Windkanals*. Doctoral dissertation, Hochschule der Bundeswehr, Neubiberg, Germany
- HANNEMANN K, LÜDEKE H, PALLEGOIX J-F, OLLIVIER A, LAMBARÉ H, MASELAND JEJ, GEURTS EGM, FREY M, DECK S, SCHRIJER FFJ, SCARANO F & SCHWANE R (2011). *Launch vehicle base buffeting - recent experimental and numerical investigations*. In: Proceedings 7th European Symposium on Aerothermodynamics for Space Vehicles, Brugge, Belgium

REFERENCES

- HASAN MAZ (1992). *The flow over a backward-facing step under controlled perturbation*. J Fluid Mech 238:73–96, DOI: 10.1017/S0022112092001642
- HEENAN AF & MORRISON JF (1998). *Passive Control of Pressure Fluctuations Generated by Separated Flow*. AIAA J 36:1014–1025, DOI: 10.2514/2.474
- HO C-M & HUERRE P (1984). *Perturbed Free Shear Layers*. Ann Rev Fluid Mech 16:365–424, DOI: 10.1146/annurev.fl.16.010184.002053
- HORN M & FISHER S (1993). *Dual-Bell Altitude Compensating Nozzles*. Technical report 19940018584, National Aeronautics and Space Administration NASA, Rockwell International Corp., Rocketdyne Div., Canoga Park, CA, USA
- HUDY LM, NAGUIB A & HUMPHREYS WM (2007). *Stochastic estimation of a separated-flow field using wall-pressure-array measurements*. Phys Fluids 19, DOI: 10.1063/1.2472507
- IMMICH H & CAPORICCI M (1996). *FESTIP technology developments in liquid rocket propulsion for reusable launch vehicles*. In: 32nd Joint Propulsion Conference and Exhibit, AIAA, Lake Buena Vista, FL, USA
- ISOMOTO K & HONAMI S (1989). *The Effect of Inlet Turbulence Intensity on the Reattachment Process over Backward-Facing Step*. J Fluid Eng-T ASME 111:87–92, DOI: 10.1115/1.3243604
- KÄHLER CJ, SAMMLER B & KOMPENHANS J (2002). *Generation and control of tracer particles for optical flow investigations in air*. Exp Fluids 33:736–742, DOI: 10.1007/s00348-002-0492-x
- KÄHLER CJ, SCHARNOWSKI S & CIERPKA C (2012). *On the resolution limit of digital particle image velocimetry*. Exp Fluids 52:1629–1639, DOI: 10.1007/s00348-012-1280-x
- KALT S & BADAL DL (1965). *Conical Rocket Nozzle Performance under Flow-Separated Conditions*. J Spacecraft Rockets 2:447–449, DOI: 10.2514/3.28200
- KANG S & CHOI H (2002). *Suboptimal feedback control of turbulent flow over a backward-facing step*. J Fluid Mech 463:201–227, DOI: 10.1017/S0022112002008728
- KILGORE RA, GOODYER MJ, ADCOCK JB & EE DAVENPORT (1974). *The Cryogenic Wind-Tunnel Concept for High Reynolds Number Testing*. Technical report NASA TN D-7762, National Aeronautics and Space Administration NASA, Langley Research Center, Hampton, VA 23665, USA
- KISTLER AL (1964). *Fluctuating Wall Pressure under a Separated Supersonic Flow*. J ACOUST SOC AM 36:543–550, DOI: 10.1121/1.1918998
- KOLMOGOROV A (1941). *The Local Structure of Turbulence in Incompressible Viscous Fluid for Very Large Reynolds' Numbers*. Akademiia Nauk SSSR Doklady 30:301–305
- KREVSOKOVSKY JP, SHAMROTH SJ & McDONALD H (1974). *Parametric relaminarization of turbulent boundary layers on nozzle walls*. Technical report NASA CR-2370, National

Aeronautics and Space Administration NASA, United Aircraft Corp., East Hartford, CT, USA

- KUEHN DM (1980). *Effects of Adverse Pressure Gradient on the Incompressible Reattaching Flow over a Rearward-Facing Step*. AIAA J 18:343–344, DOI: 10.2514/3.50765
- KUMAR R & VISWANATH PR (2002). *Mean and Fluctuating Pressure in Boat-Tail Separated Flows at Transonic Speeds*. J Spacecraft Rockets 39:430–438, DOI: 10.2514/2.3826
- DE LAVAL CGP (1894). *Steam Turbine*. US Patent
- LAWRENCE RA (1967). *Symmetrical and Unsymmetrical Flow Separation in Supersonic Nozzles*. Doctoral dissertation, Southern Methodist University, University Park, TX, USA
- LAWRENCE RA & WEYNAND EE (1968). *Factors Affecting Flow Separation in Contoured Supersonic Nozzles*. AIAA J 6:1159–1160, DOI: 10.2514/3.4693
- LE H, MOIN P & KIM J (1997). *Direct numerical simulation of turbulent flow over a backward-facing step*. J Fluid Mech 330:349–374, DOI: 10.1017/S0022112096003941
- LEE I & SUNG HJ (2001). *Characteristics of wall pressure fluctuations in separated and reattaching flows over a backward-facing step*. Exp Fluids 30:262–272, DOI: 10.1007/s003480000172
- LIONS J-L, LÜBECK L, FAUQUEMBERGUE J-L, KAHN G, KUBBAT W, LEVEDAG S, MAZZINI L, MERLE D & O'HALLORAN C (1996). *Ariane 5 Flight 501 Failure Report by the Inquiry Board*. Tech. rep., ESA
- LOOSEN S, MEINKE M & SCHRÖDER W (2018). *TP B3: Numerical Analysis of Space Launcher Wake Flows*. DFG SFB-TRR40 meeting group B, Presentation slides are available online on the DFG SFB-TRR40 server, Project meeting on 20.12.2018 in Braunschweig, Germany
- MARIE S, LAMARÉ H & DRUAULT P (2011). *A modal overview of the unsteady loads induced by the Ariane-5 base-flow*. In: 4th European Conference for Aerospace Sciences, EUCASS association, St. Petersburg, Russia, pp 1–21
- MARIE S, DRUAULT P, LAMARÉ H & SCHRIJER F (2013). *Experimental analysis of the pressure-velocity correlations of external unsteady flow over rocket launchers*. Aerosp Sci Technol 30:83–93, DOI: 10.1016/j.ast.2013.07.006
- MARTELLI E, NASUTI F & ONOFRI M (2007). *Numerical Parametric Analysis of Dual-Bell Nozzle Flows*. AIAA J 45:640–650, DOI: 10.2514/1.26690
- MCCORMICK DC & BENNETT JR JC (1994). *Vortical and Turbulent Structure of a Lobed Mixer Free Shear Layer*. AIAA J 32:1852–1859, DOI: 10.2514/3.12183
- MCGUINNESS 1978 (1978). *Flow with a separation bubble: Steady and unsteady aspects*. Doctoral dissertation, University of Cambridge, Cambridge, UK

REFERENCES

- MENDEZ MA, RAIOLA M, MASULLO A, DISCETTI S, IANIRO A, THEUNISSEN R & BUCHLIN J-M (2017). *POD-based background removal for particle image velocimetry*. *Exp Therm Fluid Sci* 80:181–192, DOI: 10.1016/j.expthermflusci.2016.08.021
- MENGLE VG (2005). *Jet Noise Reduction of Chevrons in Internally Mixed Nozzles*. In: 11th AIAA/CEAS Aeroacoustics Conference, AIAA, Monterey, CA, USA, *AIAA Aeroacoustics Conference*, vol 26
- NAVE L & COFFEY G (1973). *Sea Level Side Loads in High-Area-Ratio Rocket Engines*. In: AIAA/SAE 9th Propulsion Conference, AIAA, Las Vegas, NV, USA, DOI: 10.2514/6.1973-1284
- NEUMANN J & H WENGLE (2003). *DNS and LES of Passively Controlled Turbulent Backward-Facing Step Flow*. *Flow Turbul Combust* 71:297–310, DOI: 10.1023/B:APPL.0000014915.18571.06
- NILSSON J, SZÁSZ R-Z & GUTMARK EJ (2016). *Passive Load Control in Backward-Facing Step Flow by Using Chevrons*. In: SEGALINI A (ed) *Proc. of the 5th Int. Conf. on Jets, Wakes and Separated Flows (ICJWSF2015)*, Springer International Publishing, Cham, Switzerland, *Springer Proc Phys*, vol 185, pp 241–248, DOI: 10.1007/978-3-319-30602-5_28
- NÜRNBERGER-GÉNIN C & STARK RH (2009). *Flow transition in dual bell nozzles*. *Shock Waves* 19:265–270, DOI: 10.1007/s00193-008-0176-4
- NÜRNBERGER-GÉNIN C & STARK RH (2010). *Experimental Study on Flow Transition in Dual Bell Nozzles*. *Shock Waves* 126:497–502, DOI: 10.2514/1.47282
- NYQUIST H (1928). *Certain Topics in Telegraph Transmission Theory*. *Transactions of the American Institute of Electrical Engineers* 47:617–644, DOI: 10.1109/T-AIEE.1928.5055024
- ORSZAG SA & PATTERSON GS JR (1972). *Numerical Simulation of Three-Dimensional Homogeneous Isotropic Turbulence*. *Phys Rev Lett* 28:76–79, DOI: 10.1103/PhysRevLett.28.76
- PANDA J (1998). *Shock oscillation in underexpanded screeching jets*. *J Fluid Mech* 363:173–198, DOI: 10.1017/S0022112098008842
- PARK H, JEON W-P, CHOI H & YOO JY (2007). *Mixing enhancement behind a backward-facing step using tabs*. *Phys Fluids* 19:105103, DOI: 10.1063/1.2781597
- PATEL RP (1978). *Effects of Stream Turbulence on Free Shear Flows*. *Aeronaut Quart* 29:33–43, DOI: 10.1017/S0001925900008295
- PERGIO D, SCHWANE R & WONG H (2003). *A Numerical Comparison of the Flow in Conventional and Dual Bell Nozzles in the Presence of an Unsteady External Pressure Environment*. In: 39th Joint Propulsion Conference and Exhibit, AIAA, Huntsville, AL, USA, DOI: 10.2514/6.2003-4731

-
- PIPONNIAU S, DUSSAUGE JP, DÈBIEVE JF & DUPONT P (2009). *A simple model for low-frequency unsteadiness in shock-induced separation*. J Fluid Mech 629:87–108, DOI: 10.1017/S0022112009006417
- RAFFEL M, WILLERT CE, SCARANO F, KÄHLER CJ, WERELEY S & KOMPENHANS J (2018). *Particle Image Velocimetry: A Practival Guide*, 3rd edn. Springer International Publishing, Cham, Switzerland, DOI: 10.1007/978-3-319-68852-7
- RAGNI D, SCHRIJER F, OUDHEUSDEN BW & SCARANO F (2011). *Particle tracer response across shocks measured by PIV*. Exp Fluids 50:53–64, DOI: 10.1007/s00348-010-0892-2
- RAMIANDRASOA F (2000). *Complément d'exploitation des essais en soufflerie d'aérodynamique au culot (NLR 1999)*. Estimation de l'erreur due à l'intégration des mesures de pression sur le divergent Vulcain 2 Ariane 5 Plus, A5-RE-1-X-296-ASAI, NLR, YX/FL no. 132890 du 19/12/2000
- RAO GVR (1958). *Exhaust Nozzle Contour for Optimum Thrust*. Journal of Jet Propulsion 28:377–382, DOI: 10.2514/8.7324
- REYNOLDS O (1883). *An experimental investigation of the circumstances which determine whether the motion of water shall be direct or sinuous, and of the law of resistance in parallel channels*. Philosophical Transactions of the Royal Society of London 174:935–982, DOI: 10.1098/rstl.1883.0029
- RODGERS JL & NICEWANDER WA (1988). *Thirteen Ways to Look at the Correlation Coefficient*. Am Stat 42:59–66, DOI: 10.1080/00031305.1988.10475524
- RONA A & ZHANG X (2004). *Time accurate numerical study of turbulent supersonic jets*. J Sound Vib 270:297–321, DOI: 10.1016/S0022-460X(03)00537-6
- ROSHKO A & THOMKE GJ (1966). *Observations of Turbulent Reattachment behind an Axisymmetric Downstream-Facing Step in Supersonic Flow*. AIAA J 4:975–980, DOI: 10.2514/3.3590
- ROSS CB, LOURENCO LM & KROTHAPALLI A (1994). *Particle Image Velocimetry Measurements in a Shock-Containing Supersonic Flow*. AIAA J 94-0047, DOI: 10.2514/6.1994-47
- SCHARNOWSKI S (2013). *Investigation of turbulent shear flows with high resolution PIV methods*. Doctoral dissertation, Universität der Bundeswehr München, Neubiberg, Germany
- SCHARNOWSKI S & KÄHLER CJ (2013). *On the effect of curved streamlines on the accuracy of PIV vector fields*. Exp Fluids 54:1435, DOI: 10.1007/s00348-012-1435-9
- SCHARNOWSKI S & KÄHLER CJ (2015). *Investigation of a transonic separating/reattaching shear layer by means of PIV*. Theoretical and Applied Mechanics Letters 5:30–34, DOI: 10.1016/j.taml.2014.12.002

- SCHARNOWSKI S & KÄHLER CJ (2016). *Estimation and optimization of loss-of-pair uncertainties based on PIV correlation functions*. Exp Fluids 57:23, DOI: 10.1007/s00348-015-2108-2
- SCHARNOWSKI S, BOLGAR I & KÄHLER CJ (2015). *Control of the recirculation region of a transonic backward-facing step flow using circular lobes*. In: 9th Int. Symp. on Turbulence and Shear Flow Phenomena (TSFP-9), Melbourne, Australia
- SCHARNOWSKI S, BOLGAR I & KÄHLER CJ (2017). *Characterization of turbulent structures in a transonic backward-facing step flow*. Flow Turbul Combust 95:947–967, DOI: 10.1007/s10494-016-9792-8
- SCHARNOWSKI S, BOSYK M, SCHRIJER FJ & VAN OUDHEUSDEN BW (2019a). *Passive Flow Control for the Load Reduction of Transonic Launcher Afterbodies*. AIAA J 57:1818–1825, DOI: 10.2514/1.J057357
- SCHARNOWSKI S, BROSS M & KÄHLER CJ (2019b). *Accurate turbulence level estimations using PIV/PTV*. Exp Fluids 60, DOI: 10.1007/s00348-018-2646-5
- SHELLER K (1953). *Some Experiments on Flow Separation in Rocket Nozzles*. J Am Rocket Soc 23:28–32, DOI: 10.2514/8.4528
- SCHLICHTING H & GERSTEN K (2006). *Grenzschicht-Theorie*, vol 10. Springer-Verlag, Berlin Heidelberg, Germany
- SCHMUCKER R (1973a). *Strömungsvorgänge beim Betrieb überexpandierter Düsen chemischer Raketentriebwerke, Teil1: Strömungsablösung*. Technical report Bericht TB-7, Technische Universität München
- SCHMUCKER R (1973b). *Strömungsvorgänge beim Betrieb überexpandierter Düsen chemischer Raketentriebwerke, Teil2: Seitenkräfte durch unsymmetrische Ablösung*. Technical report Bericht TB-10, Technische Universität München
- SCHRIJER FFJ, SCIACCHITANO A & SCARANO F (2010). *Experimental investigation of flow control devices for the reduction of transonic buffeting on rocket afterbodies*. In: Proceedings of the 15th International Symposium on Applications of Laser Techniques to Fluid Mechanics
- SCHRIJER FFJ, SCIACCHITANO A, SCARANO F, HANNEMAN K, PALLEGOIX J-F, MASELAND JEJ & SCHWANE R (2011). *Experimental Investigation of Base Flow Buffeting on the Ariane 5 Launcher Using High Speed PIV*. In: Proceedings 7th European Symposium on Aerothermodynamics for Space Vehicles, Brugge, Belgium, vol 692, p 102
- SCHRIJER FFJ, SCIACCHITANO A & SCARANO F (2014). *Spatio-temporal and modal analysis of unsteady fluctuations in a high-subsonic base flow*. Phys Fluids 26, DOI: 10.1063/1.4891257
- SHANNON CE (1949). *Communication in the Presence of Noise*. Proceedings of the IRE 37:10–21, DOI: 10.1109/JRPROC.1949.232969

-
- SIGURDSON LW (1995). *The structure and control of a turbulent reattaching flow*. J Fluid Mech 298:139–165, DOI: 10.1017/S0022112095003259
- SIMPSON RL (1989). *Turbulent boundary-layer separation*. Annu Rev Fluid Mech 21:205–232, DOI: 10.1146/annurev.fl.21.010189.001225
- SINGH A & CHATTERJEE A (2007). *Numerical prediction of supersonic jet screech frequency*. Shock Waves 17:263–272, DOI: 10.1007/s00193-007-0110-1
- STARK R & HAGEMANN G (2007). *Current status of numerical flow prediction for separated nozzle flows*. In: 2nd European Conference for Aerospace Sciences (EUCASS), EUCASS association, Brussels, Belgium
- STARK RH & WAGNER B (2009). *Experimental study of boundary layer separation in truncated ideal contour nozzles*. Shock Waves 19:185–191, DOI: 10.1007/s00193-008-0174-6
- STARK RH, GÉNIN C, SCHNEIDER D & FROMM C (2016). *Ariane 5 Performance Optimization Using Dual-Bell Nozzle Extension*. J Spacecraft Rockets 53:743–750, DOI: 10.2514/1.A33363
- STATNIKOV V, BOLGAR I, SCHARNOWSKI S, MEINKE M, KÄHLER CJ & SCHRÖDER W (2015). *Analysis of characteristic wake flow modes on a generic planar transonic space launcher configuration*. In: 6th European Conference for Aeronautics and Space Science (EUCASS), Krakow, Poland
- STATNIKOV V, BOLGAR I, SCHARNOWSKI S, MEINKE M, KÄHLER CJ & SCHRÖDER W (2016a). *Analysis of characteristic wake flow modes on a generic transonic backward-facing step configuration*. Eur J Mech – B/Fluids 59:124–134, DOI: 10.1016/j.euromechflu.2016.05.008
- STATNIKOV V, ROIDL B, MEINKE M & SCHRÖDER W (2016b). *Analysis of spatio-temporal wake modes of space launchers at transonic flow*. In: 54th AIAA Aerospace Sciences Meeting, DOI: 10.2514/6.2016-1116
- STATNIKOV V, STEPHAN S, PAUSCH K, MEINKE M, RADESPIEL R & SCHRÖDER W (2016c). *Experimental and numerical investigations of the turbulent wake flow of a generic space launcher at $M_\infty = 3$ and $M_\infty = 6$* . CEAS Space J 8:101–116, DOI: 10.1007/s12567-016-0112-x
- STATNIKOV V, MEINKE M & SCHRÖDER W (2017). *Reduced-order analysis of buffet flow of space launchers*. J Fluid Mech 815:1–25, DOI: 10.1017/jfm.2017.46
- STODOLA A (1924). *Dampf- und Gasturbinen*, 6th edn. Springer-Verlag GmbH, Berlin Heidelberg, DOI: 10.1007/978-3-642-50854-7
- STROUHAL V (1878). *Über eine besondere Art der Tonerregung*. Annalen der Physik und Chemie 5:216–251, DOI: 10.1002/andp.18782411005

REFERENCES

- SUMMERFIELD M, FOSTER C & SWAN W (1954). *Flow Separation in Overexpanded Supersonic Exhaust Nozzles*. *Jet Propulsion* 24:319–321
- SUNLEY HLG & FERRIMAN VN (1964). *Jet Separation in Conical Nozzles*. *Aeronaut J* 68:808–817, DOI: 10.1017/S0368393100081086
- TAFOIRY G (2004). *Essais en soufflerie au culot - Exploitation des mesures instationnaires*. Campagne Vulcain 2 - NLR Septembre 2001 Ariane 5 Plus, A5-RE-1-X-359-ASAI, NLR, TE322 no. 142324 du 13/09/2004
- TROUTT TR, SCHEELKE B & NORMAN TR (1984). *Organized structures in a reattaching separated flow field*. *J Fluid Mech* 143:413–427, DOI: 10.1017/S0022112084001415
- VERMA SB, STARK RH, NÜRNBERGER-GÉNIN C & HAIDN O (2010). *Cold-gas experiments to study the flow separation characteristics of a dual-bell nozzle during its transition modes*. *Shock Waves* 20:191–203, DOI: 10.1007/s00193-010-0259-x
- VERMA SB, STARK RH & HAIDN O (2014). *Effect of Ambient Pressure Fluctuations on Dual-Bell Transition Behavior*. *J Propul Power* 30:1192–1198, DOI: 10.2514/1.B35067
- WAITZ IA, QIU YJ, MANNING TA, FUNG AKS, ELLIOT JK, KERWIN JM, KRASNODEBSKI JK, O’SULLIVAN MN, TEW DE, GREITZER EM, MARBLE FE, TAN CS & TILLMAN TG (1997). *Enhanced mixing with streamwise vorticity*. *Prog Aerosp Sci* 33:323–351, DOI: 10.1016/S0376-0421(96)00008-5
- WIKIPEDIA CONTRIBUTORS (2018). *Ariane 5* — *Wikipedia, The Free Encyclopedia*. Online; accessed 27-August-2018
- WINTERFELDT L, LAUMERT B, TANO R, JAMES P, GENEAU F, BLASI R & HAGEMANN G (2005). *Redesign of the Vulcain 2 Nozzle Extension*. In: 41st AIAA/ASME/SAE/ASEE Joint Propulsion Conference & Exhibit, AIAA, Tucson, Arizona, USA, pp 1–8